Electrodeposited CuO Thin-Film for Enhanced Photo-Electrochemical Glucose Oxidation

By

Neville James Cory

Thesis submitted in fulfillment of the requirements for the degree

Master of Engineering in Chemical Engineering

In the Faculty of Engineering and the Built Environment

At the

Cape Peninsula University of Technology

Bellville Campus

November 2021

Supervisor: Dr. Mahabubur Rahman Chowdhury

Declaration

I, Neville James Cory, declare that the contents of this thesis represent my own unaided work, and that the thesis has not previously been submitted for academic examination towards any qualification. Furthermore, it represents my own opinions and not necessarily those of the Cape Peninsula University of Technology.

Signed  **Date** 03/07/2021

Abstract

Cuprous oxide has been used as a non-enzymatic glucose sensor for decades. As such, there are a multitude of reports which focus on its electro-catalytic properties towards glucose oxidation though few make use of its intrinsic photocatalytic attribute. In this work, a visible light activated CuO porous film was developed using a three-step synthesis process. Optimization of each synthesis stage was achieved by comparing the sensors anodic peak currents in the dark to those captured under illumination from an LED light source. The physical characterization performed on selected samples included XRD, XPS, SEM, Hall Effect, Raman and UV-Vis to elucidate the morphology, bonding, optical and charge transfer properties. The electro-catalytic and photocatalytic oxidation of glucose was investigated by means of Cyclic Voltammetry, Electrochemical Impedance Spectroscopy and Chronoamperometric measurements under both the light and dark scenarios.

Optimization of the synthesis parameters showed the greatest difference between light and dark current density using a combination of 4 V for 2 min electrodeposition accompanied by 450 ℃ calcination for 1 h and an etching time of 2 min in concentrated NH_3 solution. XPS indicated two Cu 2p core levels peaks at 933.4 eV and 953.2 eV which confirms the presence of the Cu^{2+} species and hence, CuO. SEM images revealed trapezoidal crystal shapes on the FTO surface with increased porosity following etching. The optimized sensor presented a monoclinic structure following calcination and etching which suggests only the exposed facets were affected by NH_3. Analysis of the UV-Vis data found that the band gap (E_g) decreased from 2.07 eV to 1.88 eV following etching. Hall measurements indicate high charge carrier densities following n-type semiconductor behavior.

The CV results demonstrated that with the addition of light, the current density in 1 mM glucose solution increases by as much as 0.382 mA/cm^2 with all else equal. The electrochemical oxidation of glucose was found to be an irreversible electron transfer process controlled by diffusion in both the light and dark with regression coefficients R^2 of 0.993 and 0.999 respectively. EIS confirmed that the charge transfer resistance in the light decreases by several order of magnitude. Periodic illumination revealed persistent photoconductivity that's presence is as a result of deep-trap levels between the valence and conduction bands. Good amperometric performance was obtained for the CuO film with a 4 second response time with negligible interference from other species present in human blood. The sensor produced three linear ranges spanning over a 0.0-2.77 mM, 2.77-9.95 mM and 9.95-29.12 mM respectively. The linear range was unaffected by the incorporation of light however the sensitivity increased by 33.5% at a lower LOD.

Acknowledgments

Firstly, I would like to express my sincerest gratitude to **Dr. Mahabubur Chowdhury** for his excellent supervision throughout the period of this work. His devotion to the field of research coupled by his kind and go getter approach to life has inspired me in more ways than I could express. If it was not for your encouragement and recommendations, this work would most certainly not be completed in time. One day in my future regardless of where I am, I hope to be as inspirational, devoted and wise as you are.

Massive thanks to **Dr. Francious Cummings** from the University of the Western Cape (UWC) for running SEM and Hall Effect measurements. A special thank you to **Dr. Jessica Chamier** from the University of Cape Town (UCT) for conducting the Raman spectroscopy and your valuable input regarding possible further tests. Also, thanks to **Dr. Juliet Sackey** at the Council for Scientific and Industrial Research (CSIR) for providing the necessary UV-Vis data.

Last but certainly not least, I would like to thank the **National Research Foundation (NRF)** for their financial assistance over the past two years without which this work would not be possible. It must be noted that the opinions expressed herein along with the conclusions are those of the author and not attributed to the NRF.

Dedication

I would like to dedicate this thesis to my loving parents **Neville** and **Leonie Cory** who supported me with throughout my tertiary education. Your unconditional love, support and motivation through all the ups and downs have granted me this amazing opportunity that I will always be grateful for.

Also, to my sister **Ingrid Cory**, who was always there to bounce ideas off and never in short supply of great jokes to lighten the mood.

To my partner **Lauren Ann Woodworth** for all the time sacrifices she made to ensure that I keep on top of my work. No matter what, you were always there to lend an ear keep me motivated.

Finally, to my **friends** and **family** for their understanding and patience.

Table of Contents

Abstract ..... **i**

Acknowledgments ..... **ii**

Dedication ..... **iii**

List of Figures ..... **vii**

List of Tables ..... **ix**

List of Abbreviations: ..... **x**

List of Symbols: ..... **xi**

CHAPTER 1 ..... **1**

INTRODUCTION **1**

1.1. Introduction *1*

1.2. Background *1*

1.3. Problem Statement *3*

1.4. Aim & Objectives *3*

1.5. Scope & Delineations *4*

1.6. Organization *4*

CHAPTER 2 ..... **5**

LITERATURE REVIEW **5**

2. Introduction *5*

2.1. Photocatalysts *5*

2.2. Electronic Band Structure *9*

2.3. Current Developments *10*

2.3.1. Synthesis Methods *11*

2.3.2. Electrodeposition *12*

2.3.3. Cuprous Oxide Structure *13*

2.3.4. Photo/electro-catalytic Glucose Detection *14*

2.4. Aqueous Chemistry of Cyanide *16*

2.5. Electrochemical Analysis *19*

2.5.1. Cyclic Voltammetry *19*

2.5.2. Chemical Reversibility *20*

2.5.3. Diffusion *22*

2.5.4. Electrochemical Performance Validation *28*

CHAPTER 3 ..... **35**

EXPERIMENTAL PROCEDURES AND ANALYSIS TECHNIQUES **35**

3. Introduction *35*

3.1. CuO Thin-Film Synthesis *35*

3.1.1. Materials *35*

3.1.2. Synthesis procedure *35*

3.2. Electroanalytical Experiment Apparatus *36*

3.3. Physical Characterization *37*

3.3.1. Hall Effect *37*

3.3.2. SEM *39*

3.3.3. Raman *40*

3.3.4. X-ray Diffraction *41*

3.3.5. X-ray Photoelectron Spectroscopy *41*

3.3.6. UV-Vis *42*

CHAPTER 4 ..... **44**

RESULTS AND DISCUSSION **44**

4. Introduction *44*

4.1. Synthesis Optimization: *44*

4.1.1. Electrodeposition Time/Voltage Study *44*

4.1.2. Calcination Time/Temperature Study *46*

4.1.3. Etching Time Study *48*

4.2. Physical Characterization *50*

4.2.1. X-ray Diffraction *50*

4.2.2. X-ray Photoelectron Spectroscopy *51*

4.2.3. Scanning Electron Microscopy *53*

4.2.4. Raman *54*

4.2.5. Hall Effect *55*

4.2.6. UV-Vis Spectra *58*

4.3. Photo-Electrochemical Characterization *60*

4.3.1. Cyclic Voltammetry *60*

4.3.2. Concentration Dependence on CV response *69*

4.3.3. A proof of concept *70*

4.3.4. Reproducibility, Shelf-Life and Repeatability *71*

4.4. Charge Carrier Transport *72*

4.5. Chronoamperometric Measurements *79*

4.5.1. Different voltages etched *80*

4.5.2. Interference Study *84*

4.6. Persistent Photoconductivity *85*

CHAPTER 5 ..... **89**

CONCLUSIONS & RECOMMENDATIONS **89**

5.1 Conclusion *89*

5.2 Recommendations: *90*

References **91**

Appendix **101**

List of Figures

Figure 2.1: Band edge positions for common semiconductors relative to NHE at pH = 0 6
Figure 2.2: Electron and hole transfer via light irradiation 7
Figure 2.3: Diagram showing three types of recombination 8
Figure 2.4: Possible dye degradation pathways using a photocatalyst 8
Figure 2.5: Electronic band diagram indicating the fermi level position with respect to the conduction and valence band as well as the charge carrier concentrations 10
Figure 2.6: Distinction between TD and BU methods 11
Figure 2.7: Synthesis methods utilizing the BU approach 12
Figure 2.8: Schematic showcasing a typical electrodeposition system 13
Figure 2.9: Monoclinic CuO unit cell configuration 14
Figure 2.10: A) Triangular waveform, B) Standard CV for reversible system 20
Figure 2.11: Concentration profiles of a chemically reversible electron transfer process 21
Figure 2.12: Variation in scan rate for a) Reversible and b) irreversible reactions 22
Figure 2.13: Electrical double layer representation 23
Figure 2.14: CV of a chemically reversible electron transfer process 25
Figure 2.15: CV response to an irreversible electron transfer process 27
Figure 2.16: Potential step applied over time 29
Figure 2.17: Typical staircase chronoamperometric measurement for successive analyte additions 30
Figure 2.18: Phasor diagram illustrating the relationship between current and voltage in an AC system 31
Figure 2.19: Simple charge transfer reaction a) Nyquist plot and b) Bode plot 32
Figure 2.20: Circuits depicting a) series configuration and b) parallel configuration 33
Figure 3.1: Overall synthesis procedure prior to testing 36
Figure 3.2: Overall electrochemical analysis system 37
Figure 3.3: Depiction of the Lorentz force induced when charge flows 37
Figure 3.4: Illustration of the Van der Pauw configuration 38
Figure 3.5: Four-point connector hall voltage experimental set-up 39
Figure 3.6: Raman scattering energy diagram and Raman spectra 41
Figure 3.7: Double beam diffraction from two atoms in crystal plane 41
Figure 3.8: Depiction of XPS measurement process 42
Figure 4.1: Difference between light and dark anodic currents in 1 mM glucose for various electrodeposition voltages and times at A) 25 mV/s, B) 50 mV/s, C), 100 mV/s and D) 200 mV/s 45
Figure 4.2: Calcination temperature/time optimization using the difference in anodic peak current between dark and light in 1 mM Glucose at A) 25 mV/s, B) 50 mV/s, C) 100 mV/s and D) 200 mV/s 47
Figure 4.3: Pourbaix diagram for a Cu-H_2O system 48
Figure 4.4: Pourbaix diagram for a Cu-NH3-H_2O system at NH3 = [10 M] 49
Figure 4.5: Optimization of the NH_3 etching stage 50
Figure 4.6: XRD patterns for calcined and Etched CuO photoelectrode 51
Figure 4.7: XPS spectrographs for the “etched” sample focused on A) Cu 2p-peaks, B) O 1s-peaks, C) C 1s-peaks and D) Sn 3d-peaks 52

Figure 4.8: Spectrograph showing the full XPS range for the “etched” sample. 53
Figure 4.9: Cross sectional and surface SEM images respectively for As-deposited (A1-2), Calcined (B1-2) and Etched (C1-2) 54
Figure 4.10: Raman spectra for the various stages of synthesis including tested samples. 55
Figure 4.11: UV-Vis diffuse reflectance spectra for As-deposited, Calcined and etched samples with A) Reflectance R(%) and B) Absorption/Scattering (K/S) coefficients as determined through reflectance spectra 59
Figure 4.12: Band gap determination of A) “As-deposited” at n=2 and B) “Calcined and Etched” at n=2/3 59
Figure 4.13: Peak current densities recorded for the As-Deposited, Calcined and Etched samples at 100mV/s in 1mM Glucose. 61
Figure 4.14: Electrochemical behavior at 100 mVs^{-1} scan rate for the fabricated CuO electrode in a blank NaOH and 1 mM glucose solution under A) Dark and B) Light conditions 62
Figure 4.15: Glucose oxidation pathways 63
Figure 4.16: Glucose oxidation via hydroxyl radical attack ultimately forming of gluconic acid. 64
Figure 4.17: Energy diagram illustrating the coupling between CuO and the FTO substrate 65
Figure 4.18: CV cycles in 1 mM Glucose in the dark over a range of scan rates with peak anodic currents against scan rate and square root of scan rate and their linearities 66
Figure 4.19: CV cycles in 1 mM Glucose in the light over a range of scan rates with peak anodic currents against scan rate and square root of scan rate and their linearities 66
Figure 4.20: Peak potential vs. log(υ) in the A) Dark and B) light 67
Figure 4.21: Exponential decrease of the diffusion coefficient with increasing scan rate 69
Figure 4.22: Cyclic Voltammograms at various glucose concentrations (0.05, 0.1, 0.5, 1.0, 2.5 and 5 mM) respectively, at 100 mV/s scan rate under the A) Dark and B) light condition 70
Figure 4.23: Cyclic voltammograms for the “etched” CuO photoelectrode in the dark and under illumination from an iPhone and AutoLab cool white LED in 5mM Glucose and 100 mV/s Scan Rate 70
Figure 4.24: Electrode reproducibility test for five samples in light and dark conditions 71
Figure 4.25: Etched CuO photoelectrode Shelf-life assessment 71
Figure 4.26: Peak anodic currents for a series of 10 CV cycles on the same etched CuO sample illustrating repeatability 72
Figure 4.27: Nyquist plots in the dark (A1 and A2) and under illumination (B1 and B2) over a range of glucose concentrations 73
Figure 4.28: Top scan SEM images for samples following EIS testing A) As Deposited 50-cycles and B) Etched 50-Cycles 74
Figure 4.29: Modified Randel’s circuit in a double parallel configuration for two-time constants used in this work as the equivalent circuit 74
Figure 4.30: Zoomed in view of fitted high frequency Nyquist and Bode plots using the modified Randel’s circuit in A) Dark and B) Light for 1 mM glucose 78
Figure 4.31: Current response of selected samples during each stage of synthesis (As-deposited, Post Calcination and Post Etching) 80
Figure 4.32: Chronoamperometric measurements completed under dark and light conditions with 0.55 V, 0.57 V and 0.60 V bias 81

Figure 4.33: Zoomed view of chronoamperometric detection data at 0.6 V vs Ag/AgCl showing the first 300 seconds in the light and dark 81
Figure 4.34: Calibration curve for the “Etched” CuO thin film depicting 3 linear ranges in the A) Dark and B) light 82
Figure 4.35: Chronoamperometric response to common interfering species on the “etched” CuO electrode in the dark and light 85
Figure 4.36: Light Chopping experimental set-up 85
Figure 4.37: Light chopping at a 0.54 V bias for A) Low concentrations (NaOH, 0.1, 0.25, 0.5, 1.0 mM Glucose) and B) High Concentrations (2.5, 5.0, 10.0, 15.0, 20.0 mM Glucose) 88

List of Tables

Table 2.1: Performance criteria of typical sensors 6
Table 2.2: Advantages and disadvantages of TD and BU techniques (Zhang et al., 2006) 12
Table 2.3: Typical cyanide plating baths 16
Table 2.4: Works from Matsuda and Ayabe along with Nicholson and Shain correlating ΔEp with a dimensionless Λ parameter 26
Table 2.5: Cyclic voltammetric requirements for characterization of electrochemical systems 28
Table 2.6: Circuitry elements present in common equivalent circuits 33
Table 4.1: Peak investigation of XPS data for the “etched” sample 53
Table 4.2: Characteristic values determined through hall effect measurements 56
Table 4.3: Important electrochemical parameters deduced at various scan rates in the dark 68
Table 4.4: Important electrochemical parameters deduced at various scan rates in the Light 68
Table 4.5: Parameters used to fit dark EIS data through Microsoft excel using two-time constants 76
Table 4.6: Parameters used to fit light EIS data through Microsoft excel using two-time constants 77
Table 4.7: Successive glucose injections with respect to time and the decrease in NaOH concentration as a result of glucose additions 79
Table 4.8: Comparison drawn between this work and other similar CuO glucose sensors 83
Table 4.9: Indication time and concentration of the species injected into the testing chamber 84
Table 4.10: Fitting parameters for light chopping rise region 87
Table 4.11: Fitting parameters for light chopping decay region 87

List of Abbreviations:

ADA	American Diabetes Association
BU	Bottom-Up
CB	Conduction Band
CE	Counter Electrode
CPE	Constant Phase Element
CV	Cyclic Voltammetry
DBG	Direct Band Gap
EIS	Electronic Impedance Spectroscopy
FTO	Fluorine-Doped Tin Oxide
GOx	Glucose Oxidase
IBG	Indirect Band Gap
LOD	Limit of Detection
MO	Metal Oxide
PEC	Photoelectric Cell
PPC	Persistent Photoconductivity
RE	Reference Electrode
SEM	Scanning Electron Microscopy
TD	Top-Down
UV-Vis	Ultraviolet and Visible Spectroscopy
VB	Valence Band
WE	Working Electrode
XPS	X-ray Photoelectron Spectroscopy
XRD	X-ray Diffraction

List of Symbols:

Symbol	Description	Units
e^-/h^+	Electron Hole Pair	eV
C_o	Concentration	mol.cm^{-3}
D_o	Diffusion Coefficient	cm^2.s^{-1}
e^-	Electron	eV
E_g	Electronic Band Gap	eV
E^o	Standard Potential	Volts
E_p	Peak Potential	Volts
$E_{p/2}$	Half-Peak Potential	Volts
h^+	Photocatalytic Hole	eV
i_p	Peak Current	mA
k^o	Standard Rate Constant	Cm.s^{-1}
OH^-	Hydroxyl Ion	NA
R_{CT}	Charge Transfer Resistance	ohms
$\cdot OH$	Hydroxyl Radical	NA
A	Area	cm^2
aq	Aqueous	NA
E	Cell Potential	Volts
F	Faradays Number	C mol^{-1}
hv	Light	NA
j	Current Density	mA.cm^{-2}
n	Number of Electrons	Dimensionless
R	Universal Gas Constant	Jmol^{-1}K^{-1}
T	Temperature	Kelvin
α	Electron Transfer Coefficient	Dimensionless
τ	RC Decay Constant	Dimensionless
υ	Scan Rate	V.s^{-1}

CHAPTER 1

INTRODUCTION

1.1. Introduction

This research investigates the photo-electrochemical properties of thin film copper oxide for the purpose of glucose detection. Section 1.2 provides a background investigation to the problem with current glucose sensors. Section 1.3 defines the problem statement in context. Section 1.4 outlines the aims and objectives for this work while Section 1.5 describes the scope. The structure of the work is presented in Section 1.6.

1.2. Background

Diabetes has been affecting the human population for over three millennia. The earliest cases of the disease were mentioned by Egyptian physicians in 1552 BC (Karamanou, 2016). This disease is characterized by irregular glucose levels in the blood. The human body detects this irregularity and subsequently releases a hormone known as insulin from the pancreas. The inadequate or inability to make effective use of the insulin produced to regulate glucose levels is known as diabetes (Hwang *et al.*, 2018). Insulin removes glucose from the bloodstream by stimulating liver cells subsequently resulting in the liver converting the glucose to glycogen, thus regulating sugar levels present in the body. Along with the fact that this disease is life threatening, the American Diabetes Association (ADA) reported that co-morbidities such as obesity, hypertension, fatty liver disease, cancer and often related to bone fracturing (Association, 2019). Two common forms of the disease exist, type 1 which is hereditary and type 2 which is as a result the body's ineffective use of insulin.

Several studies have revealed that glucose level monitoring and controlling, both increased the life expectancy of patients living with the disease as well as reduced the co-morbidities associated with it (Barrett et al., 2016; Hwang *et al.*, 2018). It is with this that glucose detecting devices have become popular in this disease's management. Traditionally, self-detection and monitoring devices employ enzymes to provide glucose level data in point form (Oliver *et al.*, 2009). More recently however, non-enzymatic glucose detection methods are being investigated, with one company, Gluco Chaser, producing prototype sensors with its proprietary technology. Other novel technologies are also being pursued such as continuous monitoring devices which analyze real time data from patients through means of a sensor implanted subcutaneously (Hwang *et al.*, 2018). Enzymatic sensors have evolved from being mere photometric sensors to the market dominating enzymatic electrochemical sensors. The phasing out of first-generation photometric detectors is partly due to the operational limitations

of the technology, for instance, the exclusion requirement of bio-material in the test sample (Park, Boo and Chung, 2006). Furthermore, these detectors have a strong dependence on free oxygen to facilitate the catalytic activation/regeneration as well as a limited detection range. Second generation enzymatic sensors were introduced to overcome the oxygen dependence which resulted in the development of synthetic catalyst mediators. This resulted in much higher reaction rates but facilitated the accumulation of peroxide hindering detection (Toghill and Compton, 2010). The sensitivity of enzymatic glucose sensors is highly dependent on the immobilized enzyme's activity which complicates its ability to reproduce results. This generates uncertainty in the synthetic enzyme and raises concerns regarding legitimacy. Third generation sensors utilize electron transfer between the mesoporous electrodes and enzymes directly. Although in its infancy, stability of the sensors over a range of storage conditions remains problematic. Also, enzymatic sensors are single use thus require new test strips for every test.

Non-enzymatic sensors have promised to surpass previous generation developments in glucose detection and monitoring technology through simplicity. In contrast to tending to the highly complex requirements of enzymes, this technology hopes to oxidize glucose directly via non-enzymatic electrodes (Hwang *et al.*, 2018). This approach will allow a patient to test glucose levels using the same electrode which vastly reduces costs associated with glucose management. Although research has been carried out for decades regarding non-enzymatic oxidizing electrodes, the technology is still plagued with disadvantages thus limiting their practical application. The most critical aspect of a glucose sensor would be its monitoring ability over a range of concentrations in a given sample. These non-enzymatic sensors are limited by slow oxidation kinetics, electrode fouling and selectivity issues. In addition, the detection range is far smaller than enzymatic sensors and detectability is dependent on surface structure and the type of catalyst used (Toghill and Compton, 2010).

Transition and precious metals have showed great promise toward glucose detection however their high cost have hindered their application for a real world solution (Sehit and Altintas, 2020). A more cost effective solution steered research toward development of metal oxides (MO's) such as Co_3O_4, TiO_2, CuO, Cu_2O, ZnO and NiO. All of the aforementioned MO's share a common trait in that they are also semiconductors. Comparatively, tenorite (CuO) enjoys the most narrow band gap thus requires less photon energy incident on its surface to produce a photocurrent. The abundance of copper in the earth's crust coupled with the fact that the largest deposits of the element are found in Sothern Africa makes it an excellent candidate for this research (Institute, 2018). Furthermore, CuO is more thermodynamically stable than Cu_2O at ambient temperatures.

MO semiconductors such as CuO are mostly used in conjunction with a conductive support material which shuttle electrons to promote conductivity. Facilitation for the attachment to these substrates often requires costly or time consuming techniques such as vapor deposition, hydrothermal synthesis or spin coating. Alternatively, electrodeposition is a highly scalable technique that allows for rapid synthesis of nanomaterials while displaying high porosity and increased surface area (Thenmozhi *et al.*, 2017). In addition, this technique allows for a highly reproducible nanostructure further aiding in up-scaled production. A post electrodeposition treatment such as etching has in the past been found to enhance the electronic characteristics of copper oxides and even reshape their surfaces (Wang, Han and Tao, 2007; Zhu and Panzer, 2016). Development of a non-enzymatic sensor which is both cost and time effective is necessary to phase out the single use enzyme based sensors. Such a sensor is required to display enhanced performance toward glucose oxidation in terms of extended linear range, low LOD, high sensitivity, rapid response time and should remain unaffected by interfering species. Functionalizing the built-in semiconductor properties of CuO via the inclusion of light during glucose detection is scarcely reported on.

1.3. Problem Statement

Development of a non-enzymatic glucose sensor which does not suffer from a low linear range and sensitivity remains a challenge. Research pertaining to the synthesis of CuO nanofilms with enhanced photo-activity toward glucose detection are scarce despite a favorable band gap correlating to the visible spectrum.

1.4. Aim & Objectives

This research aims to form a stable, photo-electrochemical CuO thin-film via electrodeposition and to use its photocatalytic ability to enhanced glucose detection as a non-enzymatic sensor.

The research objectives are:

- To successfully optimize the synthesis stages (electrodeposition, calcination and etching) to maximize the difference in current density between the light and dark condition.
- Investigate the photoelectrochemical properties of the sensor to ascertain the key differences between glucose detection in the light and dark through cyclic voltammetry, electrochemical impedance spectroscopy and chronoamperometry.
- Elucidate parallels between the physical properties as determined via SEM, Hall Effect, UV-Vis and Raman spectroscopy to the photoelectrochemical performance toward glucose oxidation.

- Identify a possible mechanism which could be responsible for the detection enhancement.

1.5. Scope & Delineations

The scope of this work is limited to investigation of the photoelectrochemical and physical properties of CuO towards glucose detection. This excludes the temperature effects outside of room temperature during electrodeposition and testing. Only a standard strike solution is considered for electrodeposition experiments. Testing of human serum samples will also be omitted.

1.6. Organization

Chapter 1: Background
Provides the background to the research and contextualizes the need for improvement from current glucose management techniques.

Chapter 2: Literature Review
The relevant theory associated with semiconductor photocatalysis is discussed along with the currently accepted theories describing glucose oxidation. This also includes the electrochemical and photoelectrochemical theory and discusses in detail the relevant testing literature which aligns with the research objectives.

Chapter 3: Experimental Procedure and Physical Characterization
The experimental procedure provides an overview of the materials required and experimental steps taken to synthesize an n-type CuO semiconductor. This chapter also discusses the relevant physical characterization techniques employed to elucidate differences between samples.

Chapter 4: Results and Discussion
An attempt is made to draw meaningful conclusions for data acquired through experimental work is established. The data was interpreted and analyzed using relevant models and compared to other works to ensure validity.

Chapter 5: Conclusions and Recommendations
The most significant findings are reported along with further research focuses identified through this research. Further recommendations are made to solidify the findings presented with the significance thereof.

CHAPTER 2

LITERATURE REVIEW

2. Introduction

The following chapter provides a review into the literature and terminology regarding photocatalysts in Section 2.1, electronic band structure in Section 2.2, current developments regarding non-enzymatic glucose sensors in Section 2.3 which includes synthesis methods, CuO structure and photocatalytic glucose detection. Section 2.4 covers aqueous chemistry of cyanide while in Section 2.5, the various electrochemical analysis techniques are discussed. This chapter provides insight into how photocatalyst function, provides insight into testing techniques and relevant theory.

2.1. Photocatalysts

A process developed in the early 70's by Fujishima and Honda showed how water could be split into its constituent components over a TiO_2 catalyst under UV light bombardment, paved the way for modern day photocatalytic research (Fujishima and Honda, 1972). Since its discovery, research has been focused on enhancing the photocatalytic activity. Enhancement in this regard will benefit a multitude of research fields including waste water treatment, catalytic sensors, fuel cells and various environmental remediation practices.

Semiconductors that are activated upon the light irradiation from a part of or the full light spectrum are dubbed, photocatalysts. A photocatalytic reaction is highly dependent on the energy available which can be described by the wavelength of light and the specific catalyst being employed (Rajeshwar *et al.*, 2008). Although photoelectric cells (PEC) are the primary research field for harvesting light energy, very little is known about a photocatalytic approach toward enhanced glucose sensing. An ideal photocatalytic semiconductor exhibits the following traits: a narrow band gap to promote wide range light absorption, cheap to synthesize and availability of source materials, stability and non-toxic, enhanced charge carrier separation (Opoku *et al.*, 2017). In addition, the performance related criteria by which sensors are characterized are summarized in Table 2.1.

Table 2.1: Performance criteria of typical sensors

Trait	Description
Linear Range	- The range set forth in an analyte concentration to which the response is predictable i.e. Linear - Characterized by an R^2 value.
Sensitivity	- Depicted by the slope of the calibration curve. Steeper slope represents increased sensitivity. - Represents the response per unit of analyte.
Detection Limit	- The response for no concentration which is shifted by 3 standard deviations. - Allows for the distinction between background noise and response signal.
Response Time	- The amount of time taken from introduction of an analyte to reach 90% of the final response signal at steady state.
Stability	- Shelf life of the sensor as measured by the response decay over time.

A number of materials have been previously used as semiconductors such as those summarized in Figure 2.1. It can be seen that CuO has favorable band positions for catalytic water splitting as compared to other commonly used semiconductors. A materials band gap is a crucial property that is reflective of the materials ability to be activated via light.

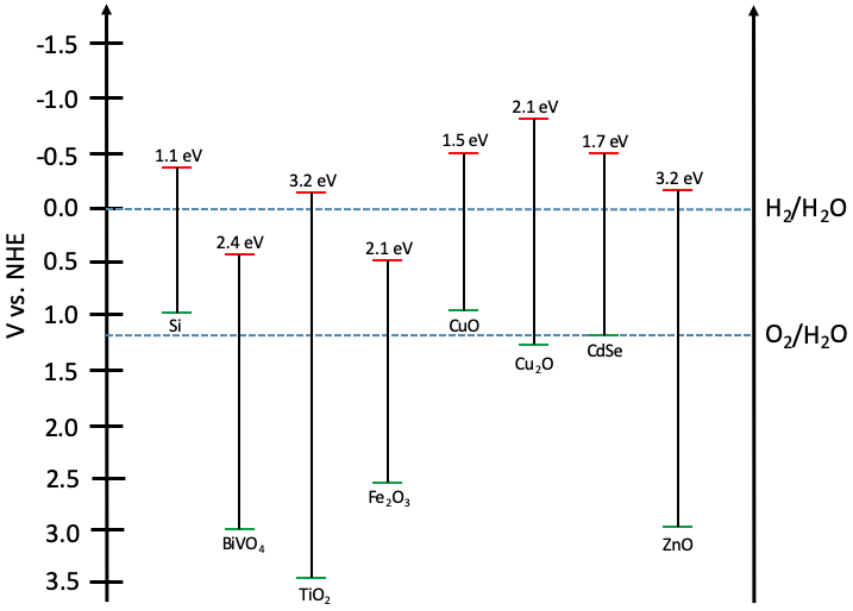

Figure 2.1: Band edge positions for common semiconductors relative to NHE at pH = 0

A material's band gap is given by the energy difference between valence and conduction band. When the VB peak occurs at the same electron momentum as that of the CB, a direct band energy gap (DBG) is present (University of Cambridge, 2020). Alternatively, when these bands do not peak at the same electron momentum, an indirect band gap (IBG) is formed. The fundamental difference between a DBG and IBG is that the amount of energy (E_g) that is required for an electron-hole pair to be produced upon light irradiation. An IBG semiconductor requires far more photon energy than its DBG counterpart. This principle also applies to the recombination of electron-hole pairs. Semiconductor based photocatalysts are unique in the

sense that they exhibit a vacant conduction band (CB) coupled with a full valence band (VB) (Han *et al.*, 2014). Charge carriers can be generated via illumination of a semiconductors surface. The photon energy brings electrons from a level of low energy to one of higher energy. When the energy is equal to or greater than the semiconductors band gap, electrons will move from the valence band into the conduction band leaving behind a hole as depicted in Figure 2.2. This is known as the generation of an electron-hole pair.

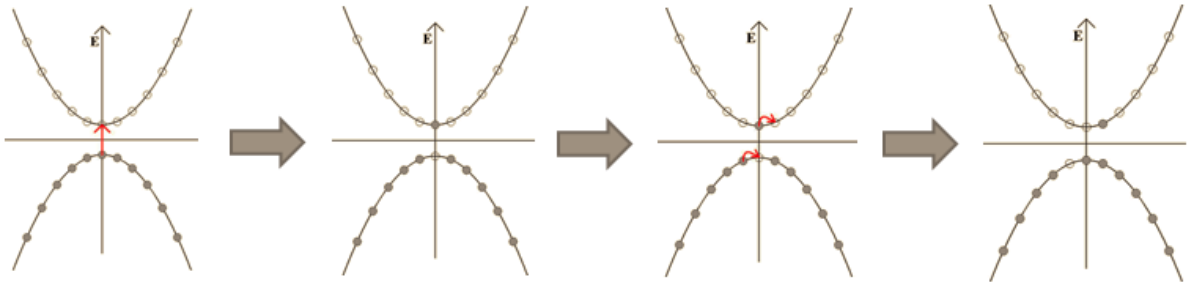

Figure 2.2: Electron and hole transfer via light irradiation

Electrons and holes are charged species and their transport is often complex. The movements of these charges are the cause of the photocurrent responses seen in semiconductors under light bombardment. Both charge carriers are readily affected by an electric field following an applied potential. This mechanism of charge transport is known as carrier drift. In addition, carriers migrate from regions of high charge density to those offering lower charge densities. This carrier concentration gradient gives rise to an alternative mechanism being carrier diffusion. The overall current in a semiconductor is a combination of both drift and diffusion current (Zeghbroeck, 2011b).

$$Photocatalyst + hv \rightarrow h^+ + e^-$$

The positively charged holes and negatively charged electrons may be trapped in site defects on the surface of the semiconductor causing undesirable recombination along with the release of energy as in the equation below (Opoku *et al.*, 2017):

$$h^+ + e^- \rightarrow energy$$

In a recombination process, oppositely charge electron-hole pairs cease to exist. These processes are classified based on the change in an electron's energy from its initial to final state. In a typical photoconductor, the recombination processes are mediated by inter band states. A lower recombination rate is expected with IBG semiconductors as electrons must first undergo momentum changes (University of Cambridge, 2020). Three types of recombination processes exist and are band to band, trap assisted and Auger which are illustrated in Figure 2.3.

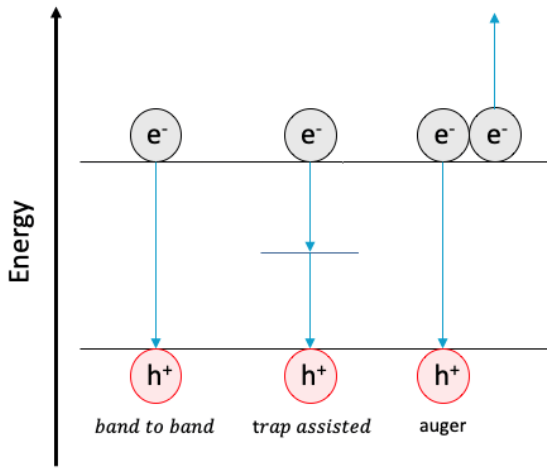

Figure 2.3: Diagram showing three types of recombination

Band to band recombination occurs when an electron from the conduction band directly combines with a positively charged hole in the valence band through the loss of energy and results in the release of a photon. The energy associated with this process is radiative. Trap assisted recombination occurs in two steps with the first being a reduction in the electron's energy to a trap state level within the band gap of a semiconductor. Thereafter, the electron moves back into the valence band fulfilling Shockley-Read-Hall recombination. Auger recombination occurs when a hole and an electron recombine in a band to band process, however the resultant energy is transferred to other carriers (Zeghbroeck, 2011c). Overall, recombination processes decrease the photocatalytic performance of a semiconductor. Electron scavengers or sacrificial reagents are used to mitigate the recombination of said electrons thus promoting the photocatalytic effect of the semiconductor (Opoku *et al.*, 2017). Successful charge carrier separation will result in electrons migrating to the surface which can be used to perform useful reactions such as those depicted in Figure 2.4. The electrons and holes migrate toward facets of high energy so as to decrease the surface energy contained within the crystal structure. The selectivity of the reactions that ensue are dependent on the flow of these charges toward the facets along with several other factors such as light intensity, pH, dye-water concentration as well as surface area (Pirsaheb *et al.*, 2020).

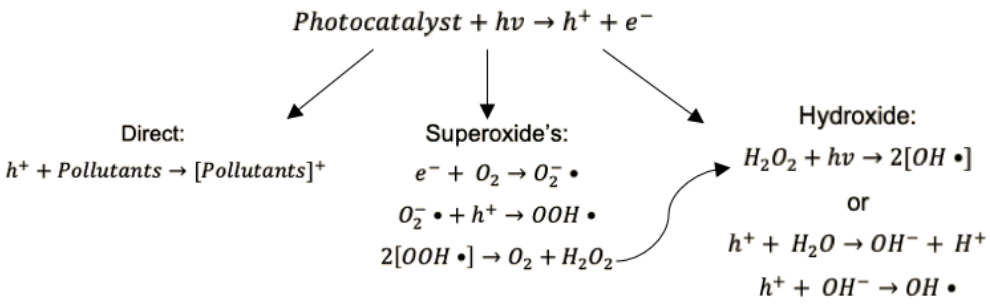

Figure 2.4: Possible dye degradation pathways using a photocatalyst

As per Figure 2.4, the holes generated via photon bombardment on a semiconductor, can oxidize pollutants directly in some cases if the conditions favor this. Alternatively, the photon-

induced charges can undergo redox reactions to form super-oxide or hydroxyl radicals via the branched mechanisms. Also, the excited electrons in the CB of the semiconductor facilitate a redox reaction by reacting with dissolved oxygen to generate superoxide anions (Ansari *et al.*, 2013). When the newly formed superoxide reacts with a proton, an unstable hydro-peroxyl radical is formed which is an intermediate that quickly decomposes to yield H_2O_2 followed by the regeneration of H_2O (Costa *et al.*, 2020). The rate of the reduction mechanism has however been reported to decrease with a decrease in the concentration of electron vacancies in the VB (Wen *et al.*, 2012). The successive excitement of the electrons into the CB coupled with the formation of the electron deficient VB provides the means to both oxidize and reduce species adsorbed onto the active sites of a photocatalyst (Rajeshwar *et al.*, 2008). Alternatively, hydroxyl radicals are produced via one of two mechanisms in Figure 3. The hydrogen peroxide formed by the superoxide radicals would decompose under photon bombardment and yields two hydroxyl radicals. The other mechanism involves much simpler kinetics whereby hydroxyl radicals are produced via oxidation of surface water or hydroxide ions in the VB of the semiconductor by the positively charged holes (Ansari *et al.*, 2013).

It is understood that the aforementioned reaction mechanisms all work in the same manner to degrade organic compounds. In the case of glucose sensors, the oxidation mechanism follows the hydroxyl assisted pathway with the inclusion of a metal oxide redox couple. Though in the light, the semiconductive behavior assists the oxidation process to essentially boost the electrochemical response. It is this additional current density that is of great interest as it is rarely reported on and could offer improved sensing performance by simply making use of its built-in physical property.

2.2. Electronic Band Structure

As previously established a semiconductors band gap is of great importance as this will determine the amount of energy that is required to excite an electron from the VB into the CB. In addition, it also determines which part of the electromagnetic spectrum will be absorbed by the material. Semiconductors with E_g > 9 eV are classed as insulators while no band gaps means they are conductors. Between 0 eV and 4.5 eV are most common band gaps for semiconductors in use today. Similarly, as important, the fermi energy level is an energy level which the likelihood of encountering an electron is 50 %. The fermi energy level for an intrinsic semiconductor lies between the CB and VB as presented in Figure 2.5. It is known that incorporation of dopants causes a shift in the fermi-level and results in band bending. A semiconductor can be classed as n or p-type based on the electron concentrations in the CB. When excess holes are present in the CB, the material is designated to be a p-type material whereas if the opposite were true the n-type designation would be made. Accordingly, the

fermi-level in an n-type material exists closer to the CB. This band structure determines the optical properties and directly results in direct or indirect band transitions.

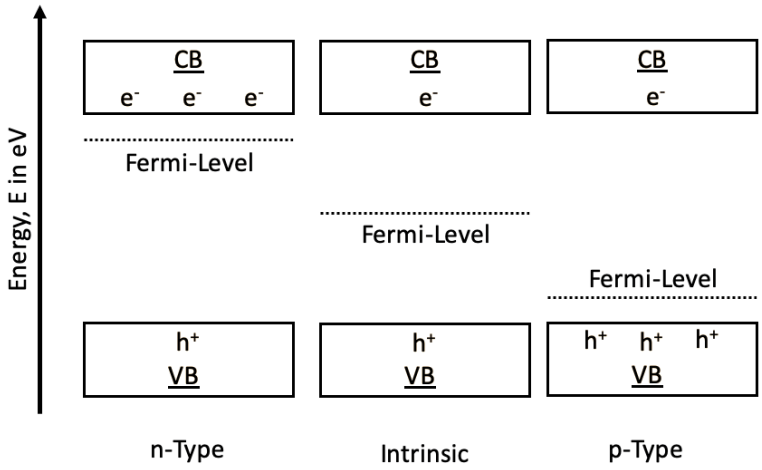

Figure 2.5: Electronic band diagram indicating the fermi level position with respect to the conduction and valence band as well as the charge carrier concentrations

2.3. Current Developments

Glucose Oxidase (GOx) sensors are enzymatic-based glucose sensors that are among the most widely used biosensors on the market. These sensors retain a high surface area which allows for enhanced electron transfer kinetics and high accuracy with good selectivity. Enzymes are however extremely susceptible to temperature swings and humidity levels making these electrocatalysts intrinsically unstable. In-vitro glucose monitoring via GOx suffer greatly from high manufacturing costs given their single use application. It is for these reasons that a great deal of research has focused on the development of a non-enzymatic alternative of which is low cost, stable and can be used multiple times to drive down the costs to consumers suffering from diabetes. Zhu et al., (2016) described non-enzymatic amperometric sensors to offer all the aforementioned characteristics with the inclusion of a low limit of detection as well as a rapid response time (Zhu *et al.*, 2016).

Since conception of the need for non-enzymatic sensors to overcome the shortcomings of the current GOx glucose sensors, a vast amount of materials have been synthesized such as metals, metal oxides, alloys, composites, metal-complexes and carbon based structures. The functionality and performance of each of these sensors are highly dependent on the transition metal center (Toghill and Compton, 2010). The electrocatalysis of glucose and other organic compounds are believed to occur over the surface of the electrodes in processes which involve d-shell electron transfer (Juska and Pemble, 2020). Metallic electrodes have extensively been studied though the most promising metals appear to be precious metals such as gold and platinum which on their own are extremely expensive as raw materials (Sehit and Altintas,

2020). Furthermore, materials such as Pt have been reported to degrade in environments which contain amino, uric and ascorbic acids, all of which coexist in physiological solutions. A more cost effective solution steered research toward development of metal oxides (MO's) such as Co_3O_4, TiO_2, CuO, Cu_2O, ZnO and NiO (Tian, Prestgard and Tiwari, 2014; Tian *et al.*, 2018). All of the aforementioned MO's share a common trait in that they are also semiconductors, though very few researchers make use of this inherent property especially toward glucose detection. This will be addressed in more detail in the following sections.

2.3.1. Synthesis Methods

Currently, a wide range of techniques are being employed to synthesize nanomaterials. These methods are characterized by two approaches (Figure 2.6) namely Bottom-up (BU) and Top-down (TD) (Ruffino and Grimaldi, 2019). With both methods yielding successful synthesis of nanoparticles, the desired approach is selected based order of merit.

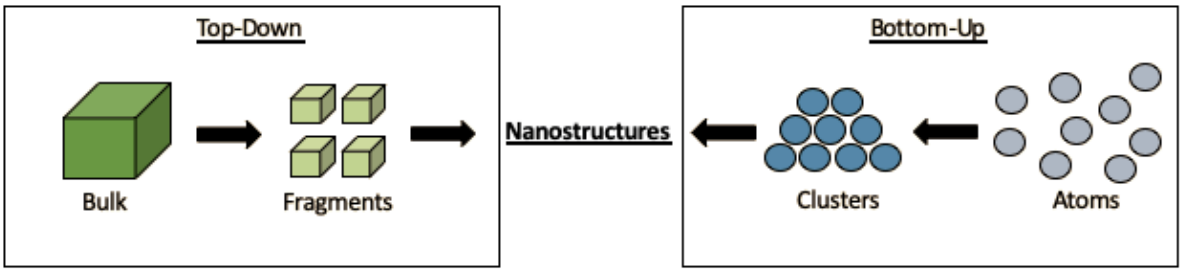

Figure 2.6: Distinction between TD and BU methods

The BU method involves material growth at an atomic scale based on the physical and chemical interaction between the atoms and fields. An external force can be applied during growth so as to direct or favor the attraction of atoms in the formation of desired morphologies or to expose desired facets (Khan, Saeed and Khan, 2019). Alternatively, the TD approach uses bulk materials often on the micro-scale and systematically reduces their size to fit the required scale. Both these approaches have their own advantages and disadvantages which are compared in Table 2.2.

The BU approach is often favored due to the distinct advantages it bares over is counterpart not to mention its limited disadvantages. The synthesis of functional nanomaterials using this approach has been conducted using various methods which are represented in Figure 2.7 (Dhand *et al.*, 2015).

Table 2.2: Advantages and disadvantages of TD and BU techniques (Khan, Saeed and Khan, 2019).

	Top-Down	Bottom-Up
Advantages	- Easily scalable - No purification required	- Various morphologies - Deposition parameters are controlled - Particle size distribution is narrow - More economical method
Disadvantages	- Large particle size distribution - No set morphology - Deposition parameters are uncontrolled - Impurities lead to defect sites - Uneconomic	- Difficult to scale production - High purity precursors are required

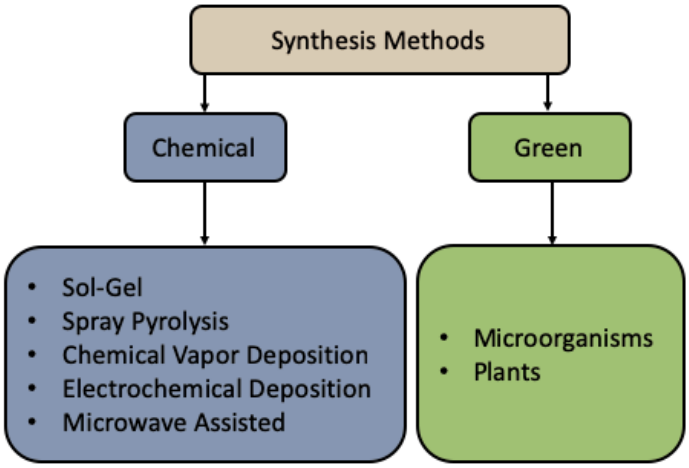

Figure 2.7: Synthesis methods utilizing the BU approach

2.3.2. Electrodeposition

The film synthesis method employed in this research focuses on electrochemical deposition which requires a conductive substrate (Florine doped tin oxide) onto which a metallic coating will form. This occurs when metal ions are electrochemically reduced from an electrolyte to form crystalline layers. For this process to occur, the electrolyte solution (liquid) must contain both positive and negative ions. Typically, the working electrode (cathode) and counter electrode (anode) are submersed in a vessel (cell) containing the electrolyte solution. The electrical circuit is completed by connecting the anode and cathode to their respective terminals on a battery or power source. With an adequate voltage, metal ions will reduce to metal atoms which nucleate onto the substrate surface. The anode is connected to the positive terminal whereas the cathode is connected to the negative terminal such that a metal layer via the following equation is deposited.

$$M^{n+}(aq) + ne^{-} \rightarrow M(s)$$

Where, M represents a metal and n denotes the number of electrons. Typically, the circuit is arranged as depicted in Figure 2.8. Here, electrons are driven by the power supply into the solution through the cathode. Current is carried across the electrolyte by the cations toward the cathode where a reduction reaction occurs. Nucleation occurs to form a thin layer on the substrates surface of which the thickness is highly dependent on the deposition time, temperature and analyte concentration.

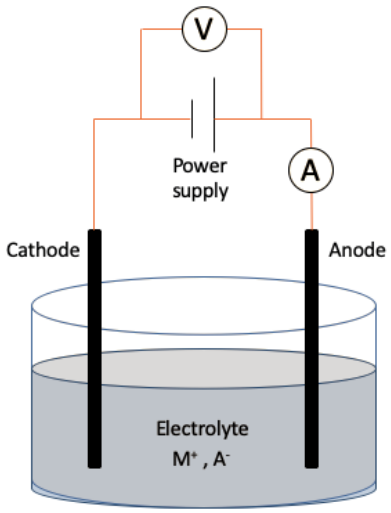

Figure 2.8: Schematic showcasing a typical electrodeposition system

Currently, a great deal of interest has been expressed for electrodeposition as a method to synthesize nanomaterials. The advantages of this method are extensive and include but are not limited to morphological control by using templates, precise nanomaterial size control over timescales as small as 1 nanosecond at predetermined voltages. In addition, considering that this process is very well established and is currently being used in many industrial applications such as copper plating, the transition from pilot to full scale fabrication is seamless.

2.3.3. Cuprous Oxide Structure

The most common stable forms of copper oxide come in the form of Cu_2O and CuO. The phase differentiation is crucial as their physical properties as well as catalytic properties differ drastically. Visually, CuO presents with a dull black surface whilst Cu_2O is dull brown with both lacking luster. Their band gaps differ vastly with CuO enjoying a much more favorable 1.2-1.9 eV in its monoclinic form as oppose to Cu_2O with a band gap between 2.0-2.2 eV. Other structural differences include a monoclinic crystal structure as oppose to a cubic structure which results in the preferential exposure of particular facets which may or may not benefit light absorption. The CuO unit cell consists of single Cu^{2+} atoms coordinated by four O^{2-} ions

in its crystal structure as presented in Figure 2.9. CuO also known as tenorite exhibits a monoclinic structure in a with C2/c space group symmetry.

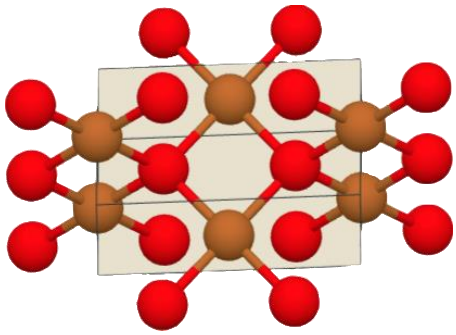

Figure 2.9: Monoclinic CuO unit cell configuration

(Materials Project, 2021)

2.3.4. Photo-electrocatalytic Glucose Detection

A number of synthesis techniques have been investigated over the last decade to produce a non-enzymatic glucose sensor that meets the requirements set out by the international organization of standardization (ISO) (Toghill and Compton, 2010). Though current non-enzymatic glucose sensors display enhanced sensing characteristics, the detection range is limited with only few just attaining double digit milli-molar (mM) detections. A typical glucose response displays a linear and non-linear range. In the former, the glucose concentration can be deduced directly via the current response whereas the concentration is unpredictable within the non-linear range. Beyond this point, a saturation level is reached and the current no longer increases with concentration. It is for this reason that the linear range is of great importance. Many researchers have attempted to uncover the root cause for low linear ranges plaguing non-enzymatic glucose sensor. At first, the surface volume was believed to be responsible for the low linear ranges. This was investigated using a Cu-Graphene heterojunction and found to be a contributing factor though only a minor increase in linear range was attained to an upper limit of 4.5 mM (Luo *et al.*, 2012). Later, an investigation by Annalakshmi et al proposed that the linear range was limited by applied potential to the working electrode (Annalakshmi *et al.*, 2019). It was determined however that even upon lowering the oxidation potential of glucose on their electrode, the linear range changed only by an unappreciable amount. In an effort to further enhance the linear range, Yang et al determined that the hydroxyl concentration was the limiting factor (Yang *et al.*, 2020). They were successful in increasing the linear range of a $Ni(OH)_2/Ni_{sheet}$ from 4 mM to 40 mM by increasing the NaOH concentration from 0.1 mM to 1000 mM respectively. They summarized that glucose could react with hydroxyl ions at high concentration which produce enediol intermediates that act to decrease the energy barrier for the electrooxidation reaction. It was also noted that an increased sensitivity was also resulted from the higher OH^- concentration.

In a study by Ashrafi et al. (2016), a rGO/CdS composite was hydrothermally prepared and decorated via electro-deposition with CoOx nanostructures (Ashrafi, Salimi and Arabzadeh, 2016). The overall nano-composite rGO/CdS/CoOx was utilized as a glucose sensor in the dark and under visible light irradiation. They found that in the presence of light, the limit of detection decreased from 0.87 to 0.40 μM while the sensitivity increased from 0.12 to 0.22 $\mu A/\mu M$. Upon amperometric determination, the linear range was revealed to be 0.001-0.6 mM at 0.4V vs Ag/AgCl though remained unchanged with the inclusion of light. Similarly, Wang, et al. developed a $BiVO_4$ photocatalytic glucose sensor via a simple electrochemical deposition (Wang *et al.*, 2019). They found that this sensor displayed an increased oxidation current (+1.45 mA/cm^2) while under illumination and a wide linear range (0.0 - 5.0 mM). In both cases, the enhanced performance was attributed to an increase in the steady state oxidation current stemming from the generation of electrons and holes with successful charge carrier separation. In another study, the influence of the applied potential on the glucose sensing performance was investigated by Feng et al (Feng *et al.*, 2014). It was found that with the inclusion of light, between 0.2-0.6 V vs Ag/AgCl, the sensitivity's obtained remained similar though above this potential, the sensitivity decreased drastically. Jafari, Salimi and Navaee explained that photoelectrochemical glucose sensors are more sensitive than electrochemical glucose sensors (Jafari, Salimi and Navaee, 2014). Liu et al, optimized the electrodeposition process of a thin $BiVO_4$ film specifically for enhanced sensitivity via an improved photocurrent (Liu, Yu and Zhang, 2017). They reported that the film thickness greatly influenced the sensitivity. Thick films hindered light absorption thus limited the transfer of charge carriers.

The thermal oxidation parameters of deposited CuO films were investigated by Panah et al. (Masudy-Panah *et al.*, 2016). It was found that rapidly annealing these films at a temperature of 550 ℃ produced highly crystalline films with increased grain sizes which significantly enhanced the photocurrent generation. The effects ammonia etching on electrodeposited Cu_2O films was investigated by Zhu and Panzer (Zhu and Panzer, 2016). They discovered that upon exposure to concentrated NH_3, the surface film became highly textured with regular morphology. The ammonia attacked (100) and (111) facets by controlling only the etching time. After only 1 min, the samples presented with decreased interface states thus lowering the amount of recombination centers and enhancing the photovoltaic performance.

2.4. Aqueous Chemistry of Cyanide

A very well-known plating solution consists of a cyanide bath which is often utilized because of certain advantages even though cyanides are extremely toxic. Cyanides behave as ligands during electroplating processes and the toxicity thereof is outweighed by the fact that the metal

oxidation states are lower in these baths compared to cuprous salts on an electrochemical equivalent standard (Chu and Fedkiw, 1993). Also, the deposition from cyanides is fine-grained and uniform which translates to excellent throwing power (Hong, Park and Lee, 2014). Furthermore, these baths allow for the formation of cyanide complexes which possess the ability to shift deposition potentials to more negative values and so prevent the displacement of copper in the presence of less noble metals. These characteristics in electrochemical deposition processes are extremely sought after and cyanide baths offer such benefits effectively justifying their use. The electrodeposition processes of copper from cyanide-based solutions are plentiful (Fujiwara and Enomoto, 2000; Cho *et al.*, 2007; Kim *et al.*, 2012, 2013). The process has been used in the metal finishing industry since 1840 because of its macro-throwing power which allows plating onto any shape (Passal, 2006).

The strike baths presented in Table 2.3 are extensively used to produce thin copper coatings that act as a seed layer or nucleation sites. The typical thickness of these layers range between 0.5 and 1μm depending on the striking time. Aqueous chemistry shows that $CuCN$ can be dissolved in solutions containing excess cyanide ($NaCN\ or\ KCN$) to form cyanocuprate ions such as $Cu(CN)_2^-$, $Cu(CN)_3^{2-}$ and $Cu(CN)_4^{3-}$ (Lu, Dreisinger and Cooper, 2002). Between sodium and potassium cyanide, $NaCN$ was chosen because of the high cost of KCN. The dissociation chemistry of copper cyanide is highly dependent on the concentration ratio between $[CN^-]$: $[Cu]$ as well as the temperature, solution pH and ionic strength (Kyle and Hefter, 2015).

Table 2.3: Typical cyanide plating baths

Bath Type	Strike	Rochelle Salt	High Efficiency
[CuCN], g/l	11	15-30	-
[NaCN], g/l	22	4-9	-
[Na_2CO_3], g/l	7.5	15-60	-
Voltage, V	6	6	0.75-4
Cathode Current, A/dm^2	1.0-3.2	1.6-6.5	1.0-11
Source	(Hong, Park and Lee, 2014)	(Lowenheim, 1974)	(Lowenheim, 1974)

The dissociation of CuCN in excess free CN^- will occur in such a way that the aforementioned cyanocuprate complexes appear in dynamic equilibrium.

$$CuCN(s) \leftrightarrow Cu^+ + CN^-$$

Detection of the di-cyanocuprate complex is extremely difficult as it exists in very low concentrations and rapidly breaks down under most experimental conditions.

$$CuCN + CN \leftrightarrow Cu(CN)_2^-$$
$$Cu^+ + 2CN^- \leftrightarrow Cu(CN)_2^-$$

Predominant formation of the tri-cyanocuprate ion is highly dependent on the presence of excess $3CN^-$ ion relative to a Cu^+ ion which typically yields solutions with a pH > 5.

$$Cu(CN)_2^- + CN^- \leftrightarrow Cu(CN)_3^{2-}$$

Tetra-cyanocuprate is commonly formed at a pH>10.

$$Cu(CN)_3^{2-} + CN^- \leftrightarrow Cu(CN)_4^{3-}$$

The $Cu(CN)_3^{2-}$ ion is predominantly formed according to Hong, Park and Lee in their investigation into the optimal plating conditions (Hong, Park and Lee, 2014). As such, this species is formed and dissociates to into Cu^+ as follows:

$$CuCN + NaCN \rightarrow NaCu(CN)_2$$
$$NaCu(CN)_2 + NaCN \rightarrow Na_2Cu(CN)_3$$
$$Na_2Cu(CN)_3 \rightarrow 2Na^+ + Cu(CN)_3^{2-}$$
$$Cu^+ + 3CN^- \leftrightarrow Cu(CN)_3^{2-}$$

According to Le Chatelier's principle, excess CN^- ions will shift the equilibrium position to the right which results in the suppression of Cu^+ ions forming. Also, when $NaCN$ is in great excess, the high coordination a number complex ion form whilst in deficit $Na_2Cu(CN)_3$ will break down. This is an effective way to limit the formation of Cu^+ ions thus allowing for even coatings.

$$Na_2Cu(CN)_3 + NaCN \rightarrow Na_3Cu(CN)_4$$
$$Na_2Cu(CN)_3 \rightarrow NaCu(CN)_2 + NaCN$$

This shows the importance of using the correct molar ratios to develop an adequate strike solution. Depending on the cyanocuprate species present, electrodeposition reaction mechanisms will vary depending on reaction conditions previously mentioned. Direct deposition from the scarce $Cu(CN)_2^-$ complex is as follows (Lowenheim, 1977):

$$Cu(CN)_2^-(aq) + e^- \rightarrow Cu(s) + 2CN^-$$

Similarly, the $Cu(CN)_4^{3-}$ species has been proposed to also undergo direct deposition by accepting an electron, however these reports are not common. Alternatively, a two-step deposition from this species is most often considered.

$$Cu(CN)_4^{3-}(aq) + e^- \rightarrow Cu(s) + 4CN^-$$

Or

$$Cu(CN)_4^{3-}(aq) + e^- \rightarrow Cu^+ + 4CN^-$$
$$Cu^+(aq) + e^- \rightarrow Cu(s)$$

The predominantly formed $Cu(CN)_3^{2-}$ complex undergoes a two-step electrodeposition process.

$$Cu(CN)_3^{2-}(aq) + e^- \rightarrow CuCN + 2CN^-$$
$$CuCN + e^- \rightarrow Cu(s) + CN^-$$

Hwang et al. investigated the oxidation of cyanide complexes under various concentrations and found that it was possible to deposit CuO from high alkalinity cyanide baths (Hwang, Wang and Wan, 1987). The mechanism proposed by them is as follows where n = 2, 3 or 4:

$$Cu(CN)_n^{(n-1)-} + 2(n)OH^- \rightarrow Cu^+ + (n)CNO^- + (n)H_2O + 2(n)e^-$$
$$2Cu^+ + 2OH^- \rightarrow Cu_2O + H_2O$$
$$Cu_2O + 2OH^- \rightarrow CuO + 2H_2O + 2e^-$$

CuO is known to be an effective catalyst toward anodic CN^- oxidation at low cell potentials ($E^0 = -0.97V\ vs\ SHE$) and in a sequence of reactions yields CO^{3-} and N_2 (Szpyrkowicz *et al.*, 1998).

$$CN^- + 2OH^- \rightarrow CNO^- + H_2O + 2e^-$$
$$2CNO^- + 8OH^- \rightarrow 2CO_3^{2-} + N_2 + 4H_2O + 6e^-$$

The photocatalytic oxidation of glucose via electrodeposited CuO from cyanide solutions has to the best of our knowledge gone unreported.

2.5. Electrochemical Analysis

The 18th century marked the birth of electrochemistry which since inception has undergone major advancements both in terms of understanding and technology. In the modern day, electrochemistry can be described as the study of chemical processes resulting from/in movement of electrons. A chemical species undergoing a charge transfer (ion or electron)

process is called an electrochemical redox-reaction if there is a change in the species' oxidation state. In nature, this can occur due to chemical energy or artificially by applying an external potential. A redox reaction encompasses two processes oxidation and reduction which require a loss/gain of electron(s).

Oxidation: $Reductant \rightarrow Prod + ne^-$

Reduction: $Oxidant + ne^- \rightarrow Prod$

For a reaction that occurs between species that exist in the same phase, it is said to be homogeneous (liquid-liquid) whereas a heterogeneous (liquid-solid) reaction occurs between species is alternate phases. The latter would occur at the interface separating the two phases. Electrochemistry as an analytical tool has become the norm to define and characterize systems involving electrochemical changes. Electroanalytical methods such as potentiometry, voltammetry, cyclic voltammetry (CV) and chronoamperometry relate analyte concentration(s) to measured potentials, currents, and resistances. This becomes particularly advantageous when investigating reaction kinetics and characteristics of said reactions. In this section, the electroanalytical methods are described along with the conclusions one can draw from them.

During voltammetric techniques, a potential is applied through an electrochemical cell to an electrode while simultaneously measuring resultant current response. Voltammetry is a broad term that encompasses sweeping (CV) and step (chronoamperometry) potential methods. The former provides insight into the relationship between faradaic and capacitive currents as measured in the cell whereas the latter deals with faradic currents (Harris *et al.*, 2019).

2.5.1. Cyclic Voltammetry

Cyclic voltammetry (CV) is an analytical potential sweep method that employs triangular waveforms (Figure 2.10A) to reveal important characteristics such as transfer kinetics/properties. In practice it is performed by linearly increasing an applied potential to a set value and then decreasing the potential back to its origin with respect to time. The rate at which the voltage is increased is referred to as the scan rate. A molecular species (in solution) will undergo a redox reaction at sufficient potentials which results in the generation of an electrical current. The observed current is a combination of faradaic and capacitive currents which occur during a potential sweep. Not all species react at the same potentials nor do they occur with similar intensities, thus this method can be used to identify multiple species and also provide an indication of their concentrations. In addition, this method offers quantitative data regarding heterogeneous redox thermodynamics, electron transfer and identification of

diffusional or kinetic processes (Bard and Faulkner, 2000). A cyclic voltammogram is constructed (Figure 2.10B) featuring the applied potential vs current response.

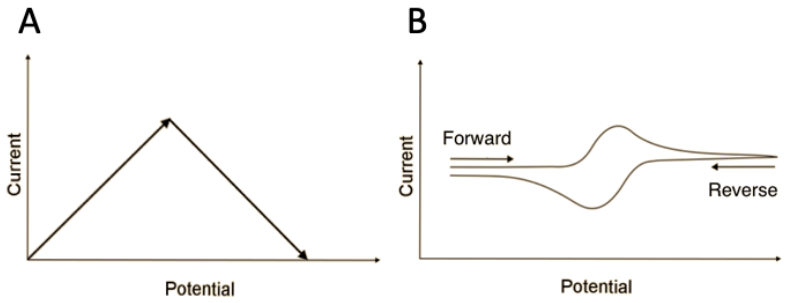

Figure 2.10: A) Triangular waveform, B) Standard CV for reversible system

In a typical heterogeneous redox-reaction, oxidation (forward scan) will begin at an onset potential which is characterized by the formation of a rising anodic current. As the potential rises through the forward sweep, so does current until a peak potential is reached. It is at this point where diffusion limits a further increase in current and in fact decreases with a classical tail shape forming the oxidation peak (Sandford *et al.*, 2019). The reversed scan becomes interesting as there are several possible scenarios. It is important to distinguish between chemical and electrochemical reversibility. If a net charge transfer exists at equilibrium in a system, it is said to be an electrochemical system whereas a chemical system will result in no resultant charge transfer (Chem LibreTexts, 2020). To distinguish between these electrochemical mechanisms, an “E” and “C” system is used where E is an electron transfer reaction and C is a chemical reaction.

2.5.2. Chemical Reversibility

The extent of chemical reversibility relies on the stability of the electrochemically generated species toward further reaction after electron transfer.

$$Oxidant + ne^{-} \rightleftharpoons Reductant \overset{k_c}{\rightarrow} Prod$$

Here, the chemical rate constant k_c dictates the extent of conversion between reductant and product. For small k_c values, the system is considered to be chemically reversible whereas at large k_c values, the formation of product is too fast resulting in chemical irreversibility. At more intermediate k_c values, the system has limited chemical reversibility. Thus, if one of the redox pair undergoes a reaction then it is said to be chemically irreversible. An electrochemical system is sensitive to change in species surface concentration and electrode potential. These changes easily are predicted by the Nernst equation.

$$E = E^{o} + \frac{RT}{\mathrm{nF}} \ln \frac{[oxidant]}{[reductant]}$$

Where the cell potential E, is related to the standard potential E^{o} and the ratio between the oxidized and reduced species for a system at equilibrium. Also, in the Nernst equation, R denotes the universal molar gas constant (8.314 $Jmol^{-1}K^{-1}$), T is the temperature (K), n depicts the number of moles of electrons and F is faradays constant (96500 C mol^{-1}). It is clear that potential shifts will impact the concentration of the redox species involved (Elgrishi *et al.*, 2018). The redox species surface concentration at time stamps labelled on the CV curve time stamps indicated on the CV curve in Figure 2.11 serve to illustrate how an applied voltage shifts equilibrium.

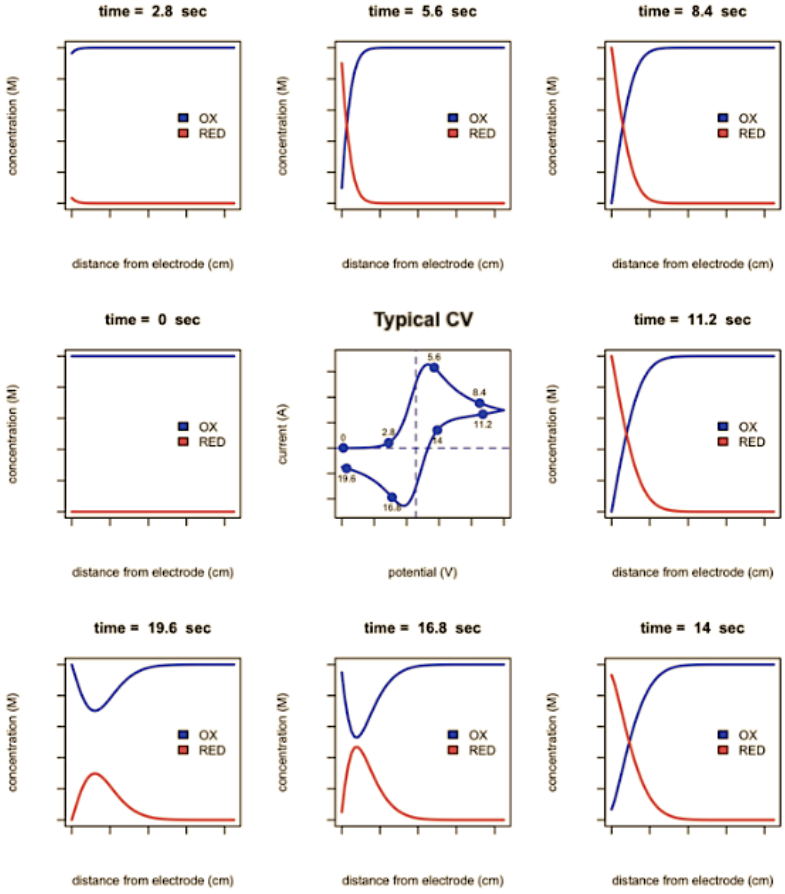

Figure 2.11: Concentration profiles of a chemically reversible electron transfer process (Depauw, 2020)

The CV illustrated in Figure 2.12 was conducted using a single scan rate. The voltage ramp or scan rate υ (V/s) is another important factor in characterizing a system. By varying the scan rate in a electrochemical process a relationship between the peak current and voltage ramp is established. This relationship can indicate whether a reaction is reversible or irreversible as presented in Figure 2.12:

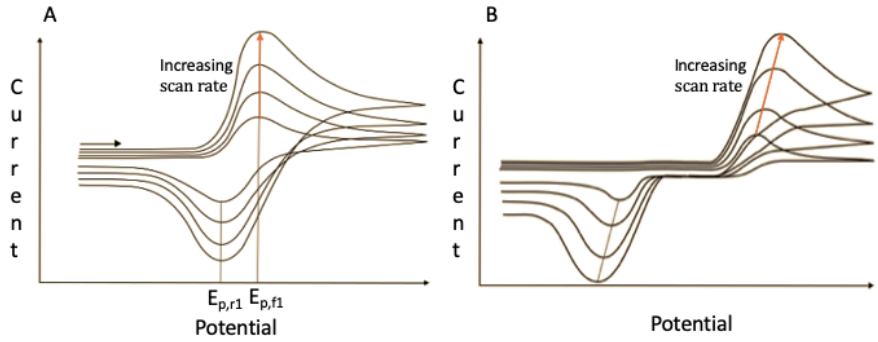

Figure 2.12: Variation in scan rate for a) Reversible and b) irreversible reactions (Graham, 2018)

A chemically reversible system where the reacting species are at with the bulk solution is presented below:

$$Oxidant + ne^- \overset{k_f, k_r}{\Longleftrightarrow} Reductant$$

In this unique case, the forward (k_f) and reverse (k_r) rate constants are at equilibrium resulting in the standard rate constant (k^o) which is simply a measure of the redox kinetics. This occurs when the applied potential (E) is equal to the standard potential E^o. When a large k^o is observed, the system will tend to equilibrium rapidly whilst a small k^o indicates slower kinetics (Bard and Faulkner, 2000). At a potential other than the standard potential, the forward and reverse rate constants are related to the standard rate constant according to the expressions:

$$k_f = k^o e^{\frac{-\alpha nF(E-E^o)}{RT}} \quad and \quad k_r = k^o e^{\frac{(1-\alpha)nF(E-E^o)}{RT}}$$

Where, α is the transfer coefficient which describes the symmetry between the forward and reverse reaction. Typically, the value of α is found to be between 0.3 and 0.7 (Bard and Faulkner, 2000).

2.5.3. Diffusion

As previously mentioned, the rise in faradaic current on the forward scan of a CV eventually gives way to a capacitive current alluding to a mass transport phenomenon. The rate of an electrochemical reaction can be limited by diffusion through the flux $J(x,t)$ of species to the electrode surface. This is expressed as follows:

$$J(x,t) = -\frac{i}{nAF}$$

In the equation, the current is i (A), the number of electrons n, the electrode area is A (cm^2) and F represents faradays constant is F (96500 C mol^{-1}). For heterogeneous electrochemical processes, diffusion occurs when there is a concentration gradient between the surface of an electrode and the bulk solution. An electrical double layer is formed between the electrodes surface and the bulk solution (Dunwell, Yan and Xu, 2018). The double layer consists is split into an inner/outer Helmholtz layer and a diffusion layer as depicted in Figure 2.13. The latter can be described as a region containing cations and anions whose net charge is zero (Double *et al.*, 1990).

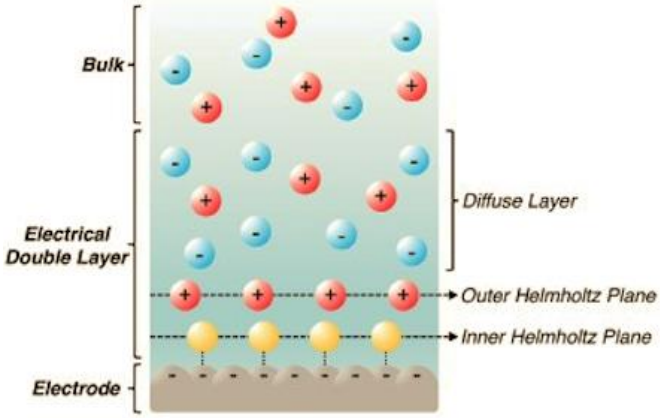

Figure 2.13: Electrical double layer representation

(Dunwell, Yan and Xu, 2018)

The bulk region constitutes the solution surrounding the electrode that is not in the diffusion layer and thus not effected by potentials applied to the electrode. The Outer Helmholtz Plane (OHP) is regarded as being the average radius of solvated ions attracted by an electrostatic force (Lee *et al.*, 2016). Finally, the Inner Helmholtz plane (IHP) is where species are adsorbed are can react. The three modes of mass transfer (migration, diffusion and convection) contribute to the flux of a species approaching an electrode and can be expressed by the Nernst-Planck equation as follows (Bard and Faulkner, 2000):

$$J(x,t) = -D_o \frac{dC_o(x,t)}{dx} - D_o \frac{z_o F}{RT} C_o \frac{d\phi(x,t)}{d(x)} + C_o(x,t)\nu(x,t)$$

The terms in blue represent the diffusion part of the Nernst-Planck equation, the green accounts for migration and the orange is due to convection. To simplify this expression, the migration term can be negated by employing an inert electrolyte. Similarly, the convection term removed when there is no stirring involved in the process (Bard and Faulkner, 2000). Under

these conditions the rate of diffusion of a species through the diffusion layer is governed by Fick's law which simply relates the diffusive flux to a concentration gradient as follows:

$$J(x,t) = -D_o \frac{dC_o(x,t)}{dx}$$

Where, D_o is the diffusion coefficient, and the concentration gradient $\frac{dC_o}{dx}$. The resultant current arising from an oxidative process can then be expressed as a combination of Fick's Law and diffusion limit flux:

$$J(x,t) = -D_o \frac{dC_o(x,t)}{dx} = -\frac{i}{nAF}$$

A CV analysis conveniently allows for categorization of processes that involve electron transfer into (i) reversible, (ii) quasi-reversible and (iii) irreversible. Also by varying the scan rates, the diffusion layer thickness is altered i.e. slow scan rates will result in a thick diffusion layer with a smaller concentration gradient and fast scan rates lead to thin diffusion layers (Aristov and Habekost, 2015).

i. Reversible e^- Transfer

As previously mentioned, an electrochemical reaction is reversible when the Nernst equation is satisfied for both species ie. and applied voltage results in a change in the both species surface concentration. Assuming a linear diffusion layer, the CV curve will result in anodic and cathodic peaks for a reaction that displays reversible electron transfer. The ratio between these peaks will be $\left|i_{p,(anode)}/i_{p,(cathode)}\right| = 1$. The peak currents can be found by applying Randles-Sevcik equation:

$$i_p = (2.69 \times 10^5) n^{3/2} A C_o D_o^{0.5} \upsilon^{0.5}$$

In this equation, i_p (A) is the peak current, n is the number of electrons, A (cm^2) is the surface area, C_o ($mol.cm^{-3}$) is the concentration, D_o($cm^2.s^{-1}$) denotes the diffusion coefficient and υ ($V.s^{-1}$) is the scan rate. Accordingly, a direct relationship exists between peak current and concentration. In this case it can be seen that the peak current varies with the square root of scan rate and so a plot of these should reveal a straight line. This relationship between scan rate and peak current is indicative of reaction which is diffusion limited (Cambiaso *et al.*, 1995). In reversible processes, the current is controlled by mass transport. The slope of $i_p \; vs \; \upsilon^{0.5}$ will be equal the parts in blue for the peak current equation and thus can be used to estimate the diffusion coefficient granted that the number of electrons involved in the process is known.

Deviation for linearity would be due to the possible involvement of a chemical reaction. The peak to peak separation for a reversible one electron process is $59\,mV/n$. A typical reversible is presented in Figure 2.14. From this, the peak potential ($E_{p,f}$) is related to the half wave potential ($E_{1/2}$) and are expressed as follows:

$$E_{p,f} = E_{1/2} - 1.109\frac{RT}{nF}$$

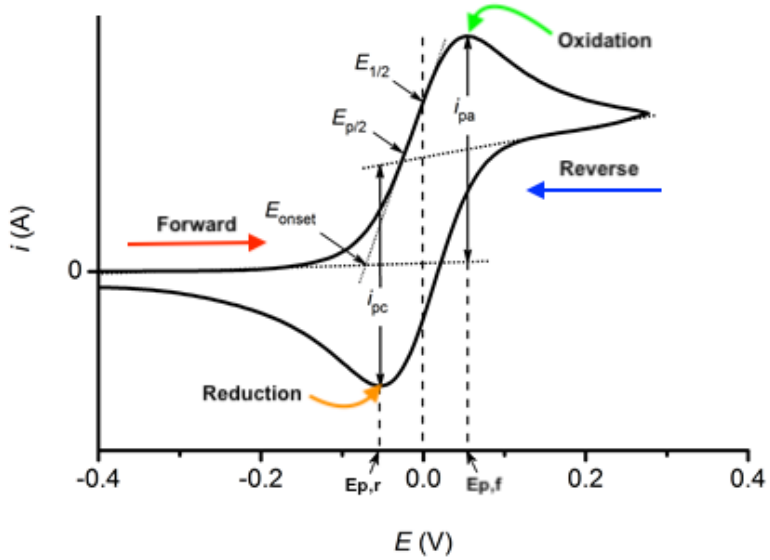

Figure 2.14: CV of a chemically reversible electron transfer process

(Robson, Reinhardt and Bracher, 2021)

The terms in this expression are the same as those previously stated. In the case where the peak appears to be broad, it is useful to use the half peak potential $E_{p/2}$ which is simply the potential where the current half its maximum value $i_p/2$. The equation then becomes:

$$E_{p/2} = E_{1/2} - 1.09\frac{RT}{nF}$$

In combining the latter, and expression relating the peak and half peak potential is acquired as follows:

$$\left|E_{p,f} - E_{p/2}\right| = 2.20\frac{RT}{nF}$$

Finally, the half wave potential ($E_{1/2}$) occurs between the forward ($E_{p,f}$) and reverse ($E_{p,r}$) potentials and can be is:

$$E_{1/2} = \frac{E_{p,f} + E_{p,r}}{2}$$

From the work of Matsuda and Ayabe in conjunction with Nicholson and Shain, the dimensionless parameter Λ was introduced (Nicholson and Shain, 1964). This parameter is a means of relating the standard heterogeneous rate constant to mass transport related process which allows for the convenient determination of the transition phases between reversible and irreversible reactions.

$$\Lambda = \frac{k^o}{m_{trans}} = \frac{k^o}{\left(\frac{\pi n F D_o \upsilon}{RT}\right)^{0.5}}$$

ii. Quasi-Reversible e^- transfer

In this type of system, the current is not only controlled by mass transport processes but also charge transfer kinetics. The CV's present with large peak to peak separation whereby in a one electron process, the $\Delta E_p \approx 60mV/n$ at low scan rates (υ) but increase with increasing scan rate (Bard and Faulkner, 2000). The peak current is not proportional to the square root of the scan rate. Theoretical modeling of a quasi-reversible system is highly complex though with the works from Matsuda and Ayabe along with Nicholson and Shain, it is possible to estimate the k_o rate constant by assessing the difference in ΔE_p (Aristov and Habekost, 2015). The change in peak potential corresponds to a dimensionless parameter Λ though is limited to a $\Delta E_p < 200\ mV$. Upon finding the ΔE_p, Table 2.4 can be used to determine the Λ parameter and depending on the Λ range the reversibility is assessed. A quasi-reversible reaction will retain a Nicholson parameter $10 < \Lambda < 10^{-2}$.

Table 2.4: Works from Matsuda and Ayabe along with Nicholson and Shain correlating ΔE_p with a dimensionless Λ parameter

$\Delta E_p, mV$	60	64	66	68	70	90
Λ	19	5.1	3.63	2.81	2.26	0.77
$\Delta E_p, mV$	100	110	120	130	160	200
Λ	0.57	0.44	0.36	0.295	0.19	0.1

iii. Irreversible e^- Transfer

When electron transfer rates are slow, a system undergoes irreversible electron transfer. In these processes, high potentials are required to drive electron transfer and produce a current. Generally, only a forward or reverse peak is observed on a CV due to this requirement of high potentials which likely occurs outside the potential window. If one was to extend the potential window enough to observe both peaks, the resultant CV (Figure 2.15) would have wide peak separation. Alternatively, high scan rates could unveil the missing peak but often does not lead

to more information about the system. For an irreversible process, the Nernst equation does not apply as the electron transfer processes are too slow which leads to a disequilibrium of the surface species.

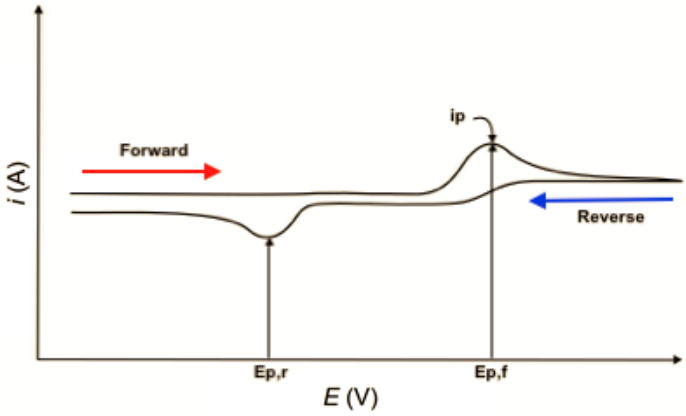

Figure 2.15: CV response to an irreversible electron transfer process

(Robson, Reinhardt and Bracher, 2021)

Processes that exhibit irreversible electron transfer are characterized by a shift in the peak potential with scan rate according to:

$$E_{p,f} = E^o - \frac{RT}{n\alpha F}\left[0.78 + ln\left(\frac{D_o^{0.5}}{k^o}\right) + ln\left(\frac{n\alpha F\upsilon}{RT}\right)^{0.5}\right]$$

Where α is the transfer coefficient and all other terms being previously defined along with their units. The relationship between peak potential (E_p) and half-peak potential ($E_{p/2}$) is:

$$\left|E_{p,f} - E_{p/2}\right| = 1.857\frac{RT}{n\alpha F}$$

The for an irreversible heterogeneous electron transfer process, the peak current in written in terms of a numerical solution to an integral equation is expressed as (Bard and Faulkner, 2000):

$$i = FAC_oD_o^{0.5}\upsilon^{0.5}\left(\frac{\alpha F}{RT}\right)^{0.5}\pi^{0.5}\chi(bt)$$

Where $\chi(bt)$ is a function that varies at any point with $\upsilon^{0.5}$ and C_o. Current functions reveal that a peak will occur at $\pi^{0.5}\chi(bt) = 0.4958$ which is a numerical solution to an integral equation, thus the peak current is found via (Mcauley and Compton, 2012):

$$i_p = (2.99 \times 10^5)AC_oD_o^{0.5}\upsilon^{0.5}n(n' + \alpha_{rds}^{0.5})$$

Here, n refers to the total number of electrons transferred whereas n' denotes the number of electrons transferred before the rate determining step and α_{rds} is the transfer coefficient for the rate determining step. Also, in combining the numerical solution for peak current with the peak potential equation, one arrives at the equation (Bard and Faulkner, 2000):

$$i_p = (0.227)FAC_o k^o e^{[-\alpha f(E_{p,f} - E^o)]}$$

This expression includes the kinetic rate constant k^owhich can be determined through a plot of $ln(i_p)\ vs\ E_{p,f} - E^o$ at different scan rates. If E^o is attainable, this plot will have a slope of $-\alpha f$ and an intercept of k^o. It has been reported that E^o can be estimated through digital simulation via curve fitting (Raziq *et al.*, 2017). Table 2.5 summarizes the overall parameters for system classification.

Table 2.5: Cyclic voltammetric requirements for characterization of electrochemical systems

Parameter	Reversible	Irreversible	Quasi-Reversible
$E_{p,f}$, forward scan peak potential	No change in peak potential $E_{p,f}$ with scan rate υ.	$E_{p,f}$ will shift to higher anodic levels by $\frac{30}{n\alpha}$ for a 10-fold increase in scan rate.	$E_{p,f}$ shifts with scan rate υ.
$\Delta E_p = E_{p,f} - E_{p,r}$	$\Delta E_p = \frac{59}{n}$	NA	ΔE_p approaches $\frac{60}{n}$ at small υ and increases at large υ.
$E_p - E_{p/2}$	$2.2\frac{RT}{nF}$	$1.857\frac{RT}{\alpha F}$	$\frac{d\Lambda}{d(n\alpha)} \times \frac{RT}{F}$
Dimensionless parameter Λ	$\Lambda \geq 15$	$\Lambda \leq 10^{-2(1+\alpha)}$	$10^{-2(1+\alpha)} \leq \Lambda \leq 15$
Heterogeneous kinetic rate constant k^o	$k^o \geq 0.3\upsilon^{0.5}$	$k^o \leq 2 \times 10^{-5}\upsilon^{0.5}$	$2 \times 10^{-5}\upsilon^{0.5} \leq k^o \leq 0.3\upsilon^{0.5}$
Ratio between peak currents $\frac{i_{p,f}}{i_{p,r}}$	$\frac{i_{p,f}}{i_{p,r}} = 1$ Independent from υ.	$\frac{i_{p,f}}{i_{p,r}} > 1$ in the case of reverse scan.	When $\alpha = 0.5$ then $\frac{i_{p,f}}{i_{p,r}} = 1$
Peak current equation i_p	$(2.69 \times 10^5)n^{3/2}AC_o D_o^{0.5}\upsilon^{0.5}$	$(2.99 \times 10^5)AC_o D_o^{0.5}\upsilon^{0.5}n(n' + \alpha_{rds}^{0.5})$	$i_{p(rev)}\mathrm{K}(\Lambda, \alpha)$ where, $0.4463\left(\frac{F^3}{RT}\right)^{0.5} n^{3/2}AC_o D_o^{0.5}\upsilon^{0.5}$

2.5.4. Electrochemical Performance Validation

i) Chronoamperometry

Contrary to cyclic voltammetry (where potential is linearly increased), chronoamperometry is an electrochemical technique that utilizes a potential step and is thus a pulsed potential method. The kinetics of chemical reactions as well as diffusion and adsorption process can be investigated through chronoamperometry. In this method, the potential is stepped from E_1 where there is no oxidation or reduction occurring to E_2 where these reactions are allowed to occur as depicted in Figure 2.16.

At E_1 there is no current flow, upon increasing the potential above the formal potential E^o of the redox couple to E_2 the current that is produced is as a result of the double layer capacitance and electron transfer.

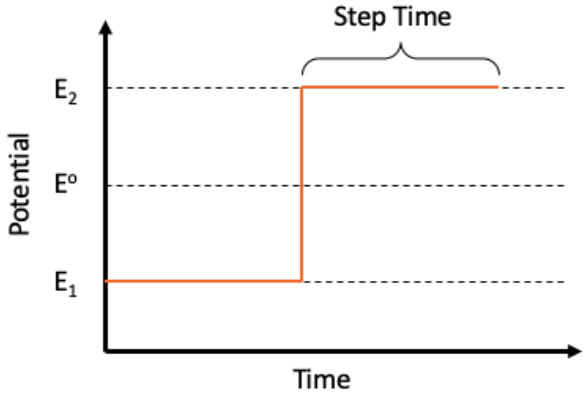

Figure 2.16: Potential step applied over time

It is this current (i) is which is recorded with respect to time (t) following a potential change $E_1 \rightarrow E_2$. The resultant current is thus dependent on the final potential applied and is the reason why the applied potential needs to be carefully selected. Typically, the applied potential E_2 is obtained from CV measurements and is the potential at which the current peak is formed. Chronoamperometric measurements are conducted under constant stirring and applied potential for a set time interval but can be employed using alternative protocols. The current-time response will reflect a change in concentration gradient around the surface of the working electrode. The capacitive current which decays time according to ($i_{cap} \propto 1/t$) can be negated by only considering the final 90% of the i-t data for each step (Gamry, 2021a). This leaves only the faradaic current caused by electron transfer reactions and is related to time via the Cottrell equation (Myland and Oldham, 2004).

$$i(t) = \frac{nFAD_o^{0.5}C_o}{\pi^{0.5}t^{0.5}}$$

Where, n represents the number of electrons, F is faradays constant (96500 C mol^{-1}), the electrodes area (cm^2) is A, the diffusion coefficient D_o (cm^2/s), the analyte concentration is C_o in (mol/cm^3) and t is the time. It is important to note that the Cottrell equation applies to situations where the current is diffusion limited along a planar electrode. The fundamental requirements for comparison between working electrodes is the response time, limit of detection, linear range, sensitivity and selectivity. These can easily be deduced by means of amperometric analysis. The time taken to reach 90% of the final current response represents the response time. Figure 2.17 is a representation of chronoamperometric measurements conducted using a single applied potential and dosing the system with successive addition of

an analyte. These peak currents can be collected and plotted against glucose concentration in a calibration curve to determine the linear range. If a linear range is visible, the corresponding glucose concentrations for those currents represent the linear glucose detection range. The sensitivity is proportional to the slope of the straight line over the linear range. The standard deviation ($\sigma_{X,Y}$) for the blank solution and the corresponding peak currents can be used in determining the detection limit of that sensor.

$$LOD = \frac{3(\sigma_{X,Y})}{Sensitivity}$$

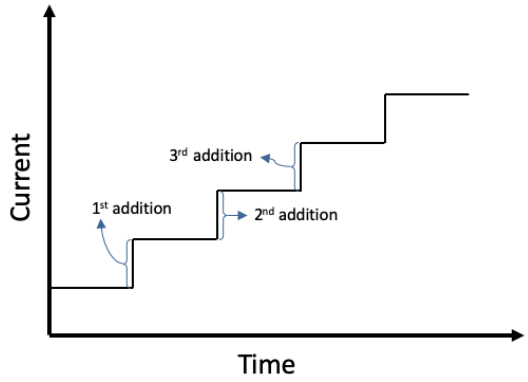

Figure 2.17: Typical staircase chronoamperometric measurement for successive analyte additions

ii) Electronic Impedance Spectroscopy

Unlike voltammetric analysis (CV, Chrono) which drive an electrochemical system beyond its equilibrium conditions, Electrochemical Impendence Spectroscopy (EIS) is a sensitive yet non-destructive characterization technique by employing small perturbations to the system. This method was predominantly used in characterizing the aforementioned electrical double layer and has since increased in popularity finding its application in characterization of electrode interface processes. It is also extensively used in corrosion analysis, battery and fuel cell research. EIS measurements make use of small amplitude sinusoidal perturbations in a system and measure the response (current, voltage or other desired signals). These measurements are made using the same three cell system previously described with the inclusion of a frequency response analyzer. EIS experiments are often carried out via the synthesis of a working electrode which is then placed in a system by which the target analyte is attracted to the electrode surface that affects the systems conductivity. By employing a single perturbation over a large range of frequencies, EIS makes it possible to investigate process exhibiting fast kinetics or slow transport. Here, an AC potential is applied over a electrochemical cell, the electrochemical impedance is measured as a response in terms of an AC current. In organic systems, the molecules are easily denatured upon application of

large voltages whereas inorganic systems offer more leniencies in this regard. A small voltage perturbation introduced to a system in the form of voltage V is represented as follows:

$$V(t) = V_0 \sin(\omega t)$$

Where V_0 represents the voltage amplitude (Volts), $\omega = 2\pi f$ which is the angular frequency in (rad.s^{-1}), f is the frequency in (Hz) and t is the time. The current response associated by such a perturbation will result in a current response (I) at time (t) along with a phase shift equal to (φ):

$$I(t) = I_0 \sin(\omega t + \varphi)$$

Here I_0 represents the current amplitude and the other variables assigned meanings before. With aid from a phasor diagram, the magnitude and phase relationship between current and voltage can be established. A typical phasor diagram involves plotting current or voltage as a vector rotating anti-clockwise about the origin to produce Figure 2.18:

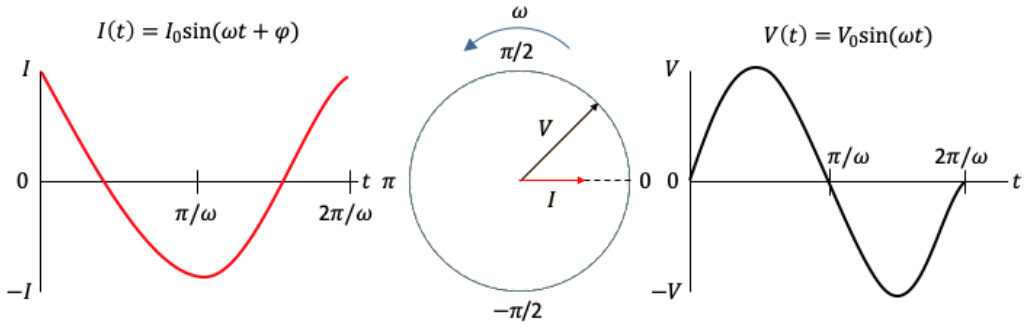

Figure 2.18: Phasor diagram illustrating the relationship between current and voltage in an AC system

According to ohms law, voltage is directly proportional to the current and the resistance as $V = IR$. The resistance in (Ω) as measured by ohms law applies to direct-current (DC) systems which are independent of frequency. In the case of AC systems, the analog of ohms law holds true which as oppose to the resistance term (R), impedance (Z) is used and is also measured in ohms (Ω). Accordingly, impedance can then be described as the opposition to the flow of current. The overall impedance is then simply the ratio between the amplitude of the voltage and that of the current. Impedance is usually a complex number but can contain real elements and so a generalized equation for it can be given as:

$$Z = \frac{V(t)}{I(t)} = \frac{V_0 \sin(\omega t)}{I_0 \sin(\omega t + \varphi)} = Z_0 \frac{\sin(\omega t)}{\sin(\omega t + \varphi)}$$

Where Z_0 is the magnitude of impedance and all other variables being previously defined. As a complex number, impedance can be expressed in the complex plane using polar coordinates with length Z and an angle φ. The latter in conjunction with calculations, the impedance can

be separated into its real (Z') from the imaginary (Z'') parts. To graphically present impedance data, a Nyquist plot is most commonly used. This is a plot of (Z''as the y-axis) and (Z' as the x-axis) as presented in Figure 2.19A. From this plot, the charge transfer kinetics as well as diffusion characteristics can be analyzed. The Nyquist plot for a simple charge transfer reaction is characterized by a semicircle in the high frequency region and a straight line increasing into the low frequency region at 45°. This line in the low frequency region represents Warburg impedance and is the region which is dominated by fast kinetics leaving diffusion as the rate limiting process. Conversely, the high frequency region is limited by slow kinetics and so a semicircle is formed. The diameter of the semi-circle represents the charge transfer resistance R_{CT} in (Ω). The solution resistance R_s is found on the real axis and is independent of frequency. In the kinetically controlled region, the R_{CT} is related to the exchange current (i_o) and subsequently the heterogeneous charge transfer coefficient (k^o) by:

$$R_{CT} = \frac{RT}{nFi_o}$$

$$i_o = nFAC_o k^o$$

This method assumes that the concentration of the bulk is the same as that at the reaction site.

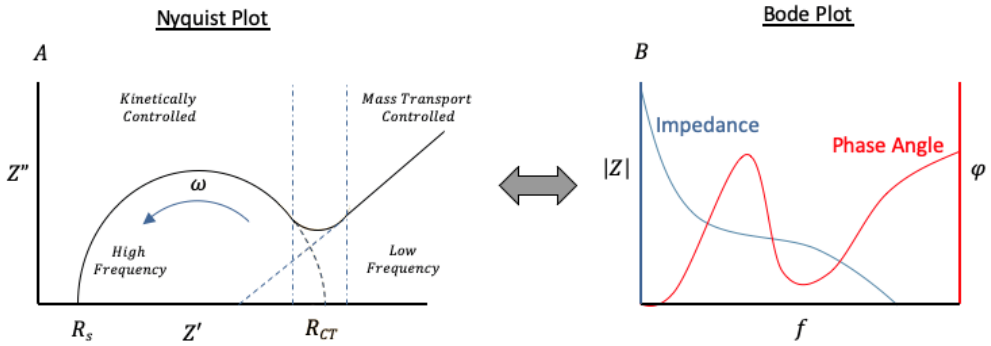

Figure 2.19: Simple charge transfer reaction a) Nyquist plot and b) Bode plot

As illustrated, all frequency information is lost on a Nyquist plot and so to retain this information an accompanying Bode plot is made. Here, frequency is plotted against either the magnitude of impedance $|Z|$ or phase angle φ as per Figure 2.19B. To determine $|Z|$ and φ, the following equations can be used:

$$|Z| = \sqrt{(Z')^2 + (Z'')^2}$$

$$\varphi = \tan^{-1}\left(\frac{Z''}{Z'}\right)$$

Although the difference between actual resistance and impedance has been established, it's convenient to represent EIS data in terms of equivalent circuits. These circuits consist of electrical elements including capacitors, resistors, inductors and ad-hoc elements such as

constant phase elements and Warburg elements. By combing these elements into an equivalent circuit, it is possible to model EIS data to define the system. Each element can be expressed as a complex mathematical function which represents its impedance contribution. The impedance for circuit elements is summarized in Table 2.6:

Table 2.6: Circuitry elements present in common equivalent circuits

Impedance Type	Symbol	Equation
Resistor	Z_R	$Z_R = R$
Capacitor	Z_C	$Z_C = \frac{1}{j\omega C}$
Inductor	Z_L	$Z_L = j\omega L$
Constant Phase Element	Z_{CPE}	$Z_{CPE} = \frac{1}{y_o(j\omega)^n}$
Warburg Element	Z_W	$Z_W = \frac{1}{y_o\sqrt{j\omega}}$

The impedance for a resistive element is the only element that does not include an imaginary part whereas capacitors, inductors, CPE's and Warburg elements only include the imaginary part. This makes it possible to identify the resistance very easily by just interpreting the Nyquist plot. For the aforementioned imaginary parts, the unreal number $j = \sqrt{-1}$ and ω is the angular frequency in (Hz.s^{-1}). In a capacitive element, C represents the capacitance (F). For an inductor, L is the inductance in (H.s). A constant phase element (CPE) is the imperfect equivalent of a capacitor and from its equation it can be seen that when the exponent $n = 1$, the CPE equation will be the same as that of the capacitor. The y_o term for the capacitor thus represents the capacitance for a CPE. On the contrary, for a Warburg element the y_o term contains information related to the diffusion coefficient. As in Figure 2.20, when elements are in series, their impedance's can simply be added together however when in parallel, the total impedance (Z_{tot}) is found by inverting the sum impedance and finding the common denominator.

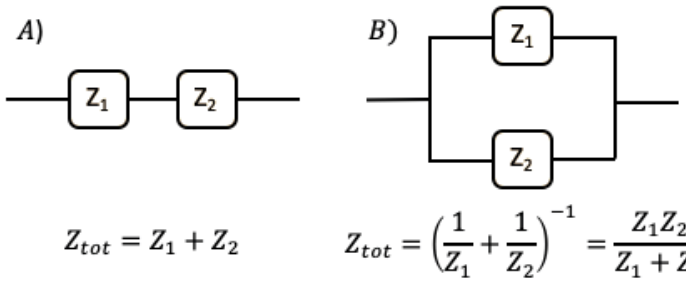

Figure 2.20: Circuits depicting a) series configuration and b) parallel configuration

iii) Transient Photoconductivity

It is well known that a semiconductor becomes more electrically conductive when it absorbs electromagnetic radiation with sufficient energy in the form of visible light, ultraviolet light and

gamma radiation. This phenomenon is known as photoconductivity and has played a significant role in functional material research. A materials ability to conduct electricity increases when exited electrons jump from the valence band into the conduction band leaving behind a hole in the valence band. The free electron hole pairs generated give rise to increased photoconductivity which is highly dependent on carrier densities and the process of carrier formation, trapping and recombination. In addition, photoconductivity is temperature dependent however is also strongly influenced by light intensity, and applied field in the form of a potential bias. By studying the photoconductive behavior of materials under various conditions such as light intensity, temperature, frequency, time and concentration, the charge carrier generation, transport and recombination characteristics are uncovered.

In a three-electrode setup, when light is incident on the working electrode surface, photogenerated charge results in a current which is measured against time. Transients arise from perturbations imposed on a system via an interrupted supply of light (light on, light off). The response time to and from the old and new system equilibrium position in a light on light off disturbance can be used to define transport parameters. Also, the relationship light intensity shares with the measured photocurrent with associated rise and decay times allows for a better understanding about the traps involved in a given system. In cases where the free carrier concentration deviates even after the light source is removed, Persistent photoconductivity (PPC) is the cause. This phenomenon is known to occur in many semiconductors though the reasons for its occurrence vary. Most often the existence of PPC is attributed to bi-stable defects between the deep and shallow energy state (Guillén and Herrero, 2018). Transients arise from the perturbations imposed on the system and the photogenerated charge results in a current which is measured against time. As previously described, the time difference between the old and new system equilibrium states can be used to define the transport parameters. The photogenerated transients were modeled using the triphasic stretched exponential function as depicted by.

$$I = i_o + A_1\left(e^{\frac{-t}{\tau_1}}\right) + A_2\left(e^{\frac{-t}{\tau_2}}\right) + A_3\left(e^{\frac{-t}{\tau_3}}\right)$$

Here, A represents a dimensionless weighting parameter associated with the amplitude of the photoinduced response, t denotes the time, i_o represents and τ is the decay time constant for each exponential term as per previous works (Li *et al.*, 2011, 2014). It is understood that e^-/h^+ pairs which are generated in the bulk crystallites will recombine according to radiative or Shockley-Read-Hall mechanisms. Free electrons which are not able to recombine with holes result in holes being captured in deep trap states. Once illumination is cut off, holes emerge from these traps and recombine with electrons thus causing a decrease in the current density.

CHAPTER 3

EXPERIMENTAL PROCEDURES AND ANALYSIS TECHNIQUES

3. Introduction

The following chapter provides detailed descriptions of the various physical as well as how the electrochemical analysis techniques were employed in this work. Section 3.1 focuses on the synthesis procedure along with the materials used in the synthesis process. Section 3.2 describes the electrochemical testing apparatus while Section 3.3 covers the relevant theory associated with the physical characterization methods.

3.1. CuO Thin-Film Synthesis

The synthesis process commenced as per the following procedure using the below materials.

3.1.1. Materials

Copper Cyanide (CuCN), Sodium Cyanide (NaCN), Sodium Carbonate (Na_2CO_3), d-(+)-Glucose, Ascorbic Acid (AA), Sodium Hydroxide (NaOH), Fructose, Sucrose, Sodium Chloride (NaCl), Uric Acid (UA), Citric Acid (CA), Acetaminophen and Fluorine doped Tin Oxide (FTO) glass were purchased from Sigma Aldrich South Africa and used without any further purification.

3.1.2. Synthesis procedure

The CuO photocatalyst synthesis involved the optimization of three separate processes Electrodeposition, Calcination and Etching. The FTO glass sheet was cut into slides with dimensions (4 x 1.5 cm). These slides along with all glassware and stirring beads were ultrasonically cleaned first with degreaser for 15 min, then a mixture of ethanol and acetone for another 15 min and finally sonicated in deionized water. The glassware and slides were then dried in a convection oven operating at 60 ℃ for 4 hours. Electrodeposition of a CuO layer from a known cyanide strike solution containing 0.036 M CuCN, 0.067 M NaCN and 0.014 M Na_2CO_3 was carried out at 4 V for 2 min. The anode and cathode used were both cleaned FTO glass slides submerged 2 cm into the solution and separated by a constant distance of 4 cm. The FTO slides with the electrodeposited were annealed in a furnace for 1 hour at 450 ℃ thus creating a thin CuO layer. After allowing the samples to cool to room temperature, they were placed into vials containing enough NH_3 at 25% (V/V) to cover the metal oxide layer for 2 min.

The slide were rinsed with deionized water and allowed to dry in the air before being placed into a clean vial prior to testing. An overview of the synthesis procedure is presented in Figure 3.1.

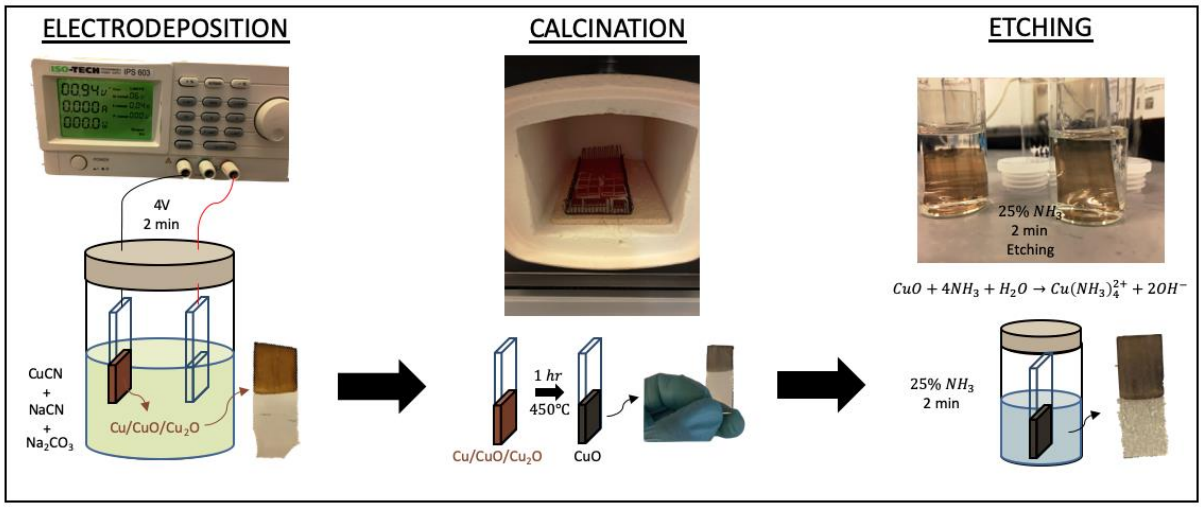

Figure 3.1: Overall synthesis procedure prior to testing

3.2. Electro-analytical Experiment Apparatus

An electro-analytical system has many configurations and is comprised of a number of individual components to produce qualitative results. For the purposes of this thesis, only a three-electrode cell is considered. The hardware includes a potentiostat to run and control the experiments. A cell which is comprised of a working electrode (WE), a counter electrode (CE) and a reference electrode (RE) which are immersed in a electrolyte solution with or without other species. The working electrode is the most important component in an electrochemical cell as it is at this interface (electrode-analyte) where reactions occur via facilitation of electron transfer. In this case, FTO glass with electrodeposited CuO acts as the working electrode. The reference electrode is used to measure the potential at the working electrode without allowing a current to pass. It is highly stable and consists of a redox system (Ag/AgCl) with a well-defined electrode potential (Gamry, 2021b). Finally, the counter electrode (Pt-wire) completes the circuit by balancing the current produced at the working electrode. The three-electrode system is connected to a potentiostat that's operation is governed by user defined inputs via a computer program (Nova 2.0). The overall system configuration is illustrated in Figure 3.2.

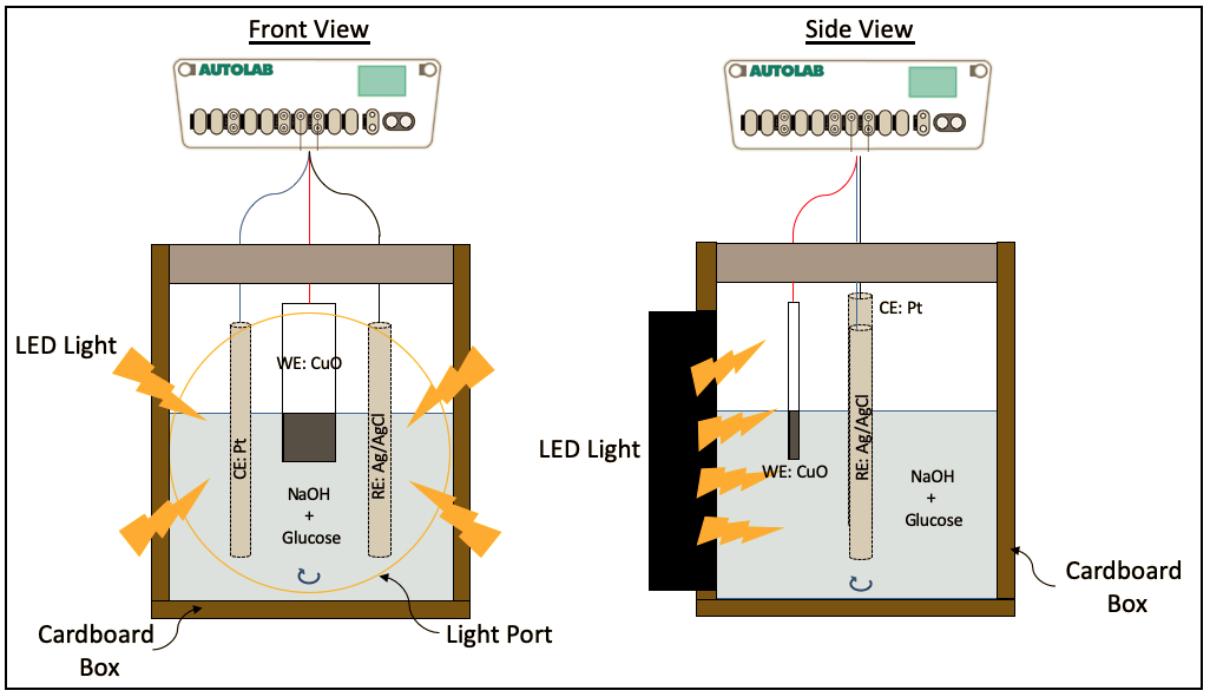

Figure 3.2: Overall electrochemical analysis system

3.3. Physical Characterization

The relevant physical characterization techniques and their associated theory is presented in this section.

3.3.1. Hall Effect

Hall Effect offers an experimental approach to investigate the motion of charge carriers. Hall Effect measurements on a semiconductor provides information regarding charge carrier densities as well as the type of conductivity it exhibits (n or p type). In this method, the behavior of free charge carriers is assessed by monitoring the Lorentz force by applying an electric or magnetic field.

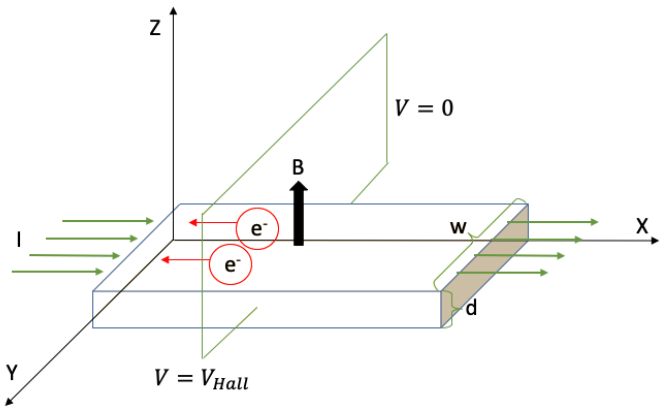

Figure 3.3: Depiction of the Lorentz force induced when charge flows

In n-type semiconductors, the majority charge carriers are due to electrons (e^-) whereas p-types exhibit a predominantly hole (h^+) rich carrier concentration. As depicted in Figure 3.3, current i will flow in a straight line along the x-axis in the absence of a magnetic field. When a magnetic field B is introduced, electrons move perpendicular to the applied field. Electrons are subject to a Lorentz force which causes the electrons to drift from their straight-line path across the width w in the negative y-axis direction. Electron drift leads to the charge accumulation on the planar sides. The Lorentz force F is calculated by:

$$F = q(E + \upsilon B)$$

Where the elementary charge is q (1.602×10^{-19}), E is the electric field and υ represents the velocity. A potential drop or Hall voltage (V_H) across the planers width can be measured as a result of the flow of charge. A positive Hall voltage indicates predominant hole carriers whereas majority electron carriers exhibit a negative potential (Zeghbroeck, 2011a).

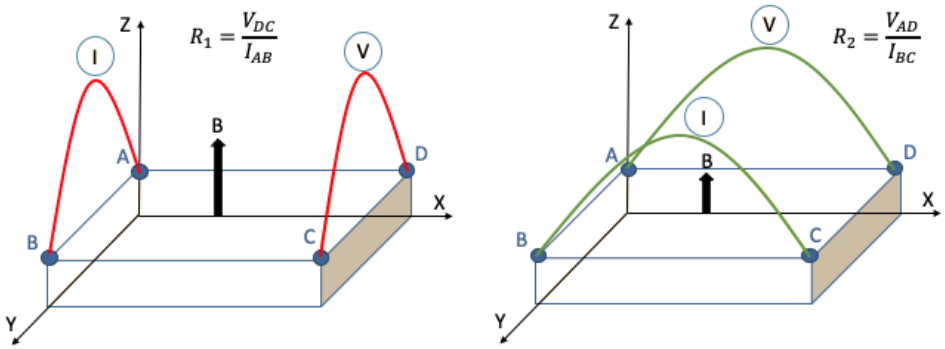

Figure 3.4: Illustration of the Van der Pauw configuration

To determine charge carrier mobility (μ) and sheet carrier density (n_s), the Van der Pauw technique is applied which combines resistivity and Hall measurements (National Institute of Standards and Technology, 2019). In this technique, two characteristic resistances (R_1 and R_2) form the overall sheet resistance R_S and are calculated as per Figure 3.4. A current is passed between points (A-B) while simultaneously measuring the potential difference across points (D-C). Following this measurement, current is then allowed to flow between points (B-C) with a voltage measurement between (A-D). Alternatively, Van der Pauw's iterative equation can be applied:

$$1 = e^{\frac{-\pi R_1}{R_S}} + e^{\frac{-\pi R_2}{R_S}}$$

The mobility is then:

$$\mu = \frac{|V_H|}{iR_sB} = \frac{1}{qn_sR_s}$$

The sheet resistance is related to bulk resistivity (ρ) by the expression $\rho = R_s d$. According to Figure 3.5, the potential difference across (B-D) represents the hall voltage. The sheet carrier density can be experientially determined via a multiple hall voltage measurement in both directions to all points under a constant magnetic and electric field.

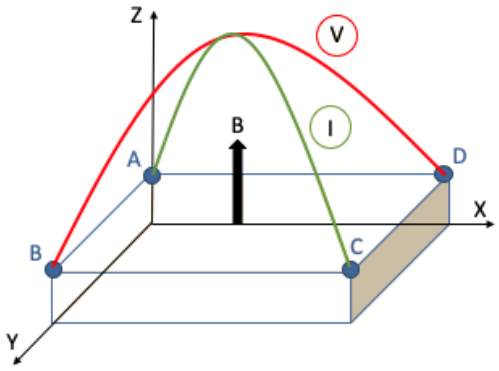

Figure 3.5: Four-point connector hall voltage experimental set-up

The hall voltage (V_H) can be calculated by applying:

$$V_H = \frac{iB}{qn_s}$$

Where i is the applied current in the magnetic field B and q is (1.602×10^{-19}). The sheet carrier density (n_s) is related to the bulk carrier density (n) by $n = \frac{n_s}{d}$ where d is the thickness. The overall hall voltage is then, $V_H = \frac{V_{BD}+V_{AC}+V_{DB}+V_{CA}}{8}$.

3.3.2. SEM

Scanning Electron Microscopy (SEM) is an indispensable physical characterization technique which enables surface morphology and topographical studies of nanosized materials. In this method, high energy beam of electrons are fired at a samples surface in a raster configuration under high vacuum. These electrons penetrate the surface of the material and in doing so, interact with the atoms. Depending on the interaction of the electrons with the atoms, signals are recorded in the form of secondary electrons, backscattered electrons, X-rays or light.

Backscattered electron signals are recorded during SEM scans when the incident beam of high energy electrons forms inelastic collisions with the nuclei of atoms at the surface. Under these conditions the electrons scatter from the surface and those which experience low energy loss during this process are backscattered electrons. The amount of back scattered electrons is highly dependent on the atomic weight of the atoms involved in the interaction. SEM image resolutions will thus decrease with increasing atomic number. In the case of secondary

electrons, the incident electron beam interacts with the valence electrons of the atoms inelastically which subsequently liberates electrons with low energy following migration to the samples surface (Bijoor, 2006). Due to the energy differences between back scattered and secondary electrons, different detectors are used to develop a SEM image. Both back scattered and secondary electrons together form the basis of a high resolution SEM images and are detected via a photomultiplier and light guide.

In some cases, scanning electron microscopes can be fitted with an energy dispersive X-ray spectroscope (EDS). The electron beam excites the atoms on the surface of a sample which emit X-rays of specific wavelength which are characteristic of its atomic structure. Thus EDS is the standard method employed to both identify and quantify elemental compositions of a sample (Ebnesajjad, 2014). The detector converts X-rays into proportional voltages which are processed and analyzed using software which correspond energy peaks to particular elements. Also, visible light can be reflected from a samples surface when cathode ray tubes are used to illuminate a sample. Cathodoluminescence detectors harvest the reflected light to produce color images of the elements in the sample.

3.3.3. Raman

Raman spectroscopy is spectral analysis technique that utilizes inelastic scattering of incident radiation on molecules. A laser of particular wavelength illuminates a sample which causes molecules to vibrate and scatter light at specific frequencies. The scattering is measured perpendicular to the incident monochromatic light. Most of the scattered light has a similar frequency to that of the incident laser beam ($V_s = V_i$) which represents Rayleigh scattering. Raman scattering occurs when the frequency of an incident beam is different to the scattered radiation. In cases where the scattered beam displays a lower frequency ($V_s < V_i$), anti-stokes lines are evident on a Raman spectrum whereas Stokes lines appear in cases of higher frequency ($V_s > V_i$) as electrons absorb energy as presented in Figure 3.6. The transition from lower to higher vibration energy in Stokes shifted bands reveal sharp characteristic peaks (Paršin, 1976). Anti-Stokes shifted bands are particularly useful in florescence studies however the standard approach to measuring Raman spectra make use of Stokes bands. The magnitudes of the peaks are independent of the incident beams wavelength though the scattering is (Settle, 1997). The peak positions offer a means of identification of the molecule present in a sample and so can be used for characterization purposes.

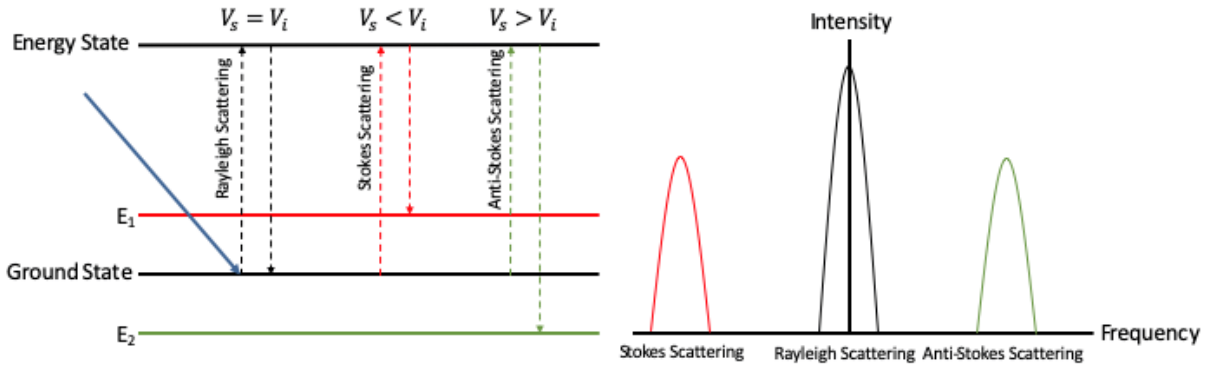

Figure 3.6: Raman scattering energy diagram and Raman spectra

3.3.4. X-ray Diffraction

X-ray diffraction (XRD) is an analytical technique which offers phase identification as well as provides information regarding crystallinity, lattice parameters, crystal structure and size of the sample. This method utilizes constructive interference caused by monochromatic X-rays which scatter at specific angles. Bragg's law describes the inter-atomic interaction between the atoms and X-rays as follows: $n\lambda = 2dsin\theta$. Where n represents the order of reflection, λ is the X-ray wavelength, d is the interplanar spacing and θ is the angle of incidence as presented in Figure 3.7.

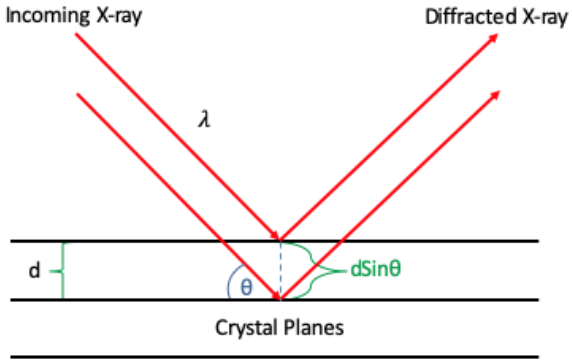

Figure 3.7: Double beam diffraction from two atoms in crystal plane

The diffracted X-rays are detected and counted over a range of 2θ angles to include all diffraction angles as determined by the unit cell. The intensity is dependent on the distribution of electrons within said unit cell and so in electron dense regions, high intensities are recorded.

3.3.5. X-ray Photoelectron Spectroscopy

X-ray photoelectron spectroscopy (XPS) is a spectroscopic technique that is widely used in surface chemistry to assess the surface composition and charges associated with them. A beam of X-rays with known power irradiates a samples surface under high vacuum while the kinetic energy of the escaping electrons are recorded as depicted in Figure 3.8. The energy of the electrons is then converted to binding energy by applying the following equation:

$$Binding\ Energy, (eV) = E_{Photon} - \Phi E_{kinetic}$$

Where E_{Photon} represents the energy of the X-rays, Φ represents the work function which is particular to the spectrometer being used and $E_{kinetic}$ is the energy associated with the leaving electrons from the samples surface. These binding energies correlate with specific elements and can also be attributed to specific valence shells from which the photoelectrons were ejected to provide information regarding the valency.

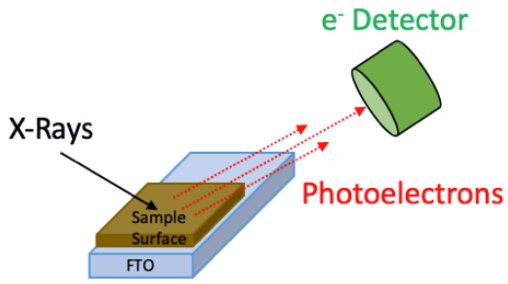

Figure 3.8: Depiction of XPS measurement process

3.3.6. UV-Vis

Diffuse reflectance is commonly used in UV-vis regions to provide information regarding the molecular structure of a given sample. The reflectance spectrum is obtained by recording the reflection of electromagnetic radiation with respect to frequency or wavelength. The interactions between UV light and a catalysts surface is complex as light is both absorbed and scattered simultaneously. The band gap of a semiconductor is the amount of energy required to excite and electron from the valence band into the conduction band. The optical band gap of semiconductors can be evaluated using the theory from Kubelka and Munk (Makuła, Pacia and Macyk, 2018). Because the Tauc method assumes the absorption coefficient (K) is energy dependent, it may be replaced with a ratio of (K) and the scattering coefficient (S). From the reflectance spectra, the ratio (K/S) was determined by applying the following relationship.

$$F(R_\infty) = \frac{K}{S} = \frac{(1 - R_\infty)^2}{2R_\infty}$$

Where $R_\infty = \left(\frac{R_{Sample}}{R_{Stardard}}\right)$ represents the reflectance of a sample with infinite thickness, K denotes the absorption coefficient whilst S is the scattering coefficient. Upon substitution of this ratio into the Tauc relation, the following equation is obtained.

$$\left(\frac{K}{S}(h\upsilon)\right)^n = B(h\upsilon - E_g)$$

Here, h is planks constant, υ is the photon energy, B is a constant and E_g is the band gap. The n power is especially important as this defines the nature of the electron transition which is associated with direct or indirect bands. When $n = 2$, a “direct allowed” band structure is present and if $n = 0.5$, and “indirect allowed” band structure prevails. However, n can also be 2/3 in which case the transition is “direct forbidden” and also 1/3 for “indirect forbidden”.

CHAPTER 4

RESULTS AND DISCUSSION

4. Introduction

This chapter accounts for the interpretation and reporting of experimental data. Section 4.1 covers the synthesis optimization for the fabrication stages in order of which they were experimentally determined. Section 4.2 discusses the physical characterization (XRD, XPS, SEM, Hall Effect, UV-Vis) of selected samples. The electrochemical study (CV and EIS) findings are presented in Section 4.3 while Section 4.4 covers the charge transfer characteristics. The sensor performance is analyzed in under section 4.5 and the transient photocurrent is analyzed in Section 4.6.

4.1. Synthesis Optimization:

The synthesis process of this unique photocatalytic CuO film was carried out via the optimization of three simple process electrodeposition, calcination and etching.

4.1.1. Electrodeposition Time/Voltage Study

The overall synthesis process of the CuO photocatalyst involved the optimization of three separate process (Electrodeposition, Calcination and Etching). Electrodeposition of a thin CuO layer from a known cyanide strike solution containing 0.036 M CuCN, 0.067 M NaCN and 0.014 M Na_2CO_3 was carried out. The sequence of reactions to deposit a thin CuO film onto the FTO substrate is believed to proceed is as follows:

$$Cu(CN)_n^{(n-1)-} + 2(n)OH^- \rightarrow Cu^+ + (n)CNO^- + (n)H_2O + 2(n)e^-$$

$$2Cu^+ + 2OH^- \rightarrow Cu_2O + H_2O$$

$$Cu_2O + 2OH^- \rightarrow CuO + 2H_2O + 2e^-$$

As previously reported in other electrochemical deposition works, the deposition voltage and time play a critical role in the overall peak current density of a given sample. The deposition voltages investigated were 2 V, 3 V, 4 V and 5 V over a time (min) of 0.5, 1, 2 and 4 respectively. All these samples were calcined at 350℃ for 2 hours as a preliminary temperature and time. Cyclic voltammetry (CV) experiments were conducted to determine the optimum deposition voltage and corresponding time. These studies were conducted in a alkaline medium (0.1 M NaOH) both in the presence and absence of glucose (1 mM) with and without

illumination. As previously mentioned, NaOH was incorporated to negate the effects of the migration term in the diffusion equation. In addition, glucose is non-conductive as it dissolves in water but does not dissociate. In an effort to counter this, NaOH bridges the gap and allows for a conductive solution. Human blood also slightly basic with a pH of approximately 7.4, thus incorporation of NaOH during testing is a commonly accepted practice (Weatherspoon, 2019). The CV's conducted in the dark were performed in an optical glass box housed in cardboard to block illumination of the sample from ambient light. The same cardboard housing was used for samples undergoing illumination though a cut out in the box. Evaluation of the optimum electrodeposition voltage and time was done by comparing the difference in anodic peak currents between the light and dark conditions at various scan rates.

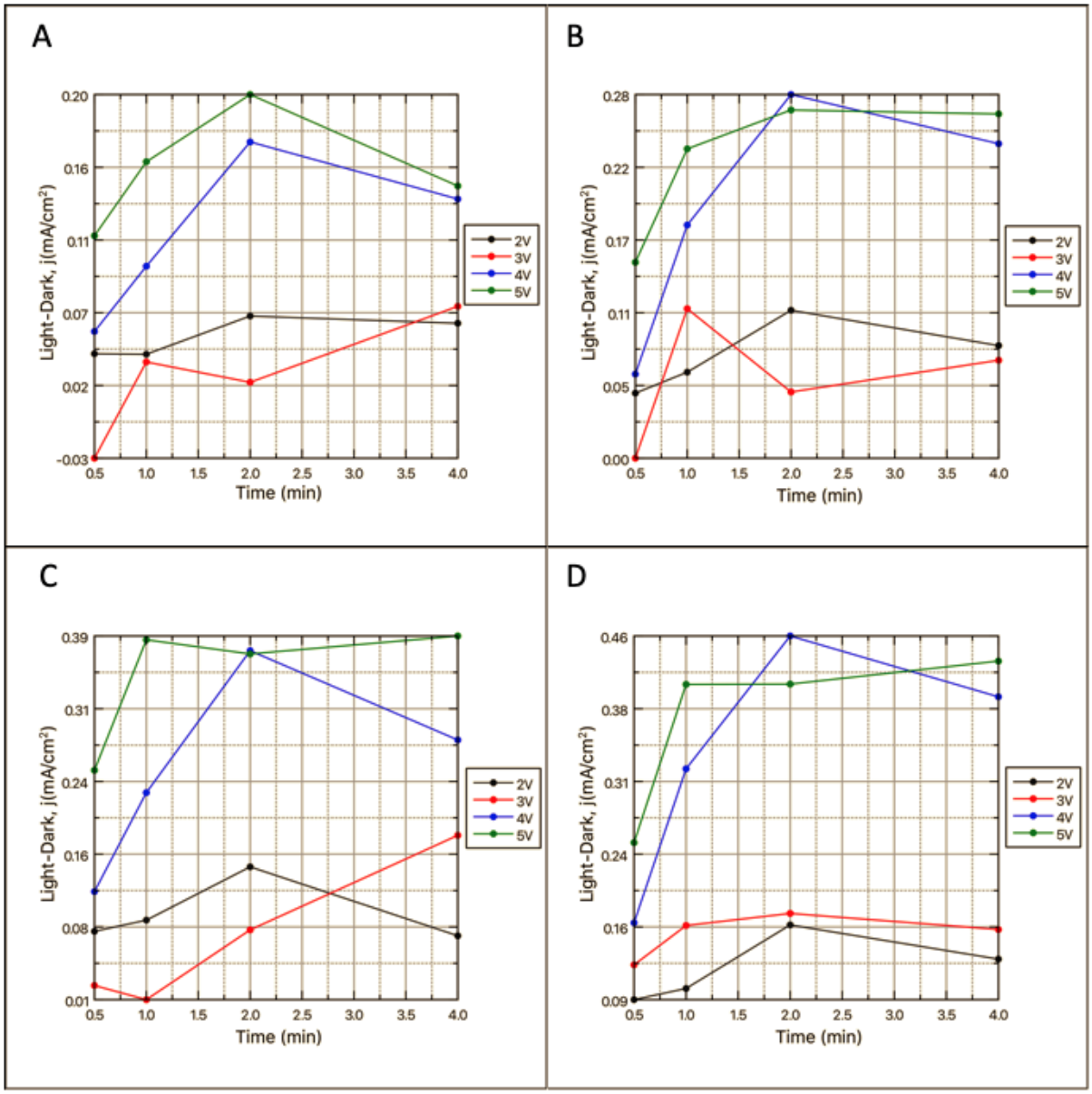

Figure 4.1: Difference between light and dark anodic currents in 1 mM glucose for various electrodeposition voltages and times at A) 25 mV/s, B) 50 mV/s, C), 100 mV/s and D) 200 mV/s

In the absence of 1 mM glucose, there are no observable oxidation or reduction peaks in CV measurements. The relationship between electrodeposition parameters is portrayed in Figure

4.1 relative to the respective difference in anodic current density in the light and dark. It can be seen that an electrodeposition voltage of 4-5 V produces the greatest difference in current density between the light and dark in all scan rates. Although a 5 V deposition voltage shows an increased difference in current density at 25 mV/s scan rate, the films produced at this voltage are inconsistent. Also peeling of the films occurred at this condition at longer deposition times signaling adherence problems. This may be as a result of the high-speed nucleation oxygen gas bubbles forming on the surface which both hinder binding to the FTO substrate.

The films deposited at lower voltages (2-3 V) appeared thin with good adhesion which was tested via a simple scratch test. When comparing the electrodeposition time to the deposition voltage it can be seen that the combination of 4 V at 2 min consistently produces a higher difference in current density irrespective of scan rate. As a result, this combination was selected as the optimized electrodeposition parameters and all further samples are synthesized according to these findings.

4.1.2. Calcination Time/Temperature Study

In a study by Chandrappa and Venkatesha regarding the characterization of CuO nanoparticles, they found that CuO crystals began to nucleate at calcination temperatures above 350℃ though complete crystal formation occurred at 660℃ (Chandrappa and Venkatesha, 2013). At lower temperatures, a mixed Cu phase would persist. This mixed phase has been known to produce impressive photocurrents and so by expanding the thermal oxidation temperature range of investigation, it is possible to compare the difference between the light and dark current produced for the various synthesis conditions. The optimum calcination temperature and time was found by comparing the difference between the light and dark peak current density over 100, 250, 350, 450, 550 and 650 ℃ for 1, 2, 3 and 4 hours respectively. The CV measurement was carried out under the same conditions as previously established.

The calcination temperature ranges as well as times were chosen because of their prevalence in literature with studies regarding CuO. In all cases with the exception of the 200 mV/s scan in Figure 4.2, the shorter calcination times produced the best difference in peak anodic currents. Low temperature calcination consistently yielded smaller peak differences for example in the following order (100 ℃ < 250 ℃ < 350 ℃) at 50 mV/s and 1 hour. A 650 ℃ calcination produced mediocre photocurrents and, in some cases, very similar to the low temperature calcinations. The two most impressive temperatures were 450 ℃ and 550 ℃ respectively. Of these, 450 ℃ for 1 hour feature the highest difference in photocurrents over the full range of scan rates. It is possible that thermal oxidation at this temperature exposes

particular facets which offer enhanced photocatalytic glucose degradation. Also, it is known that the crystallite size increases with increasing calcination temperature (Chandrappa and Venkatesha, 2013). The fact that increasing the temperature above 450 ℃ results in similar or even decreased performance is an indication that the crystallite size is an important factor to consider. With these findings, a calcination temperature of 450 ℃ and time of 1 hour was selected and used as the optimum conditions for this step. These parameters were unchanged during further studies.

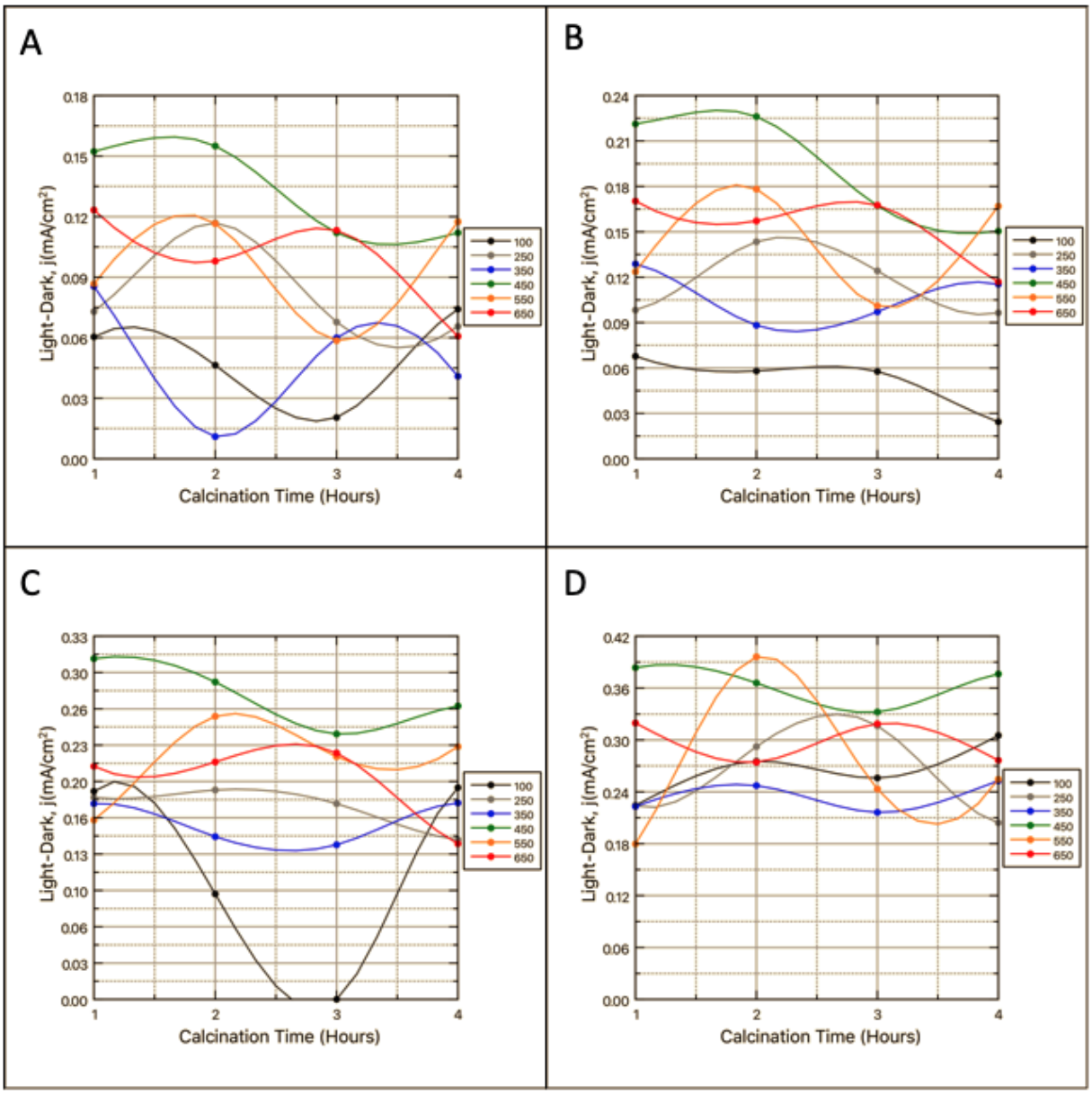

Figure 4.2: Calcination temperature/time optimization using the difference in anodic peak current between dark and light in 1 mM Glucose at A) 25 mV/s, B) 50 mV/s, C) 100 mV/s and D) 200 mV/s

4.1.3. Etching Time Study

Wet chemical etching is a process whereby a materials surface layer is removed via a liquid (etchant). In this process, multiple chemical reactions occur to remove the reactants the

surface layer which forms new species. The mechanism involved can be described by three stages (1) Diffusion of etchant to the materials surface, (2) chemical redox reaction which oxidizes the top layer and (3) Diffusion of the redox products away from the surface. The morphology of the crystalline material being etched greatly impacts the etching rate. Also, the etching process is known to further improve the electrochemical properties of CuO nanomaterials (Wang, Han and Tao, 2007; Zhu and Panzer, 2016). In particular, NH3 as an etchant is abundantly researched because of its limited etching rate towards copper-based oxides. Thus, experiments were conducted to determine (if any) the increase in current density after subjecting calcined samples to NH_3 etchant of a single concentration 25% (V/V) over various times 1, 2, 4 min respectively. According to the Pourbaix diagram (Figure 4.3) for a Cu-H_2O system at low Cu concentration, the solubility is very low and so to promote solubility an oxidizing environment is required. As a noble metal, copper metal is not directly etched by ammonia but rather reacts with copper oxides such as CuO and Cu_2O. The dissolution of CuO in NH_3 occurs according to the following equation:

$$CuO + 4NH_3 + H_2O \rightarrow Cu(NH_3)_4^{2+} + 2OH^-$$

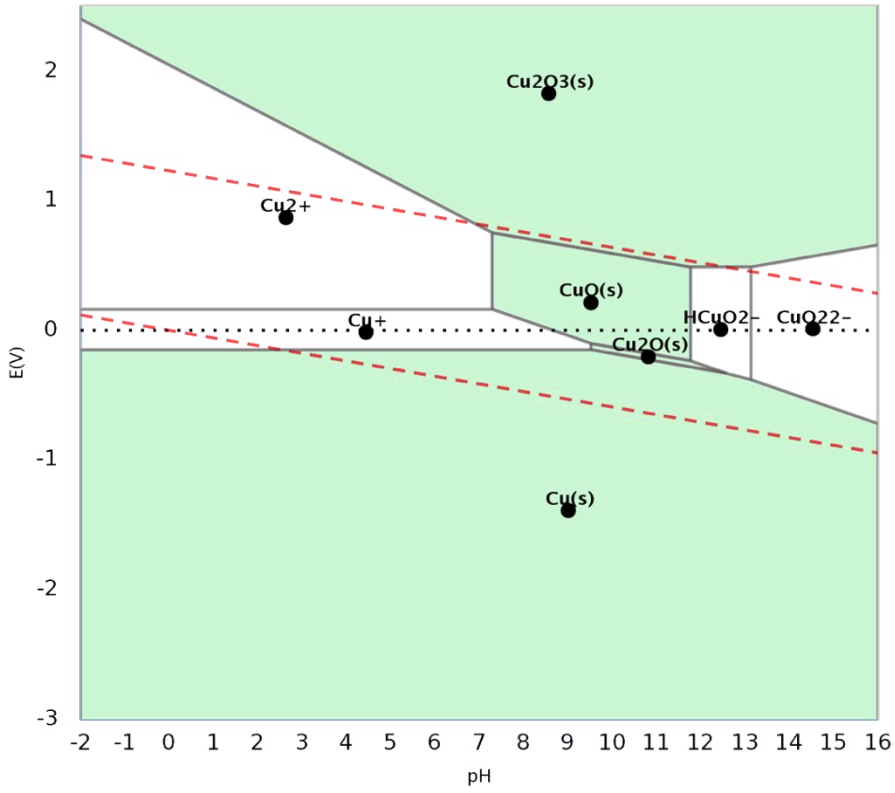

Figure 4.3: Pourbaix diagram for a Cu-H_2O system

(Materials Project, 2021)

This however in not representative of the true dissociation as liquid ammonia is in equilibrium with the ammonium ion:

$$NH_3(aq) + H_2O(l) \leftrightarrow NH_4^+(aq) + OH^-(aq)$$

In addition, with dissolved oxygen in solution, the dissociation of CuO in ammonia solution forms a cupric-ammine species (Figure 4.4) as follows:

$$CuO(s) + 4NH_4^+(aq) \rightarrow Cu(NH_3)_4^{2+}(aq) + H_2O(l) + 2H^+(aq)$$

Following desorption from the CuO surface, the $Cu(NH_3)_4^{2+}$ is in the aqueous phase meaning some amounts of copper has been effectively removed from the surface of the material. This finding is also shown in SEM images with a decrease in layer thickness post etching.

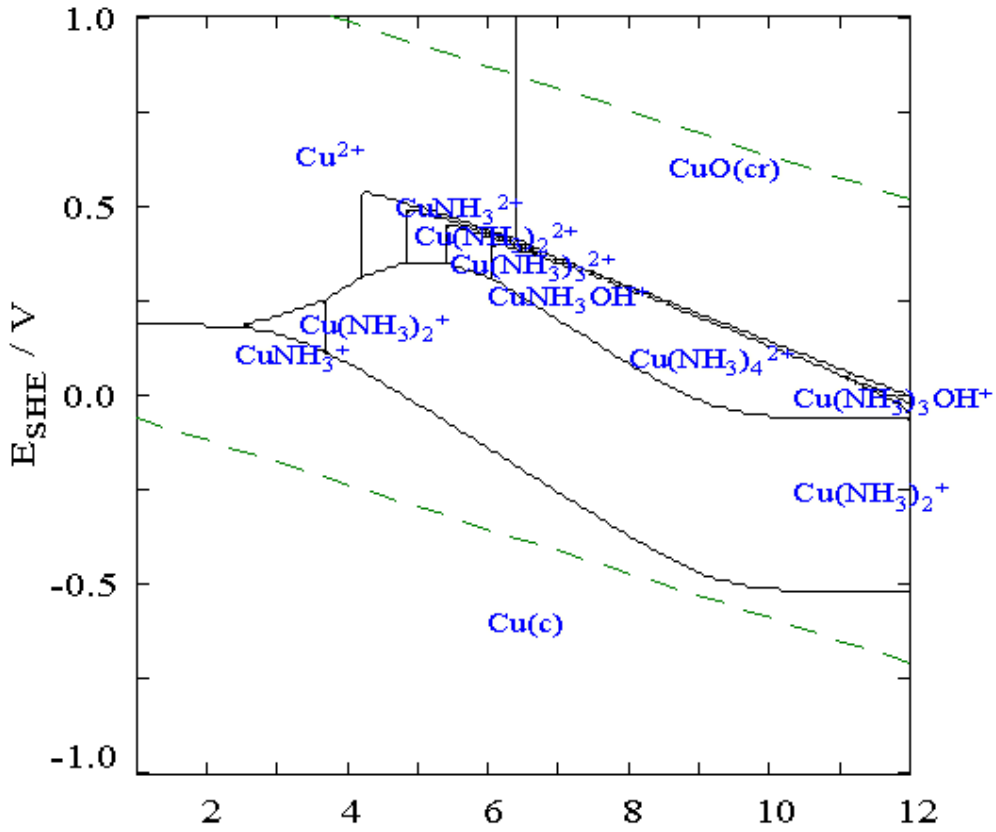

Figure 4.4: Pourbaix diagram for a Cu-NH3-H_2O system at NH3 = [10M]

(en-academic, 2021)

Accordingly, a set volume (5 mL) of concentrated NH_3 solution was added to a vial containing the calcined slides and the timer started. It was found that by exposing the calcined CuO photoelectrode to NH_3 for 2 min improved the current density by 0.43 mA/cm^2 as presented in Figure 4.5. Though this increase in performance is not revolutionary, the decrease in band gap (shown in chapter 4) is of great importance along with other distinct enhanced features. This is covered in more detail in the following section. All further tests were conducted using these optimized values unless stated otherwise.

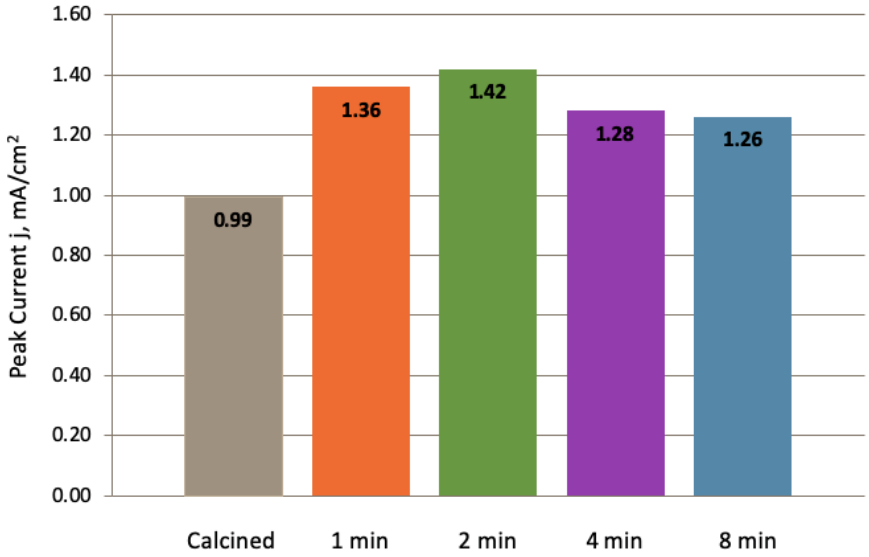

Figure 4.5: Optimization of the NH_3 etching stage

4.2. Physical Characterization

4.2.1. X-ray Diffraction

Phase identification was done using X-ray diffraction (XRD). The “etched” samples were characterized using a Cu-$K\alpha$ radiation source at an operational tube voltage of 45 kV and a current of 40 mA. The diffraction patterns were collected at increments of 0.02 via a continuous scan. An analysis of Figure 4.6 revealed the “calcined” sample was comprised of structural features indicative of a monoclinic structure indexed from PDF-01-070-6831 (van Oversteeg *et al.*, 2020). From these findings it is confirmed that a CuO film was synthesized as no peaks were recorded for other Cu species. No evidence of any peak broadening nor peak shifts were found between the “calcinated” and “etched” samples. In fact, no new peaks appeared at all which suggests the crystallographic structure remained monoclinic even after NH_3 etching. Interestingly, major amplitude decreases were recorded for most FTO peaks. Similarly, the intensity of the CuO peaks remained mostly unchanged up to a scan angle of $2\theta = 50$. Extending the scan angle past this point revealed that the (20-2), (11-3), (22-1), (31-2), (13-2) and (20-4) facet’s intensity decreased by approximately a third though no shift or peak broadening was observed. This decrease in intensity may be associated with thinning of the CuO layer as would be expected via etching and will be further analyzed using SEM.

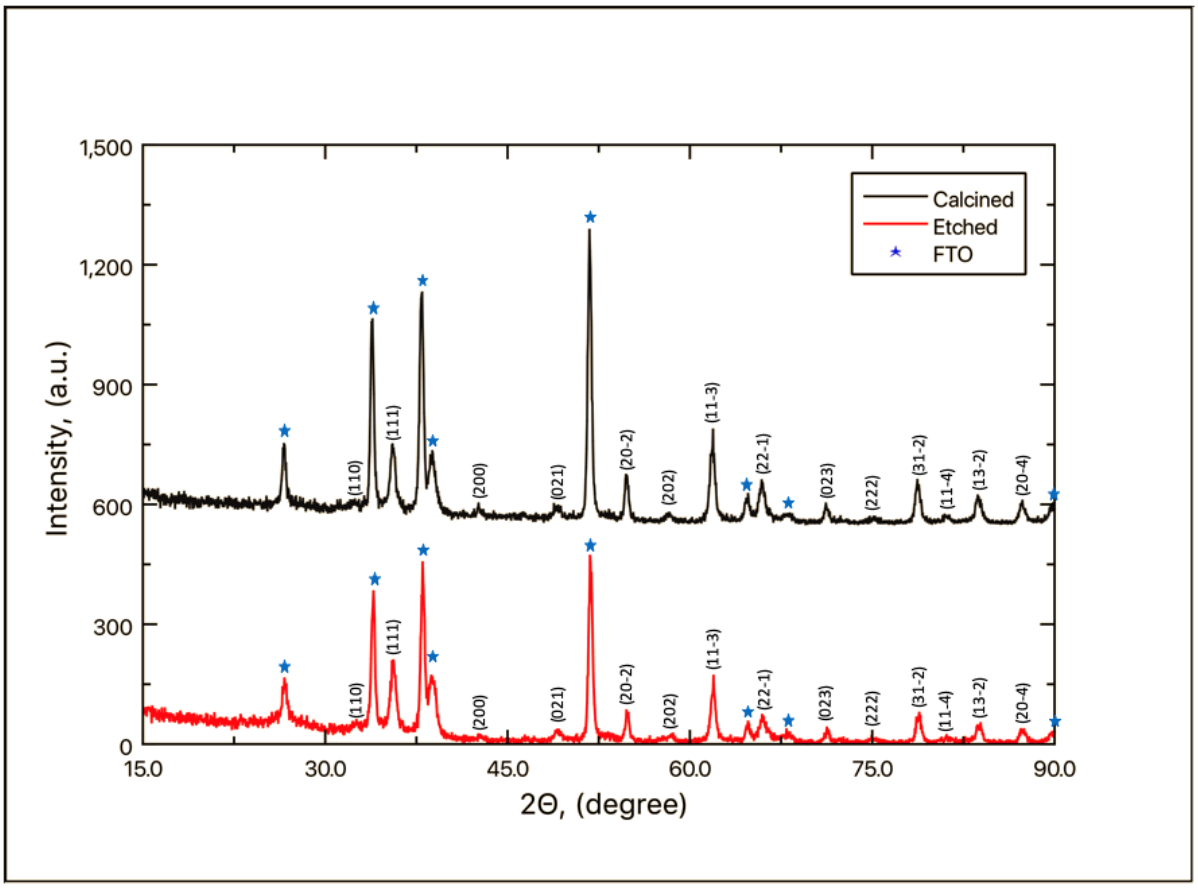

Figure 4.6: XRD patterns for calcined and Etched CuO photoelectrode

4.2.2. X-ray Photoelectron Spectroscopy

X-ray photoelectron spectroscopy experiments were conducted by bombarding selected samples with X-rays of known energy while recording the kinetic energy of the released photoelectrons. From this the binding energy is calculated and used to identify the elements from which the electrons were extracted. All XPS measurements were conducted using a Thermo-ESCAlab 250Xi with a monochromatic Al-$K\alpha$ source (1486.7 eV) and a power of 300 W at an operational pressure of 10^{-8} mBar. Figure 4.7 presents the core Cu 2p, O 1s, C 1s and Sn 3d peaks. The Cu 2p core level's XPS spectra for the "etched" sample featured two peaks corresponding to Cu $2p_{3/2}$ and Cu $2p_{1/2}$ which occurred at 933.4 eV and 953.2 eV respectively. The former binding energy is assigned to Cu^{2+} ions which are characteristic of the CuO phase while the latter further confirms the presence of CuO by matching with the standard XPS spectra for CuO (Li *et al.*, 2015). At least three satellite peaks are recorded at higher binding energy's relative to their main peaks at 940.8 eV, 943.4 eV and 962.0 eV which are assigned to the Cu $3d^9$ configuration. The position of the Cu $2p_{3/2}$ peak with respect to its satellite indicates the existence of two CuO configurations which are the Cu $3d^{10}$ and the Cu $3d^9$ (ground state) (Parmigiani *et al.*, 1992). This further confirms the existence of CuO. The binding energies associated with the O 1s XPS spectra revealed a strong peak at 529.2 eV

which is associated with a metal-oxygen bond in the lattice. A peak at 529.4 eV confirms the M-O bond is in fact a (Cu-O) bond however some impurities were detected in the form of (C-O) bond at 531.0 eV and a (C=O) bond at 532.8 eV. The detection of these impurities is common in samples which have been stored in air as opposed to an evacuated vial. XPS did not detect any form of (-OH) species on the samples surface though the carbon-based impurities were further investigated in the C 1s core level scan. A strong sp^2 (C-C) peak was detected at 284.2 eV along with a secondary confirmation of the contaminant (C-O) and (C=O) species at 285.8 eV and 287.6 eV respectively. Finally, it was confirmed that the FTO glass substrate remained un-altered after etching in NH_3 as Sn^{4+} was detected.

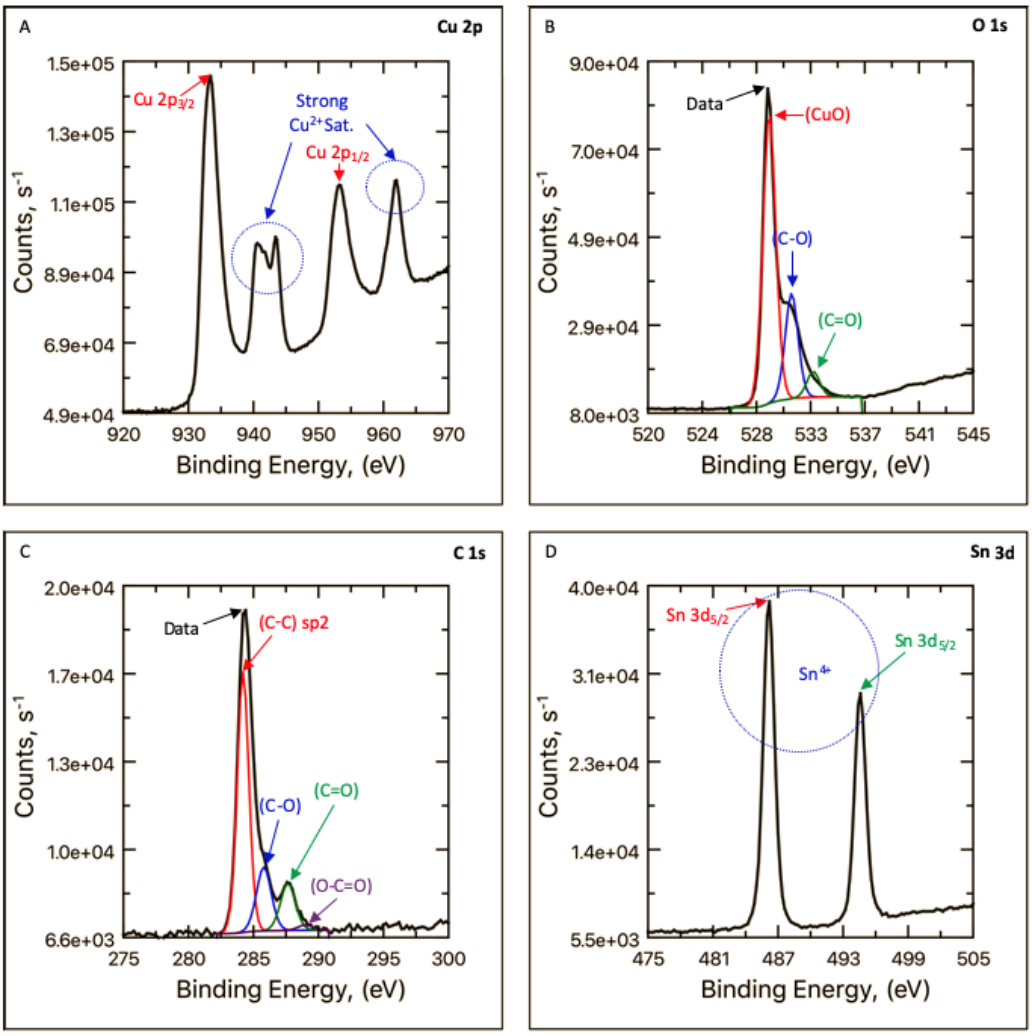

Figure 4.7: XPS spectrographs for the “etched” sample focused on A) Cu 2p-peaks, B) O 1s-peaks, C) C 1s-peaks and D) Sn 3d-peaks

The full XPS survey scan is presented in Figure 4.8 and indicates the presence of other impurities such as Na 1s and N 1s. The presence of these species is as a result of the synthesis processes via the use of Na-compounds in electrodeposition as well as NH_3 during etching. A peak list with the associated binding energy’s and calculated FWHM values is presented in Table 4.1.

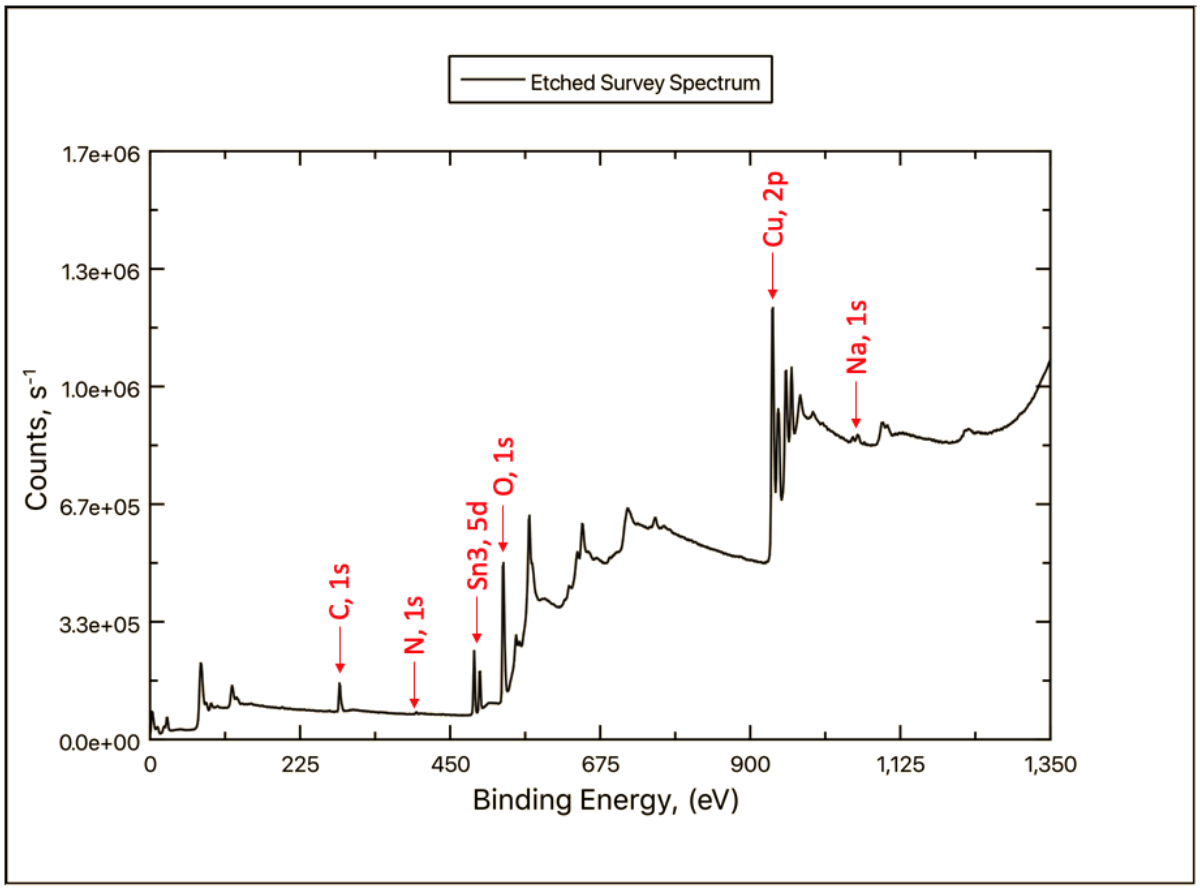

Figure 4.8: Spectrograph showing the full XPS range for the “etched” sample.

Table 4.1: Peak investigation of XPS data for the “etched” sample

Name	Peak BE, eV	FWHM, eV	Area, CPS.eV	Atomic %
O 1s	529.8	3.5	1395763.78	44.9
Cu2p	933.5	3.9	6283549.76	29.9
C 1s	284.4	3.2	278813.67	22.8
Sn 3d	486.1	2.8	787099.27	1.9
N 1s	399.2	2.6	10536.05	0.5

4.2.3. Scanning Electron Microscopy

A Zeiss Auriga field emission scanning electron microscope was employed to evaluate the morphological changes throughout the synthesis process to determine the layer thickness at each stage. All images were compiled using an in-lens electron detector with a beam accelerated to an EHT of 5 kV. SEM images presented in Figure 4.9 show interesting transitions between the different stages of synthesis. The “As deposited” layer (A1-2), featured a random distribution of particles across the substrates surface. Post calcination (B1-2), the particles seem to fuse together in trapezoidal shapes with much more regular grain sizes and crystallinity. By etching the surface of the calcined thin films (C1-2), the trapezoidal nanostructures were reduced in size with seemingly increased porosity. This decrease in film thickness confirms the removal of a small layer of CuO from the surface of the electrode and confirms the reason for the decrease in peak intensity presented on the XRD data. The film

was at its thickest ($\approx 225\ nm$) after calcination and reduced by a 12 % ($\approx 200\ nm$) following etching. The increase in film thickness after calcination may be as a result of Oswald ripening whereby a diffusion process of smaller particles fuse to form bigger ones at elevated temperatures.

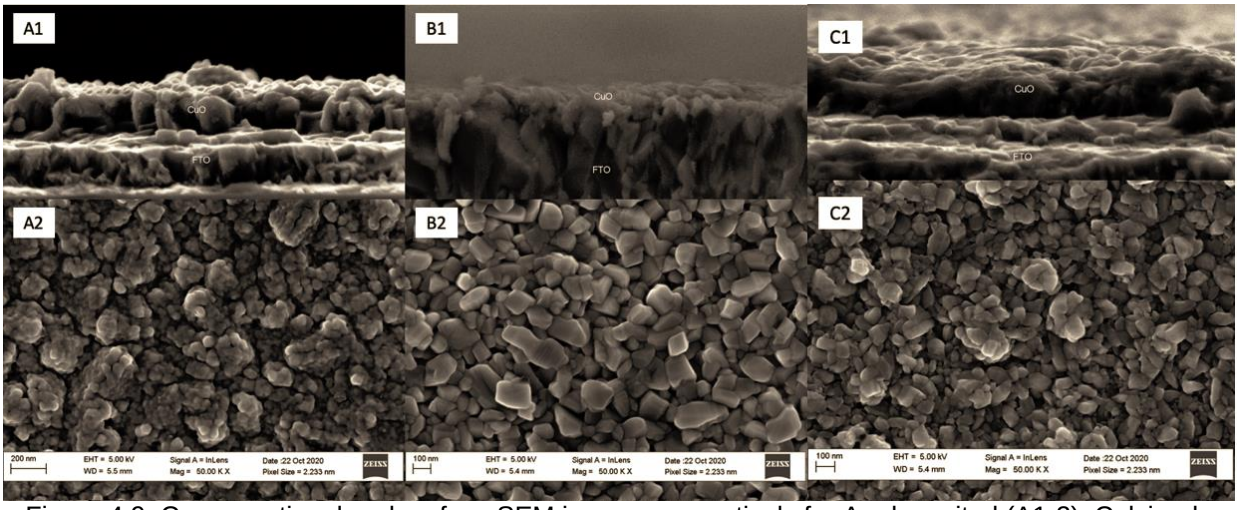

Figure 4.9: Cross sectional and surface SEM images respectively for As-deposited (A1-2), Calcined (B1-2) and Etched (C1-2)

4.2.4. Raman

Raman spectroscopy was employed as a characterization method to identify molecules present in selected samples. Raman spectroscopy revealed three individual peaks which occurred for each sample during the synthesis stages. This alludes to the possibility that the samples in question are composed of the same materials which are unchanged since electrochemical deposition. The peaks presented in Figure 4.10 occur at 280.6, 323.3 and 613.4 cm^{-1} respectively. The primitive cell of CuO contains two molecules such that there exists nine optical zone-centered modes which are $A_g + 4A_u + 2B_g + 5B_u$ (Debbichi *et al.*, 2012). Of these, only three modes are Raman active ($A_g + 2B_g$). Upon comparison with other works, the 280.6 cm^{-1} peak can be assigned to the A_g whilst the 323.3 cm^{-1} and 613.4 cm^{-1} are B_g modes (Nagajyothi, 2015).

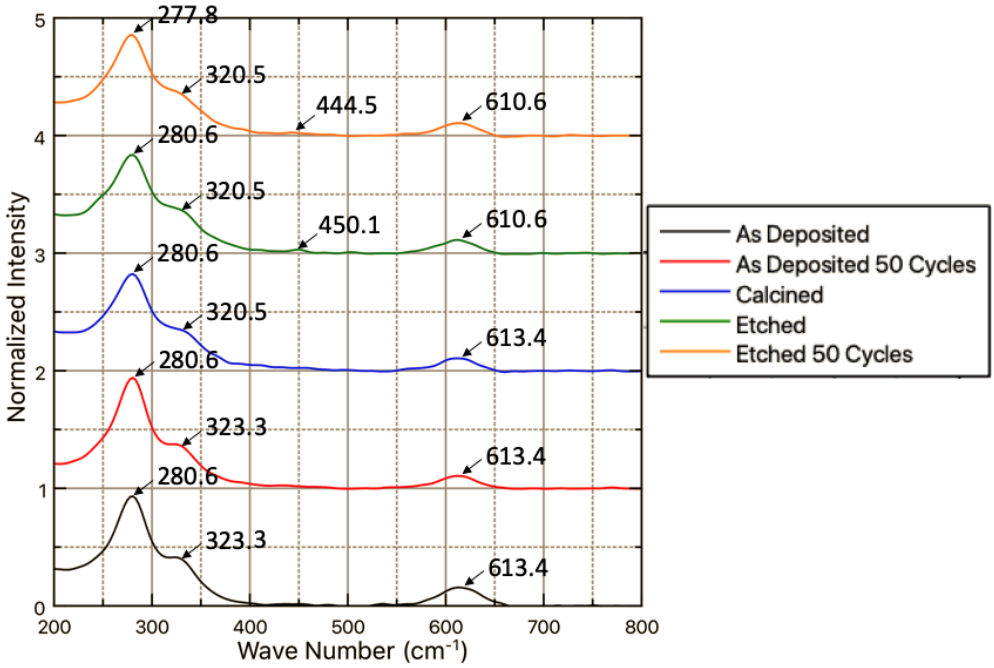

Figure 4.10: Raman spectra for the various stages of synthesis including tested samples.

The intensity of the peaks have been normalized however, it can be noted that the intensity of the "as deposited" sample after 50-cycles is much sharper as compared to the others. It has been reported that intensity is related to grain size and that Raman peaks are observed to shift with grain size variations (Joya, Barba-Ortega and Raba, 2019). This along with SEM images showing what appeared to be increased porosity; the small deviations noted among the wave numbers are attributed to the grain size differences. Raman can also be used to identify the presence of unintended species such as Cu_2O or even $Cu(OH)_2$ (Tran and Nguyen, 2014). Glucose has been reported to reduce copper hydroxides to form cuprous oxide according to the equation below (Su, 2018), however the Raman data obtained for samples following glucose testing shows no Cu_2O in any of the films.

$$Cu(OH)_2 + C_6H_{12}O_6 \rightarrow Cu_2O + H_2O$$

New minor peaks appear following etching at 450.1 cm^{-1} and 444.5 cm^{-1} respectively. Following thermal oxidation, the 323.3 cm^{-1} peak undergoes a blue shift to 320.5 cm^{-1} which may be as a result of the increased presence of oxygen in the crystal structure as seen in the XPS data. Then after etching the 613.4 peak shifts to 610.6 cm^{-1} and is ascribed to the decrease in crystallinity in the A_g mode.

4.2.5. Hall Effect

To better understand the electronic transport nature of the deposited semiconductor, Hall Effect measurements were carried out to identify the type of charge carrier, the carrier

concentration, Hall mobility as well as conductivity of the samples. The Hall measurements were conducted at 300K, 500 μA and 0.55 T using an Ecopia HMS-3000 measuring system. These parameters are displayed in Table 4.2 for the "As-deposited", "Calcined" and "Etched" samples including tests conducted after 50 CV cycles. The thickness of the films was obtained from SEM images in the previous section and reported alongside the hall measurements.

Table 4.2: Characteristic values determined through Hall Effect measurements

Parameter	As Deposited	As deposited 50 Cycles	Calcined	Etched	Etched 50 cycles
Layer Thickness (μm)	0.200	0.200	0.225	0.200	0.200
Bulk Concentration (/cm^3)	-1.34E+22	-2.36E+22	-1.27E+21	-8.85E+20	-1.15E+21
Sheet Concentration (/cm^2)	-4.05E+17	-4.71E+17	-2.60E+16	-2.67E+16	-2.90E+16
Mobility (cm^2/Vs)	7.91	7.36	2.54E+1	1.23E+1	2.68E+1
Resistivity (Ωcm)	5.89E-5	3.60E-5	1.94E-4	5.73E-4	2.03E-4
Conductivity (1/Ω cm)	1.70E+4	2.78E+4	5.15E+3	1.75E+3	4.94E+3
Average Hall Coefficient (m^2/C)	-4.70E-4	-2.65E-4	-4.92E-3	-7.05E-3	-5.43E+3
Transfer Type	n-type	n-type	n-type	n-type	n-type

Typically, metal-oxide based sensors will follow one of two different sensing mechanisms depending on the majority charge carriers present. Sensors which display p-type characteristics will adsorb oxygen to form acceptor levels near the valence band which results in upward band bending. As a result, an accumulation layer of holes is formed near the surface which has been reported to enhance hole transport (Barsan *et al.*, 2010). From the hall coefficients it can be deduced that throughout the synthesis and testing process, the CuO film is classified as an n-type semiconductor. This is due to the negative values of the hall coefficients which decrease through the stages of fabrication. In addition, this finding reveals that the majority charge carriers are electrons. This means that although no doping occurred in these samples, there exists a donor state close to the conduction band which can accept

free electrons within the band gap. The electron-hole generation and trapping in this n-type semiconductor are further discussed in the transient photocurrent section. The Van der Pauw method was applied in an iterative process to determine the charge carrier mobility and sheet concentration. The carrier mobility tripled (7.91 → 25.4 cm^2/Vs) following the calcination step which is as a result of the increased crystallinity and uniform morphology along with the increase in layer thickness seen in the SEM images. Additionally, the grain sizes were larger in the calcined sample and are inclination free which could result in a more direct flow path. A decrease in mobility was found following the etching stage as a result of the decreased particle sizes, uniformity and layer thickness. The etched samples mobility (12.3 cm^2/Vs) however is still almost double that of the original as deposited sample (7.91 cm^2/Vs).

It was found that a three-fold increase in resistivity (5.89E-5→1.94E-4 Ωcm) yielded an approximately equivalent threefold increase in carrier mobility. Wu et al. noted that high resistivity's (better insulators) are associated with low carrier mobility's but are greatly influenced by temperature which could be the cause of the deviations seen in this data (Wu *et al.*, 2014). The calculated resistivities in this work are very low and more comparable with bulk Cu. Nevertheless, there are reports where the resistivity's of CuO-based nanomaterials fall between 2.0E-5 to 1.0E+6 Ωcm (Li *et al.*, 2010; Yabuki and Arriffin, 2010; Grigore *et al.*, 2016). During electrodeposition, the formation of electrically active vacancies could be replaced by neutral CuO sites which could lead to decreased resistivity's and so upon calcination are increased by the generation of carriers in the crystalline structure (De Los Santos Valladares *et al.*, 2012). Low range resistivities especially for semiconductors are highly sought after as it shows better conductivity which translates to increased mobility.

With the characteristic resistances across the sheet the overall sheet resistance was found for each sample. Interestingly, the bulk carrier concentration (-8.85E+20 cm^{-3}) was the largest in the etched sample which could explain why relatively high mobility's were recorded for this sample. Other authors have noted carrier concentrations of 4.0E+18, 9.0E+19 and 6E+20 cm^{-3}, of which some are several orders of magnitude smaller than in those reported in this work (Li *et al.*, 2010; Wu *et al.*, 2014; Morasch *et al.*, 2016). Such high charge carrier concentrations could be an indication of low valence band maximums which cause fermi-level pinning (Parenr *et al.*, 1980). Li et al. investigated the relationship between carrier concentration and mobility while comparing the effects to sensing performance. They found that decreased carrier concentrations and increased carrier mobility's resulted in higher sensitivity (Li *et al.*, 2019).

4.2.6. UV-Vis Spectra

The UV-Vis diffuse reflectance spectra of the “As-deposited”, “Calcined” and “etched” CuO samples were assessed to determine the light absorption properties of these films. The spectra was run from a wavelength of 200 nm to 2500 nm while recording the reflectance R (%). The optical band gap of semiconductors can be evaluated using the theory from Kubelka and Munk (Kubelka, 1954). Because the Tauc method assumes the absorption coefficient (K) is energy dependent, it may be replaced with a ratio of (K) and the scattering coefficient (S). Figure 4.11-A shows the reflectance spectra for the three samples and while Figure 4.11-B reveals the absorption (K) and scattering coefficients (S) in relation to the photon energy. From the reflectance spectra, the ratio (K/S) was determined by applying the following relationship.

$$F(R_\infty) = \frac{K}{S} = \frac{(1 - R_\infty)^2}{2R_\infty}$$

Where $R_\infty = \left(\frac{R_{Sample}}{R_{Stardard}}\right)$ represents the reflectance of a sample with infinite thickness, K denotes the absorption coefficient whilst S is the scattering coefficient. Upon substitution of this ratio into the Tauc relation, the following equation is obtained.

$$\left(\frac{K}{S}(h\upsilon)\right)^n = B(h\upsilon - E_g)$$

Here, h is planks constant, υ is the photon energy, B is a constant and E_g is the band gap. The n power is especially important as this defines the nature of the electron transition which is associated with direct or indirect bands. When $n = 2$, a “direct allowed” band structure is present and if $n = 0.5$, and “indirect allowed” band structure prevails. However, n can also be 2/3 in which case the transition is “direct forbidden” and also 1/3 for “indirect forbidden”.

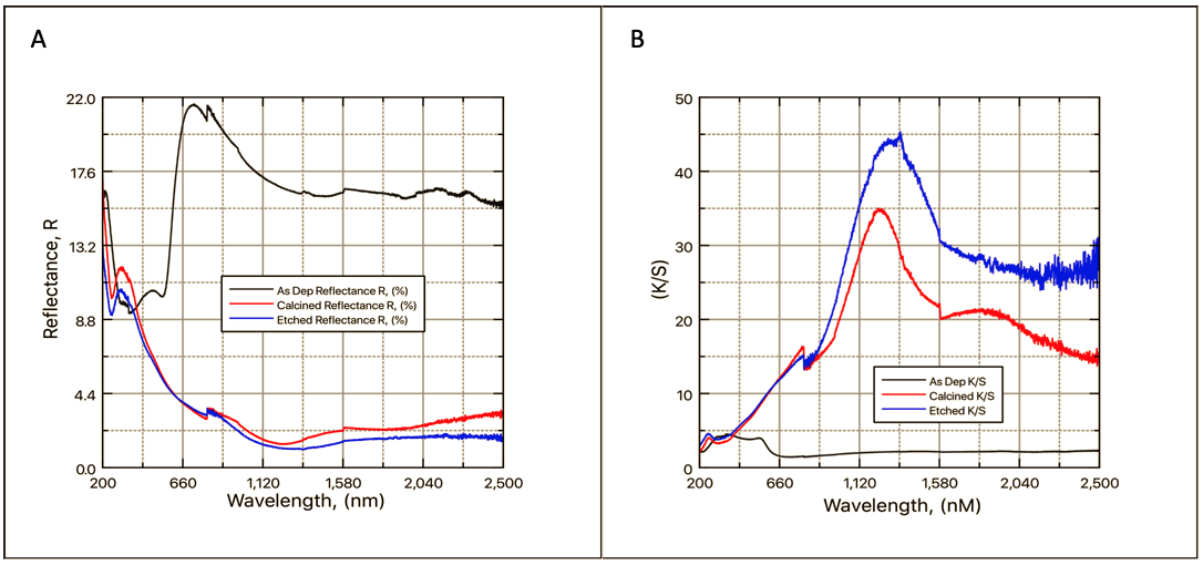

Figure 4.11: UV-Vis diffuse reflectance spectra for As-deposited, Calcined and etched samples with A) Reflectance R (%) and B) Absorption/Scattering (K/S) coefficients as determined through reflectance spectra

The band gaps for the samples were determined using the x-axis "$h\upsilon$" intercepts of the plots in Figure 4.12. It was found that as the synthesis process proceeded, the optical band gap decreased accordingly; As-Deposited > Calcined > Etched. An E_g of 1.88 eV was found for the etched sample, 2.07 eV for the calcined sample and two band gaps were discovered for the As-Deposited sample at 2.01 eV and 2.18 eV. The band gap for CuO have been reported to fall over a range between 1.2 eV and 2.1 eV which is in good agreement for all samples tested. It is apparent that the morphology and layer thickness greatly impact the optical properties and by extension the band gap. Interestingly, upon thermal oxidation the band transitions from a "direct allowed" to a "direct forbidden". Direct band structures are indicative of crystalline semiconductor materials.

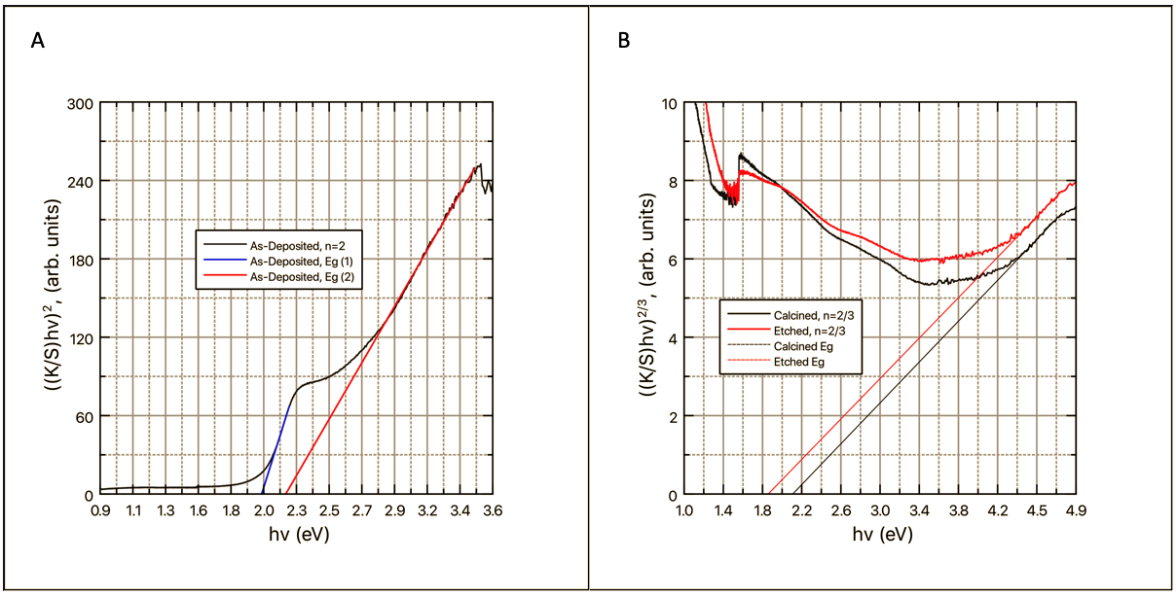

Figure 4.12: Band gap determination of A) "As-deposited" at n=2 and B) "Calcined and Etched" at n=2/3

4.3. Photo-Electrochemical Characterization

4.3.1. Cyclic Voltammetry

The electrochemical characterization of the deposited CuO film was evaluated using cyclic voltammetry (CV) in an alkaline medium (0.1 M NaOH) both in the presence and absence of glucose. The electrochemical activity towards the oxidation of glucose was measured in a 1 mM solution of Glucose. A total of 10 stabilization cycles were performed before the data was recorded to ensure stability. The CV's conducted in the dark were performed in an optical glass box housed in cardboard to block illumination of the sample from ambient light. The same cardboard housing was used for samples undergoing illumination via a cool white LED (6 W, 540 lumen) through a cut out in the box.

a) Optimized Synthesis Parameters Electrochemical Behavior

Using the optimized synthesis parameters (4 V for 2 min electro-deposition, 450 ℃ calcination for 1 h and 2 min of NH_3 etching) the resultant current densities are represented in Figure 4.13. It can be seen that the current density of the as-deposited CuO film is the greatest at 1.87 mA/cm^2 in the dark. In the light however a very small increase of 0.175 mA/cm^2 is noticed. The optimization process focused on the maximization of photocurrent and so as this sample produces the smallest difference between dark and light, its photoactivity is inferior as compared to the calcined and etched samples. This may be as a result of the increased band gap (2.01-2.18 eV) found for the as deposited sample. Nevertheless, current density produced by this sample in the presence of 1 mM glucose is impressive as it enjoys higher current densities in both light and dark scenarios. As seen from the SEM images this sample is also the most porous of all the samples which might explain the aforementioned phenomena. The increase in current density for the calcined samples was found to be 0.261 mA/cm^2 whilst the greatest difference was recorded for the etched sample with an increase of 0.328 mA/cm^2 from dark to light. A possible reason for this increase in photocurrent could again be attributed to the decrease in band gap from calcined (2.07 eV) to etched sample (1.9 eV). A smaller band gap in a semiconductor translates to less energy being required to promote an electron from the valence band into the conduction band.

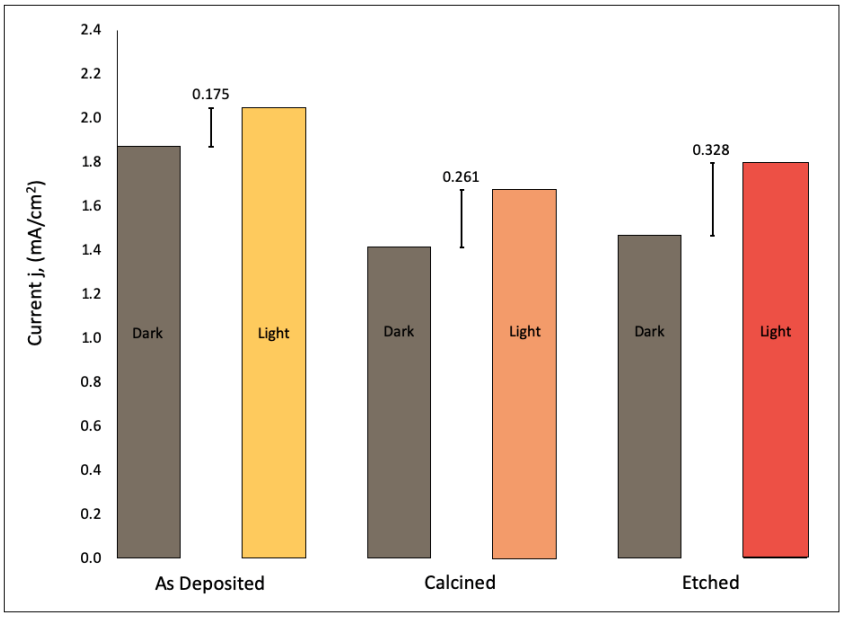

Figure 4.13: Peak current densities recorded for the As-Deposited, Calcined and Etched samples at 100 mV/s in 1 mM Glucose.

b) Electrochemical behavior via CV

The oxidation of carbohydrate species on Cu-based electrodes occurs over a similar potential range to that of the Cu(III) species formation. The redox couple between Cu(II)/Cu(III) is reported to occur at potentials 0.58 and 0.61 V vs Ag/AgCl in 0.1 M NaOH (Pap and Szyrwiel, 2017). Non-enzymatic glucose electrooxidation is believed to be mediated by this redox couple as CV measurements indicate oxidation over this wide potential range. The formation of the Cu_2O_3 species has also been reported, however under the same alkaline conditions (0.1 M NaOH) its formation occurs at higher potentials than oxygen evolution (Xia *et al.*, 2015). Similarly, the formation of highly reactive hydroxide radicals has been proposed to act as the mediators in glucose oxidation. The standard potential for this redox pair (E > 1.33 V) is however well outside the potential window tested (Xie and Huber, 2001). It is for this reason that the glucose oxidation mechanism most often considered by other researchers involves the formation of highly oxidative Cu^{3+} species. This demands the formation of individual or a combination of Cu^{3+}, CuO_2^-, Cu_2O_3, CuOOH, $Cu(OH)_3$ or $Cu(OH)_4$ species for the process to proceed (Xia *et al.*, 2015; Inyang *et al.*, 2020). The reactions associated with Cu(II)/Cu(III) redox pair are summarized in Equations 2-4 and glucose is oxidized as per Equation 5 to form gluconic acid after hydrolysis of gluconolactone:

$$CuO + OH^- + H_2O \rightarrow Cu(OH)_3 + e^- \qquad \text{Eq 2}$$

$$CuO + 2OH^- + H_2O \rightarrow Cu(OH)_4^- + e^- \qquad \text{Eq 3}$$

$$CuO + OH^- \rightarrow CuOOH + e^- \quad \text{Eq 4}$$

$$Cu^{3+} + Glucose \rightarrow Cu^{2+} + Gluconolactone \quad \text{Eq 5}$$

Jose' et al determined that while the CuOOH species is most commonly used to describe the glucose oxidation mechanism via Cu^{3+}, no equilibrium potential nor CV peaks are obtained for its reaction (Barragan *et al.*, 2018). Although it is well known that CuO exhibits semiconductive behavior, few works make use of this property and so information regarding the photo-electrochemical oxidation of glucose is scarce. These photoelectro-oxidative properties of CuO were investigated under cool white LED illumination (6 W, 540 lumen) in a blank 0.1 M solution of NaOH and 1 mM glucose solution. As per the CV's in Figure 4.14-A, in the absence of glucose at 100 mVs^{-1} scan rate, there are no observable redox peaks for both bare FTO nor for the etched CuO electrode. A prominent current plateau is evident in both cases with an exponential anodic current increase at potentials greater than 0.65 V for this CuO electrode. This rapid current rise can be attributed to the formation of oxygen on the surface of the electrodes following the oxidation of OH^- ions (Lide, 2005; Wang *et al.*, 2010; Barragan *et al.*, 2018).

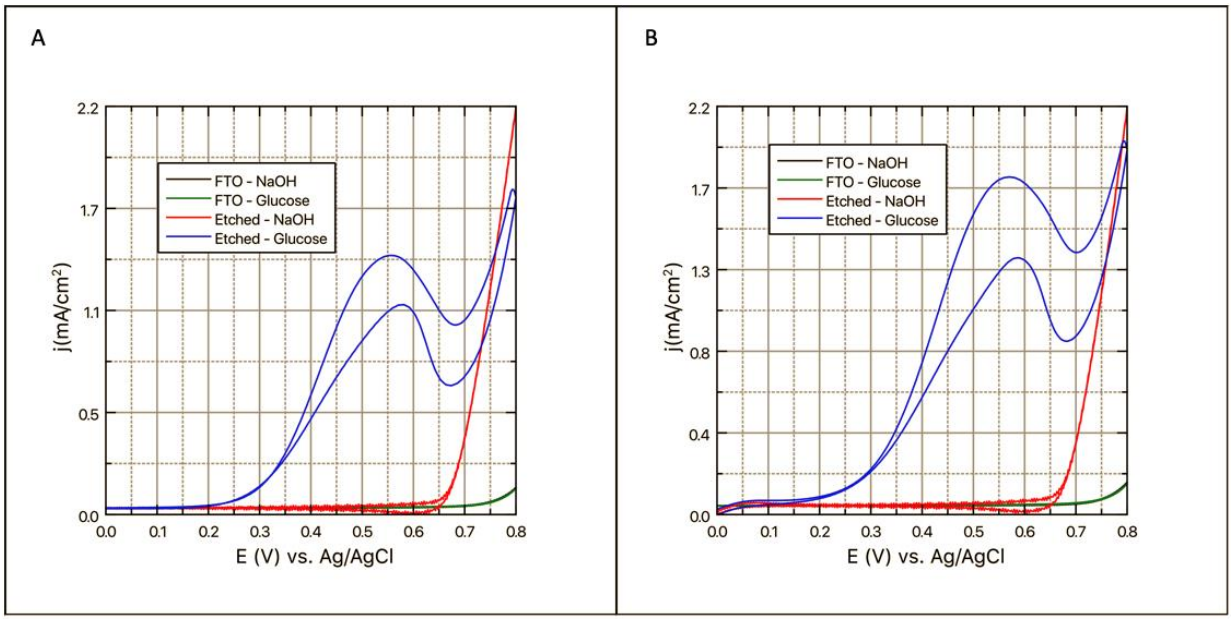

Figure 4.14: Electrochemical behavior at 100 mVs^{-1} scan rate for the fabricated CuO electrode in a blank NaOH and 1 mM glucose solution under A) Dark and B) Light conditions

The separation observed between the forward and reverse scan of the etched sample in 0.1M NaOH could be attributed to the chemical reaction Eq. 1.1-1.2 (Felix *et al.*, 2017).

$$Cu(OH)_2 + OH^- \rightarrow CuOOH + H_2O + e^- \quad \text{Eq. 1.1}$$

$$CuO + OH^- \rightarrow CuOOH^- + e^- \quad \text{Eq. 1.2}$$

The shape of the CV curve presented in Figure 4.14 changes dramatically with clear oxidation-reduction peaks evident in the presence of glucose in the dark and light. This isolates the electrocatalytic activity toward glucose as being solely due to the copper species deposited on the substrate and not the FTO. Figure 4.14-A features an oxidation peak at 0.56 V vs Ag/AgCl accompanied by an anodic current density of 1.41 mA/cm^2 with a reduction peak occurring at 0.67 V vs Ag/AgCl and 0.69 mA/cm^2. These peaks occur well above the current plateau observed in the blank solution.

Figure 4.14-B shows CV-curves which illustrate just how much light enhances the oxidation process by simply making use of its built-in semiconductive properties. The etched CuO electrode presents anodic photocurrents in the presence of glucose in the dark and light scenario at onset potentials of 0.27 V and 0.15 V respectively. A decrease in onset potential has previously been reported, however, it is very unique for Cu based electrodes (Billy and Co, 2018). A peak current density of 1.795 mA/cm^2 was observed while illuminated, which, equates to an increase of 0.382 mA/cm^2, far greater than in the dark. Although the general CV shape appears consistent, upon closer examination is was found that under illumination, the oxidation potential increased by 0.014 V thus requiring an applied potential 0.576 V. This small potential change is attested to a shift in the equilibrium position of the system to less andic values. Due to the semiconductive nature of CuO and the subsequent increase in current density as seen in the CV's in the light, it is required to investigate alternate mechanisms which could be the reason for this increase. An overall depiction of the possible reaction pathways for the oxidation of glucose in both the light and dark is represented in Figure 4.15. Both reaction pathways 1 and 2 have been well documented for group (III) M-O for glucose oxidation in the dark (Barragan *et al.*, 2018; Billy and Co, 2018; Mensah *et al.*, 2018; Giziński *et al.*, 2020).

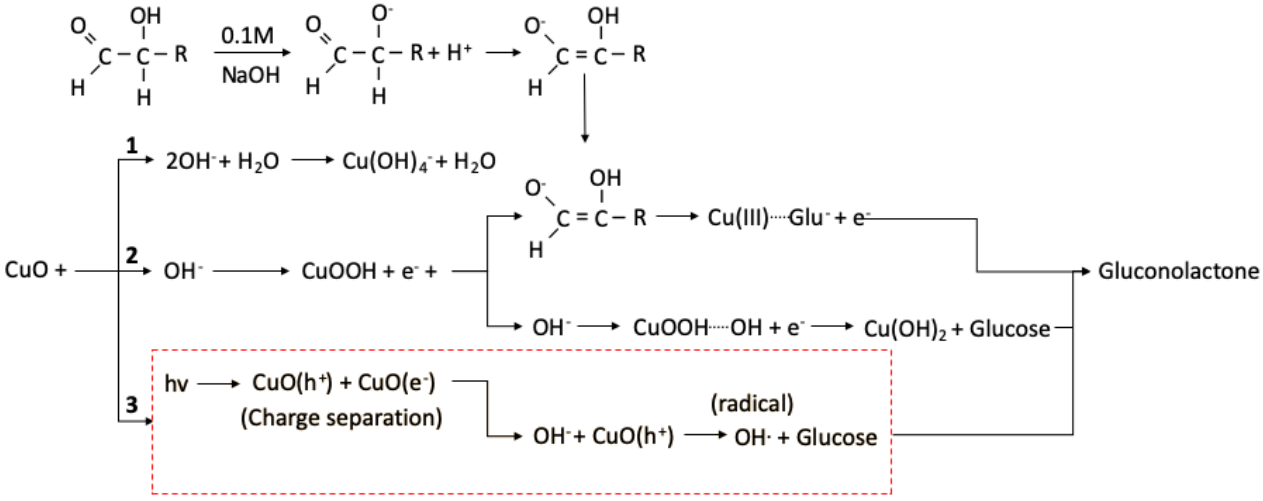

Figure 4.15: Glucose oxidation pathways

The etched CuO film was excited by the light incident on its surface resulting in the generation of e^- and h^+ which undergo charge separation as depicted in pathway 3. The CB energy level for FTO is lower than that of CuO which results in electron transfer from CuO to FTO as this is the more energetically favorable process (Hirst *et al.*, 2019). Good contact between the FTO and CuO as a result of the high calcination temperature provided the ideal electron transport system which translated into high light sensitivity and aided in reducing electron hole pair recombination. The $CuO(h^+)$ left behind in the VB pair with OH^- ions which are oxidized to form hydroxyl radicals under the assumption that charge transfer occurs efficiently (Barragan *et al.*, 2018). These radicals desorb from the CuO surface and so leave behind an active site for more hydroxyl ions to adsorb to (Ahn and Bard, 2016). Glucose molecules are then attacked by the radicals as depicted in Figure 4.16. The radicals react with D-Glucose by means of hydrogen abstraction that forms an intermediate glucose species with a carbon centered radical. This is followed by oxygenation of the subsequent intermediate by releasing a carbonyl group which forms gluconolactone (Travaini *et al.*, 2015). Hydration of the gluconolactone species results in the reversible gluconic-acid/gluconolactone system.

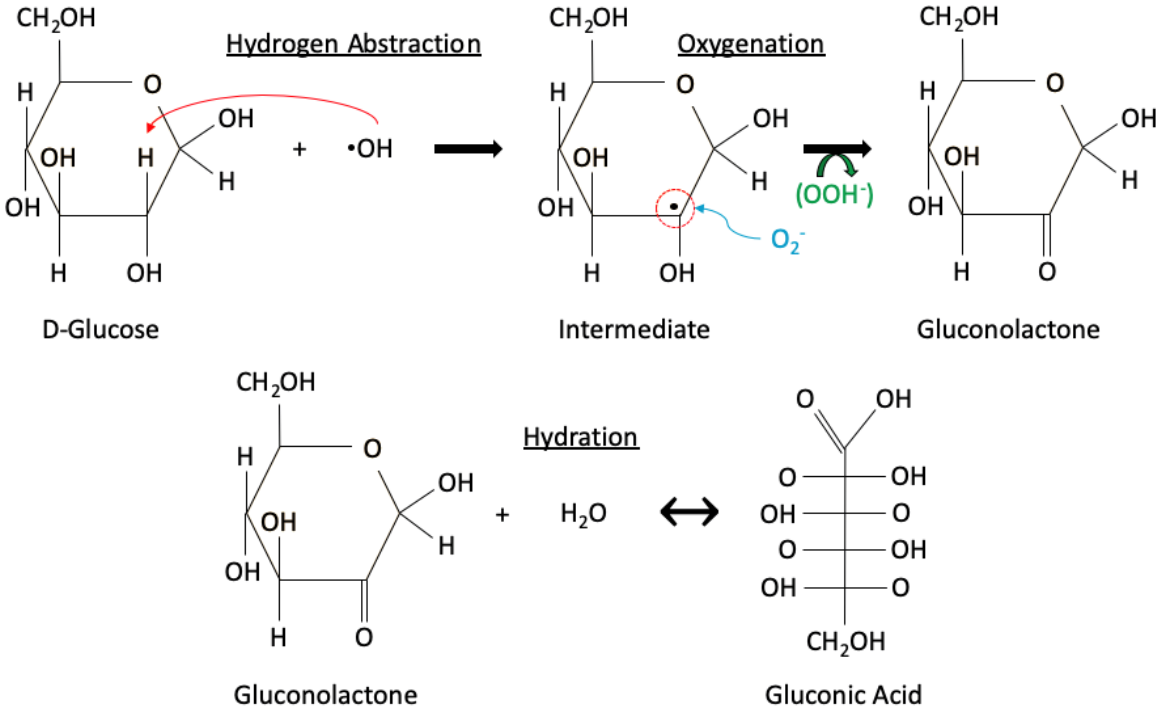

Figure 4.16: Glucose oxidation via hydroxyl radical attack ultimately forming of gluconic acid.

The glucose sensing mechanism proposed to take place in light via pathway 3 aligns well with other reports of carbohydrate oxidation through hydroxyl radical attacks (Travaini *et al.*, 2015; Barragan *et al.*, 2018). Herein lies a problem as sensors making use of this mechanism could suffer from low selectivity. This issue of selectivity will be further addressed in the chronoamperometric analysis.

The formation of hydroxyl radicals via surface adsorbed OH^- have been extensively studied (Shibata *et al.*, 1998; Liao and Reitberger, 2013; Nosaka and Nosaka, 2016). The reduction potential of surface bound OH radicals is far less than the $OH^-/\cdot OH$ redox couple thus providing additional evidence for the mechanism proposed in Figure 4.16. In both the light and dark conditions, the shape of the CV curves remained the same though the peak currents differed. It is then entirely plausible that with the inclusion of light, there is additional generation of oxidative $\cdot OH$ species over and above the oxidation occurring via the Cu(II)/Cu(III) couple. This would explain the increase in current density seen in the light as more electrons would be excited into the conduction band of the CuO photoelectrode thus increasing the conductivity as depicted in Figure 4.17.

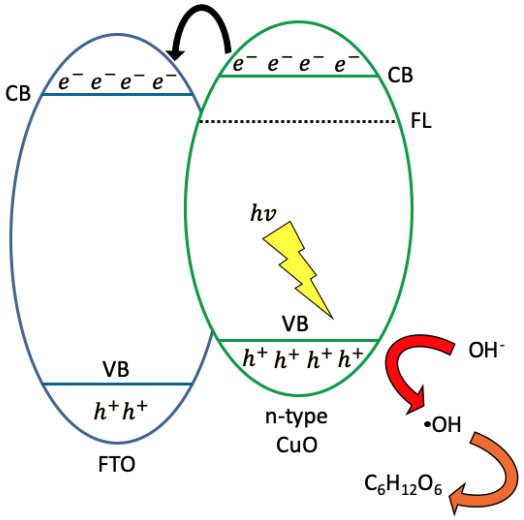

Figure 4.17: Energy diagram illustrating the coupling between CuO and the FTO substrate

c) Electrochemical Kinetics

The kinetic interactions occurring at the electrode's interface offer a clearer view to draw meaningful conclusions regarding the glucose oxidation process. In the interest of conciseness, the photoelectrochemical results for the as-deposited and calcined sample have been omitted from this section and included in the appendix. The kinetic interactions were investigated using CV measurements over a range of scan rates (25, 30, 40, 50, 70, 100, 150, 175, 200 and 300 mV/s) in a solution containing 1 mM glucose and 0.1 M NaOH. Figure 4.18 reveals how the oxidation potential and ultimately peak current varies with scan rate.

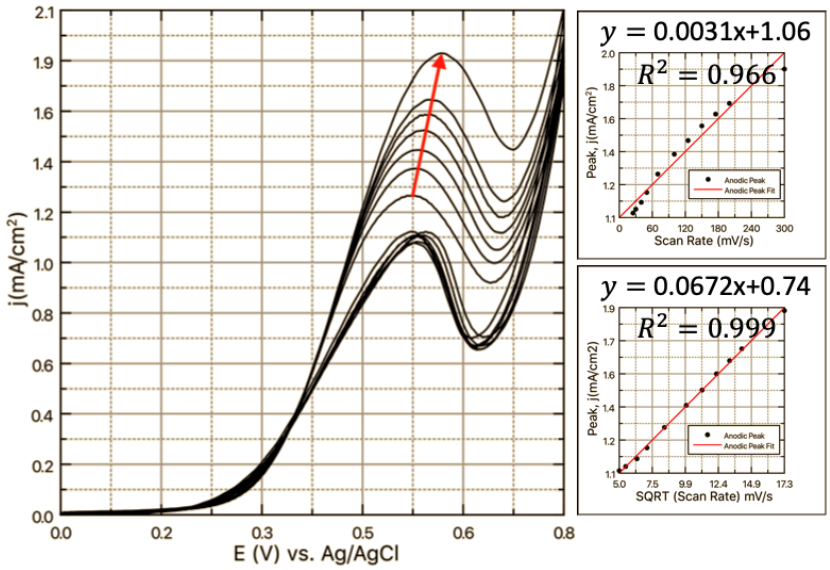

Figure 4.18: CV cycles in 1 mM Glucose in the dark over a range of scan rates with peak anodic currents against scan rate and square root of scan rate and their linearity's

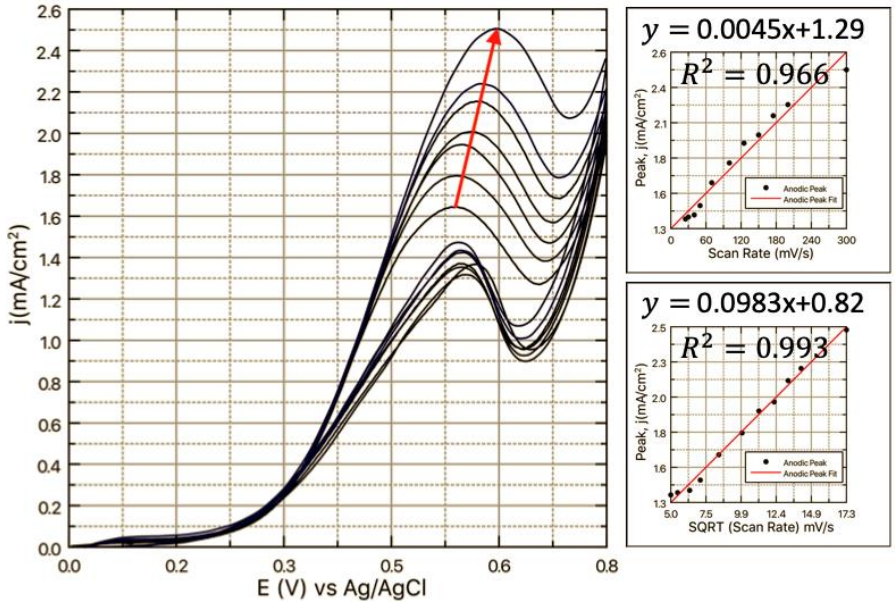

Figure 4.19: CV cycles in 1 mM Glucose in the light over a range of scan rates with peak anodic currents against scan rate and square root of scan rate and their linearity's

A shift in potential to more positive oxidative levels is observed with increasing scan rate suggesting that the glucose oxidation process is irreversible whilst the Cu(II)/Cu(III) redox couple is electrochemically reversible. A plot (Figure 4.20) of peak potential vs log(υ) revealed a slope of 57.5 mV/decade further supporting the theory that an irreversible electron transfer process is the reason for the oxidation peaks during the anodic scan. Also, no reduction peaks are formed at potentials lower than the oxidation potential (0.6 V vs. Ag/AgCl) solidifying the irreversible nature. A strong linear dependence exists between $i_p \; and \; \sqrt{v}$ with a regression coefficient of R^2 = 0.999 in the dark (Figure 4.18).

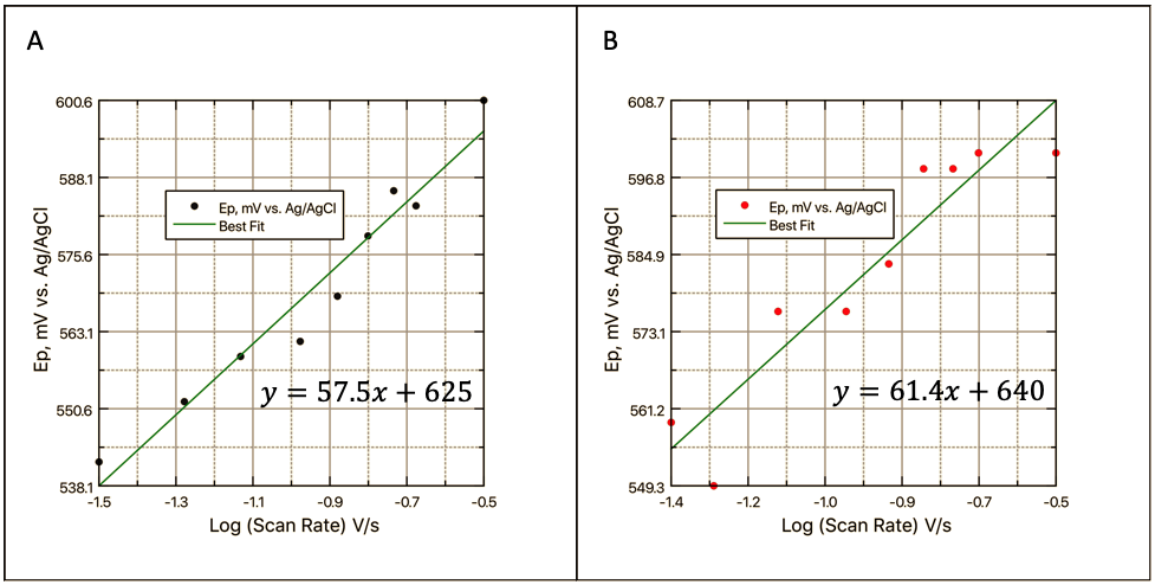

Figure 4.20: Peak potential vs. log(υ) in the A) Dark and B) light

Similarly, a strong linear relationship was found between $i_p \; and \; \sqrt{v}$ which retains a regression coefficient of R^2 = 0.993 in the light (Figure 4.19). A slope of 61.4mV/decade was found in the light for the etched CuO sample as depicted in Figure 4.20. These dependencies in both the light and dark indicate that the oxidation of glucose at this CuO electrode is a mass transfer process within the double layer controlled by diffusion of glucose to the active redox sites. Also, these findings rule out the possibility of a quasi-reversible system as in such processes, linearity between $i_p \; and \; \sqrt{v}$ is not found. Anodic shifts were also noted to increased potentials with increasing scan rate in the light. The difference however is the magnitude of anodic current which is far greater than in the dark with all others equal. Interestingly, the cathodic scan also reveals little change in peak potentials however these were more easily distinguishable. This may be due to a difference in the kinetic rate constant. The electrochemical rate constants (k_o) for this system could not be assessed via CV experiments due to the fact that the formal potential (E^0) for this glucose/CuO system is not obtainable (Bard and Faulkner, 2000). Alternatively, the rate constants can be predicted by making use of EIS data which is further discussed in the EIS-section.

Interestingly upon increasing the scan rate, there was little to no change in the cathodic sweeps. In-fact at lower scan rates (not shown) these cathodic scans were indistinguishable. Here, the rate constant for electron transfer is so fast that diffusion is the only limiting factor towards overall peak potential. For each of the scan rates in the light and dark conditions, the peak oxidation potentials (E_p) were assessed along with the half peak potentials ($E_{p/2}$) and are recorded in Table 4.3 and 4.4. For an irreversible mass transport-controlled system the diffusion coefficient was assessed using the following equations where the electrochemical transfer coefficient must first be calculated.

$$\left(E_p - E_{p/2}\right) = \frac{1.857RT}{\alpha F}$$

$$D_o = \left(\frac{i_p}{(2.99 \times 10^5)\alpha^{0.5} A C_o D_o^{0.5} \upsilon^{0.5}}\right)^2$$

Table 4.3: Important electrochemical parameters deduced at various scan rates in the dark

Scan Rate, υ in mV/s	i_p, in mA	E_p, in V	$E_{p/2}$, in V	α	D_o
25	1.086	0.554	0.396	0.301	7.02E-05
30	1.108	0.542	0.398	0.331	4.60E-05
40	1.146	0.579	0.400	0.268	3.43E-05
50	1.201	0.552	0.403	0.320	2.01E-05
70	1.303	0.559	0.410	0.320	1.21E-05
100	1.413	0.562	0.415	0.326	6.86E-06
125	1.489	0.569	0.420	0.320	4.96E-06
150	1.571	0.579	0.425	0.310	3.95E-06
175	1.636	0.586	0.430	0.305	3.20E-06
200	1.696	0.583	0.432	0.315	2.55E-06
300	1.885	0.601	0.442	0.301	1.47E-06

Table 4.4: Important electrochemical parameters deduced at various scan rates in the Light

Scan Rate, υ in mV/s	i_p, in mA	E_p, in V	$E_{p/2}$, in V	α	D_o
25	1.367	0.601	0.403	0.241	1.39E-04
30	1.383	0.579	0.400	0.268	8.88E-05
40	1.399	0.559	0.398	0.296	4.62E-05
50	1.469	0.549	0.403	0.326	2.97E-05
70	1.644	0.576	0.410	0.287	2.15E-05
100	1.795	0.576	0.420	0.305	1.18E-05
125	1.946	0.583	0.427	0.305	8.88E-06
150	2.008	0.598	0.432	0.287	6.98E-06
175	2.151	0.598	0.437	0.296	5.71E-06
200	2.228	0.601	0.442	0.301	4.62E-06
300	2.439	0.601	0.449	0.315	2.35E-06

From the CV's conducted at various scan rates the mean diffusion coefficients in the light and dark were 1.8×10^{-5} cm²/s and 3.3×10^{-5} cm²/s respectively. These values are in good agreement with literature (Sattarahmady and Heli, 2012; Haynes, 2016; Raziq *et al.*, 2017). An increase in the mean diffusion coefficient was noted in transitioning from the dark to light condition. This is ascribed to the presence of additional charge carriers (e^-/h^+) present at the

electrodes surface which assist in the glucose oxidation process. In both the light and dark, the diffusion coefficient decreased exponentially with increasing scan rate as depicted in Figure 4.21. This decrease is as a result of the depletion of the diffusion layer at higher scan rates.

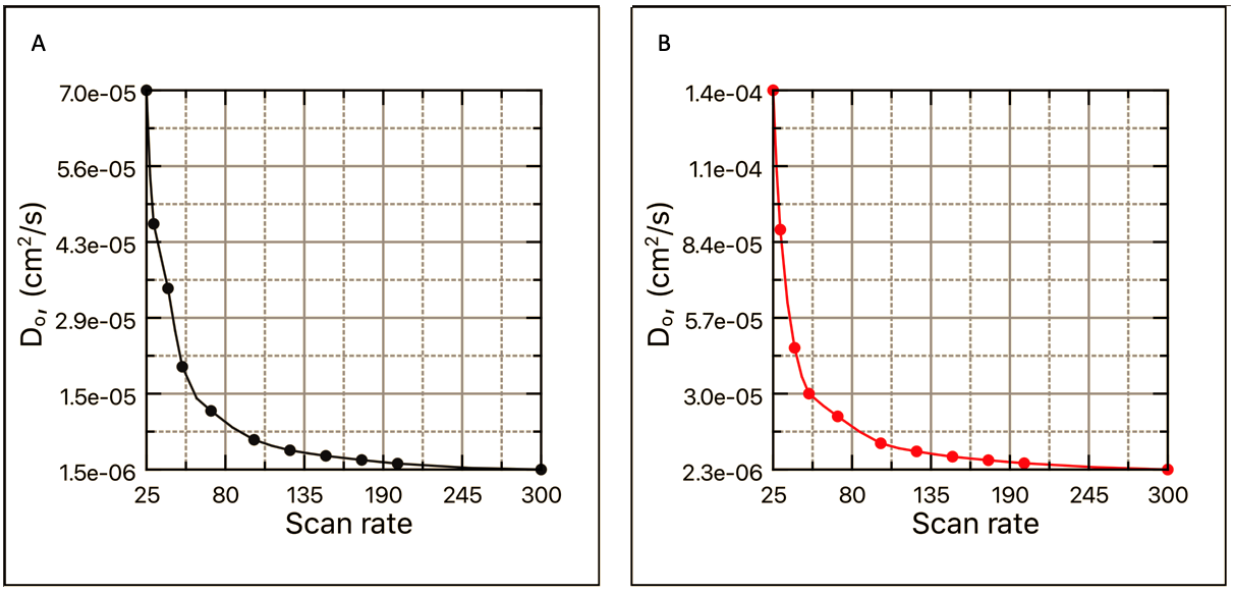

Figure 4.21: Exponential decrease of the diffusion coefficient with increasing scan rate

4.3.2. Concentration Dependence on CV response

Figure 4.22 shows cyclic voltammograms of the “etched” CuO photoelectrode in the presence of various concentrations of glucose in the dark and light at a 100 mV/s scan rate. A typical electrochemical response was recorded under both conditions. Interestingly, upon increasing the glucose concentration, the anodic peaks shift toward higher oxidative potentials. Similarly, the positive sweep peak currents increased with glucose concentration. The onset potential remained mostly unchanged regardless of glucose concentration. Also, the semiconductive properties of the “etched” CuO film is showcased with vastly greater oxidation peak current in the light as oppose to the dark under the same conditions. Under illumination, the 5mM glucose response lost its characteristic oxidation peak and appeared to be saturated. In contrast, the dark CV presented clearly visible oxidation peak however, above 5 mM glucose, the CV responses were completely saturated showing no clear oxidation peaks.

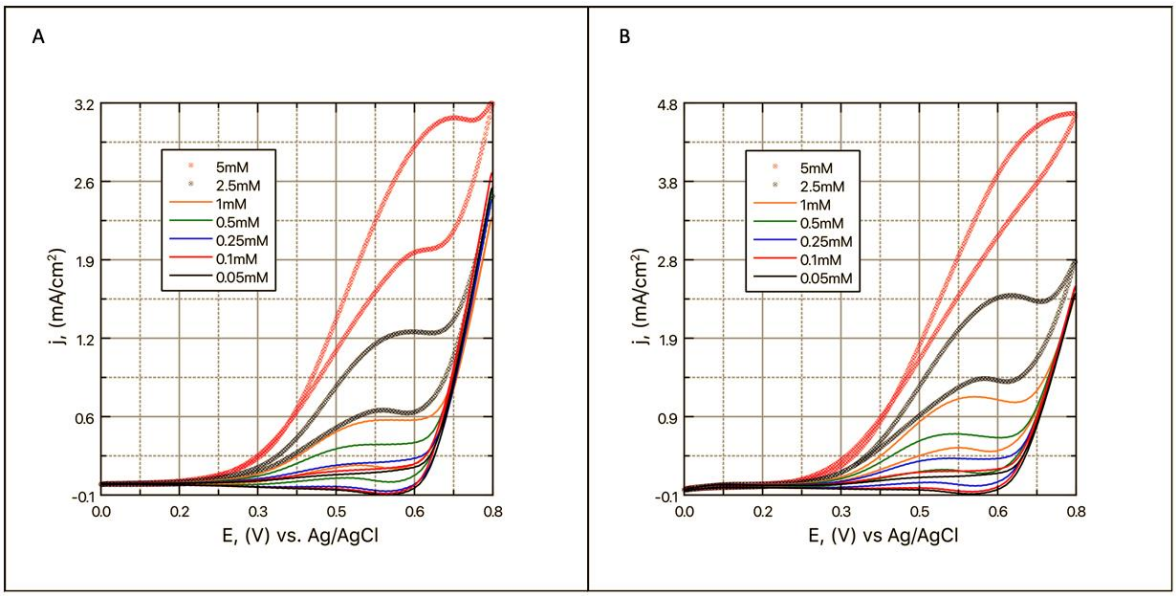

Figure 4.22: Cyclic Voltammograms at various glucose concentrations (0.05, 0.1, 0.5, 1.0, 2.5 and 5 mM) respectively, at 100mV/s scan rate under the A) Dark and B) light condition

4.3.3. A proof of concept

An increase of 0.08mA/cm^2 was recorded when illuminating the “etched” CuO photoelectrode with a standard iPhone 6S LED ($\approx 7\,W$) over its dark counterpart as shown in Figure 4.23. Though this is a minuscule performance increase, it goes to show that making use of the built-in semiconductive properties can result in increased performance. According to StatsSA (2021), at current, there are approximately 24.5 million smartphone users in south Africa compared to the 9.7 million users in 2014. This illustrates the dramatic increase in access and use of smartphone devices in 7 years alone. Smartphones inherently have LED lights built-in and with further performance enhancement could give these users access to a reusable non-enzymatic glucose sensor on the go.

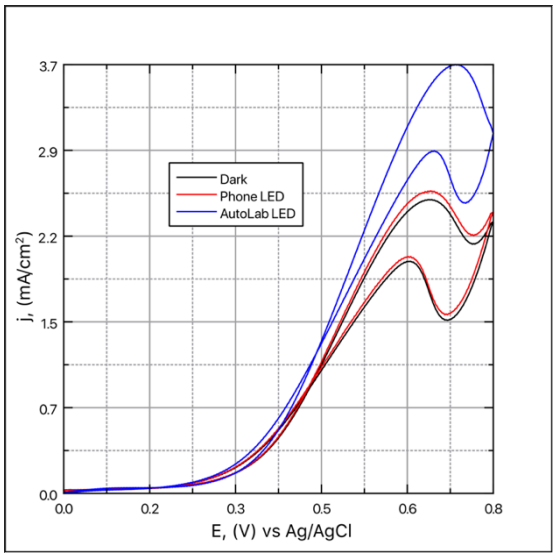

Figure 4.23: Cyclic voltammograms for the “etched” CuO photoelectrode in the dark and under illumination from an iPhone and AutoLab cool white LED in 5 mM Glucose and 100 mV/s Scan Rate

4.3.4. Reproducibility, Shelf-Life and Repeatability

The reproducibility of the etched CuO thin film was electrochemically tested using CV in a solution of 0.1 M NaOH and 1 mM Glucose. Samples were first stabilized at a scan rate of 100 mV/s for ten cycles and the data was recorded at 50 mV/s. Anodic peak current densities of the five prepared samples were recorded at 0.54 V vs Ag/AgCl. The reproducibility of the etched CuO films is represented in Figure 4.24. This shows excellent electrode reproducibility in both the light (RSD = 4.85%) and dark (RSD = 1.86%) scenarios.

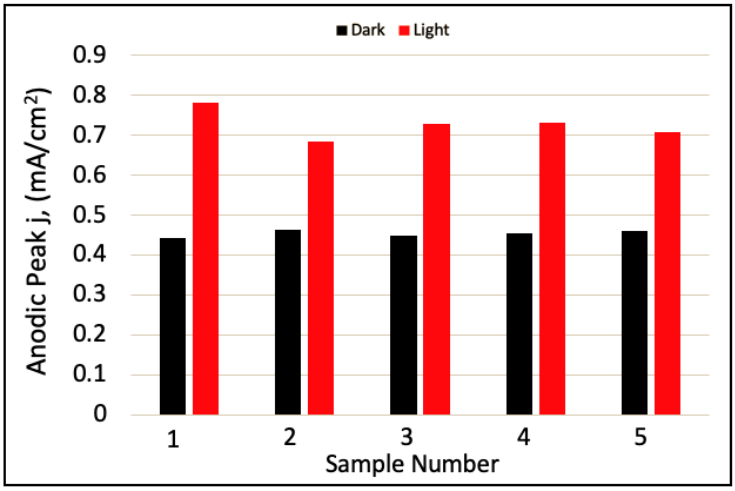

Figure 4.24: Electrode reproducibility test for five samples in light and dark conditions

Similarly, the shelf life of the CuO electrode was validated under the aforementioned conditions. An etched sample was selected and repeatedly tested over a period of one month (1-day, 2-days, 4-days, 7-days, 14-days, 21-days, and 28-days). The results depicted in Figure 4.25 reveal that in the dark the deterioration was subtle with the largest photocurrent decrease (0.026 mA/cm^2) occurring between 2 and 4 days. In the light however, clear evidence of photo-corrosion is seen with much larger deterioration over the same time frame. The RSD's for the dark and light condition were found to be 2.40% and 4.56% respectively. This emphasizes how much more the sensors response deteriorates over the testing period.

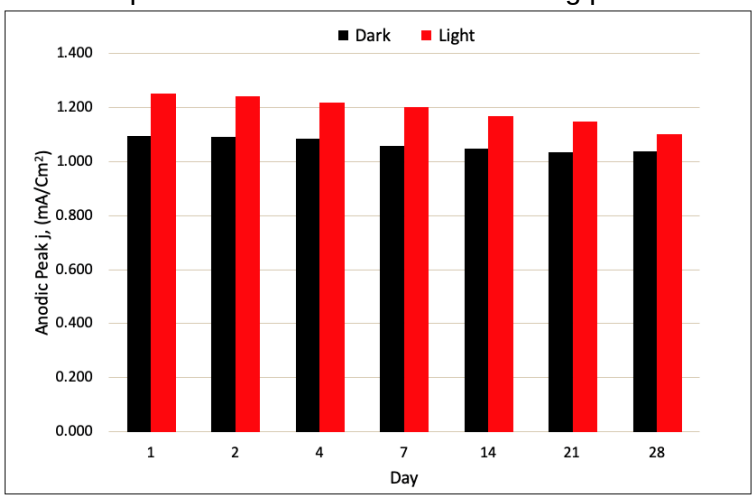

Figure 4.25: Etched CuO photoelectrode Shelf-life assessment

Under these same conditions, one electrode was subjected to repeated CV cycles to assess the repeatability of the anodic peaks obtained. As per Figure 4.26, it was found that the oxidation peaks for this sample were very repeatable over 10 Cycles for both the dark and light with RSD's of 1.98% and 1.75% respectively.

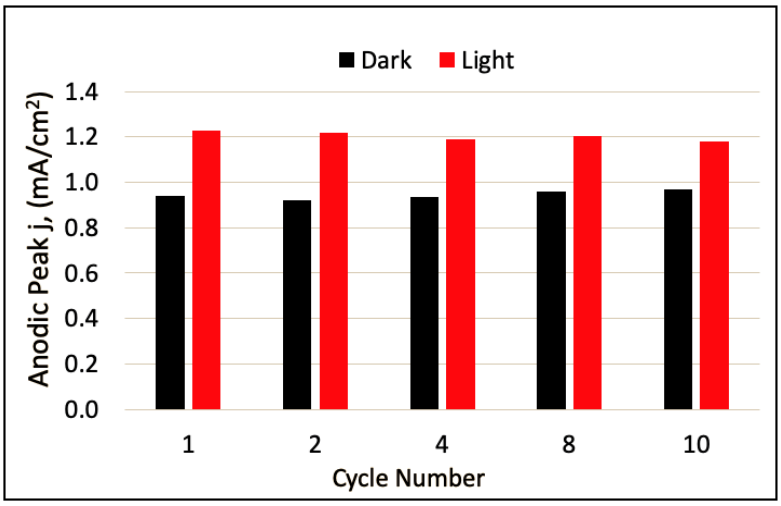

Figure 4.26: Peak anodic currents for a series of 10 CV cycles on the same etched CuO sample illustrating repeatability

4.4. Charge Carrier Transport

The electrochemical impedance characterization of selected samples was carried out in a solution of 0.1 M NaOH with various glucose concentrations both in the dark and under illumination. The impedance studies were carried out over a frequency range of 100 kHz to 0.01 Hz using an AC perturbation with a magnitude of 5 mV at room temperature without stirring. A Nyquist plot alludes to the charge transfer kinetics as well as diffusion characteristics of a given sample. The Nyquist plot for a simple charge transfer reaction is characterized by a semicircle in the high frequency region and a straight line increasing into the low frequency region at 45°. This line in the low frequency region represents Warburg impedance and is the region which is dominated by fast kinetics leaving diffusion as the rate limiting process. Conversely, the high frequency region is limited by slow kinetics and so a semicircle is formed. The diameter of the semi-circle represents the charge transfer resistance R_{CT} in (Ω). The solution resistance R_s is found on the real axis and is independent of frequency. The impedance measurements were used to construct Nyquist plots over a range of glucose concentrations as presented in Figure 4.27. From the EIS data represented in Figure 4.27, it can be seen that the shape of Nyquist plots varies drastically between the light and dark condition. In the dark, the Nyquist plots displayed flattened and incomplete capacitive arcs which decrease in size with increasing glucose concentration. Typically, this feature is associated with the formation of a passive film over the surface of the electrode. In the light this is only true at low concentrations where at concentrations above 1 mM, the diameter of the Nyquist plot increases. This due to the fact that the charge transfer mechanism is much

more complex in the light. Under illumination, higher glucose concentrations produce a larger barrier to interfacial charge transfer which may be as a result of decreased OH- ion concentration near the surface of the electrode.

The formation of such a film was visually confirmed using SEM imaging following EIS testing over the entire frequency range and are displayed in Figure 4.28. Interestingly, electrochemical testing of the samples revealed the formation of small crystals all across the samples surface. In an alkaline environment, Cu forms a passive layer over its surface which in effect retards further corrosion (Rios, Calderón and Nogueira, 2011). In both the light and dark scenarios, the absence of glucose resulted in the formation of the largest arcs. Figure S7 included in the supplementary depicts the 1 mM Glucose fits over the whole frequency range.

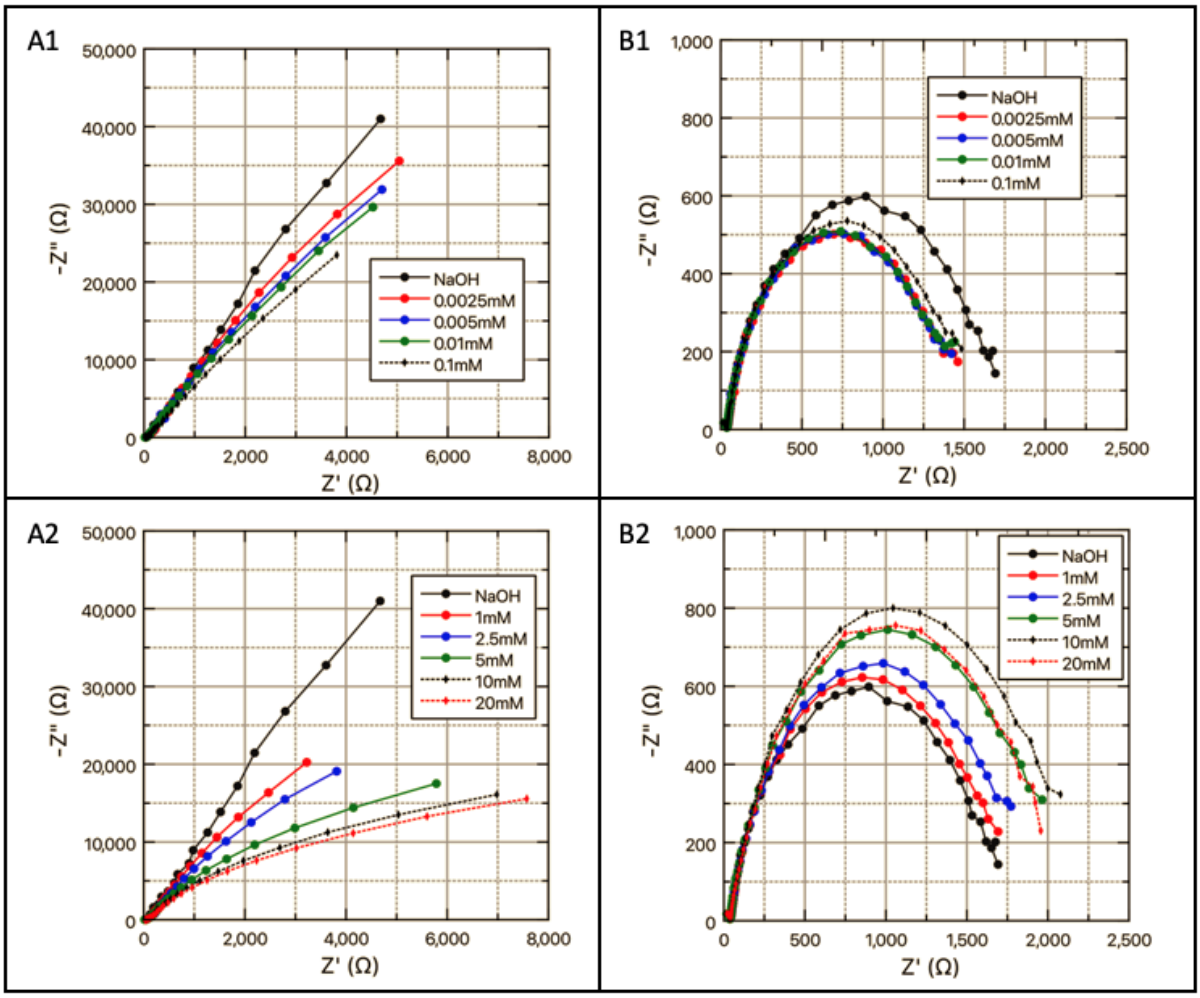

Figure 4.27: Nyquist plots in the dark (A1 and A2) and under illumination (B1 and B2) over a range of glucose concentrations

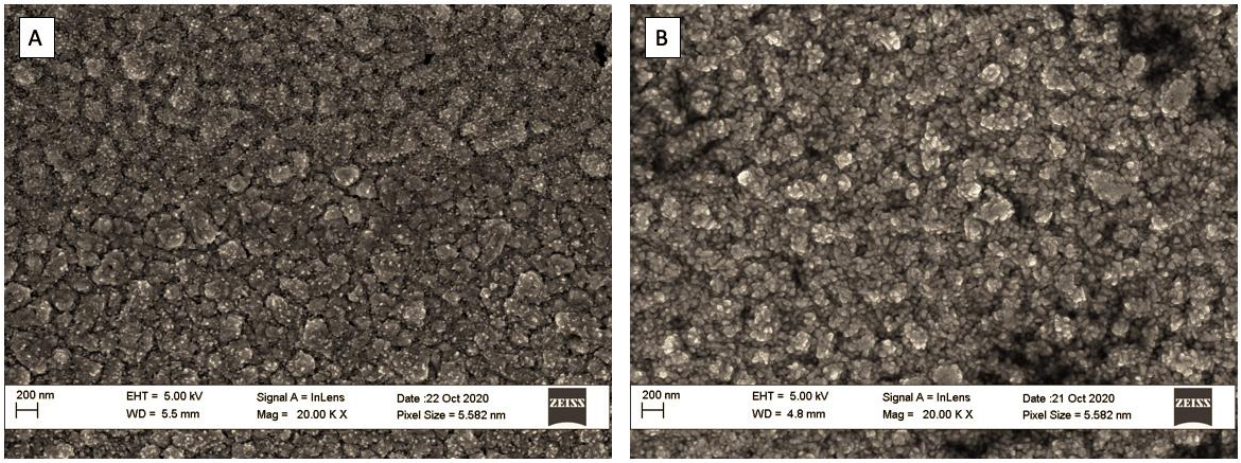

Figure 4.28: Top scan SEM images for samples following EIS testing A) As Deposited 50-cycles and B) Etched 50-Cycles

Under illumination, a clear depressed semi-circle is visible both in the presence and absence of glucose. The semi-circle peak in the medium frequency range increases with glucose concentration suggesting higher charge transfer resistances between the solid and electrolyte interface (R_{CT}). The analysis of Nyquist plots in the high and medium frequency region is especially complex and to accurately interpret charge carrier transport, an appropriate equivalent circuit must be used to fit the EIS data. Previously, Yang et al., Meng and Liu made use of a modified Randel's circuit with a double parallel arrangement to depict EIS data in an equivalent circuit for two-time constants (Yang *et al.*, 2018; Meng and Liu, 2019). Due to the grain-like morphology and nature of the coating, the circuit presented in Figure 4.29 will be used to further interpret the EIS data as the diffusion paths are similar.

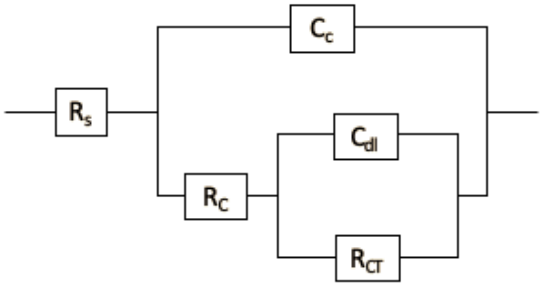

Figure 4.29: Modified Randel's circuit in a double parallel configuration for two-time constants used in this work as the equivalent circuit

From the electrical equivalent circuit, R_s represents the solution resistance, R_C and C_c denote the coating resistance and capacitance respectively whereas C_{dl} is the double layer capacitance and R_{CT} is the charge transfer resistance. The capacitive elements were replaced with constant phase elements (CPE) to account for the scattering effect as a result of surface heterogeneity (Zhang *et al.*, 2004). Enzymatic sensors require CPE's to describe the impedimetric responses due to adsorption however; CuO is non-enzymatic and so does not rely on a mediator to facilitate a chemical reaction. It is therefore common practice to make

use of CPE's as the electrochemical responses are believed to be purely capacitive in nature. The aforementioned circuit was used to fit both the light and dark scenarios with great success. The equation derived from this circuit including CPE components is complex and required many term designations so as to not confuse the inside parallel with the outside one. The inside parallel is designated as follows:

$$\text{If } Z_{CPE} = \frac{1}{y_0(jw)^n} \qquad \text{let } -n = m_2 \; and \; Y_2 = \frac{1}{y_o} \qquad \text{thus, } Z_{CPE} = Y_2(jw)^{m_2}$$

$$\text{Where, } j^{m_2} = Cos\left(\frac{\pi m_2}{2}\right) + jSin\left(\frac{\pi m_2}{2}\right)$$

$$\text{And so, } C_{dl} = CPE_{21} = Y_2 w^{m_2} Cos\left(\frac{\pi m_2}{2}\right) \text{ and } CPE_{22} = Y_2 w^{m_2} Sin\left(\frac{\pi m_2}{2}\right)$$

Y_n represents the magnitude of the CPE, w is the angular frequency in rad/s, j is an imaginary number and m_n is the inverse of the exponent related to surface heterogeneity. The inside RC parallel's equation is:

$$Z_{inside} = R_C + \frac{R_{CT}(CPE_{21} + jCPE_{22})}{(CPE_{21} + R_{CT}) + jCPE_{22}}$$

After some work, separating the real from the imaginary parts of the equation reveals $X_{Real} \; and \; X_{imag}$:

$$X_{Real} = R_C + \frac{R_{CT}(CPE_{21})^2 + CPE_{21}(R_{CT})^2 + R_{CT}(CPE_{22})^2}{(CPE_{21})^2 + 2R_{CT}CPE_{21} + (R_{CT})^2 + (CPE_{22})^2}$$

$$X_{imag} = \frac{CPE_{22}(R_{CT})^2}{(CPE_{21})^2 + 2R_{CT}CPE_{21} + (R_{CT})^2 + (CPE_{22})^2}$$

The equation for the outside parallel was established in a similar manor though is more tedious with the additional real and imaginary parts:

$$C_c = CPE_{11} = Y_1 w^{m_1} Cos\left(\frac{\pi m_1}{2}\right) \text{ and } CPE_{12} = Y_1 w^{m_1} Sin\left(\frac{\pi m_1}{2}\right)$$

$$\text{And so, } Z_{outside} = R_s + \frac{(CPE_{11} + jCPE_{12})(X_{Real} + jX_{imag})}{(CPE_{11} + X_{Real}) + j(CPE_{12} + X_{imag})}$$

Finally, the overall equation used to fit all the EIS curves is a combination of the inside and outside X designations:

$$Z_{Circuit} = R_s + \frac{(CPE_{11}X_{Real} - CPE_{12}X_{imag}) + j(CPE_{12}X_{Real} + CPE_{11}X_{imag})}{(CPE_{11} + X_{Real}) + j(CPE_{12} + X_{imag})}$$

Using the overall circuit equation upon separating the real from the imaginary, the fitting parameters were found using Microsoft excel and Excel's Solver add-in. The results are tabulated (Table 4.5: Dark, Table 4.6: Light) for both the light and dark conditions under various glucose concentrations. The difference in charge transfer resistance between the light and dark condition is staggering with the light condition enjoying (R_{CT}) which are several orders of magnitude smaller. In the dark, the charge transfer resistance (R_{CT}) fluctuates slightly at low glucose concentrations (0.0025 mM to 0.025 mM) and then peaks at 0.1 mM. This indicates that between a blank solution up to 0.1 mM, the charge transfer process is most difficult at this concentration. By increasing the glucose concentration (0.1 mM to 20 mM) the charge transfer resistance decreases to levels below that of the blank solution indicating a more favorable charge transfer process. In the light however, the R_{CT} decreases from 1634 Ω/cm^2 in a blank solution until a minimum is reached at 1377 Ω/cm^2 for 0.005mM glucose. The R_{CT} then increases steadily to 2146 Ω/cm^2 in 15 mM glucose before decreasing again. The surface heterogeneity factor in both the light and dark are close to n =1 indicating good surface exposure to the electrolyte.

Table 4.5: Parameters used to fit dark EIS data through Microsoft excel using two-time constants

Dark							
Concentration	Fitting Parameter						
	$R_s,\ \Omega$	$R_C,\ \Omega$	$R_{CT},\ \Omega$	C_c	n_{C_c}	C_{dl}	$n_{C_{dl}}$
Blank	3.36E-07	46.14	3.41E+07	1.03E-06	0.833	3.59E-05	0.937
0.0025mM	1.08E-04	42.43	1.72E+08	6.89E-07	0.792	4.42E-05	0.911
0.005mM	6.35E-04	40.90	3.98E+08	5.90E-07	0.804	4.91E-05	0.913
0.01mM	1.44E-03	39.63	2.10E+08	4.76E-07	0.821	5.28E-05	0.912
0.025mM	5.73E-06	41.47	2.76E+08	1.03E-06	0.763	5.63E-05	0.907
0.05mM	1.07E-06	39.41	4.04E+06	4.99E-07	0.819	6.07E-05	0.904
0.1mM	3.05E-03	39.03	4.11E+10	3.45E-07	0.848	6.67E-05	0.894
0.25mM	7.36E-07	39.61	5.89E+08	3.64E-08	0.944	6.35E-05	0.914
0.5mM	1.10E-04	38.74	5.29E+07	3.49E-07	0.848	7.68E-05	0.887
1mM	5.92E-07	40.93	1.28E+06	3.43E-07	0.847	8.08E-05	0.908
2.5mM	9.71E-07	39.65	1.54E+08	3.38E-07	0.849	8.51E-05	0.871
5mM	9.59E-07	39.01	4.99E+05	2.56E-07	0.871	8.84E-05	0.869
10mM	3.81E-06	39.50	1.53E+05	2.57E-07	0.869	9.01E-05	0.863
15mM	5.12E-06	41.74	1.97E+06	3.68E-07	0.841	8.84E-05	0.856
20mM	1.55E-05	41.76	1.30E+05	3.80E-07	0.839	8.89E-05	0.851

Table 4.6: Parameters used to fit light EIS data through Microsoft excel using two-time constants

Light							
Concentration	Fitting Parameter						
	$R_s,\ \Omega$	$R_C,\ \Omega$	$R_{CT},\ \Omega$	C_c	n_{C_c}	C_{dl}	$n_{C_{dl}}$
Blank	5.90E-07	42.10	1634	4.32E-07	0.826	7.03E-05	0.819
0.0025mM	5.57E-07	39.53	1400	2.71E-07	0.864	8.17E-05	0.816
0.005mM	1.46E-03	38.43	1377	2.31E-07	0.877	8.44E-05	0.828
0.01mM	1.91E-06	37.45	1380	1.93E-07	0.892	8.85E-05	0.830
0.025mM	1.91E-07	38.74	1537	2.88E-07	0.862	8.91E-05	0.833
0.05mM	1.08E-05	37.19	1406	1.76E-07	0.900	9.64E-05	0.829
0.1mM	7.21E-07	37.32	1441	1.75E-07	0.901	9.99E-05	0.829
0.25mM	7.46E-08	37.69	1517	1.72E-07	0.903	1.07E-04	0.821
0.5mM	4.12E-06	36.92	1545	1.58E-07	0.910	1.12E-04	0.821
1mM	1.55E-06	38.44	1684	1.84E-07	0.898	1.15E-04	0.818
2.5mM	6.60E-07	39.82	1763	1.28E-06	0.749	1.12E-04	0.826
5mM	2.79E-03	37.32	1998	1.47E-07	0.915	1.18E-04	0.818
10mM	1.39E-04	38.23	2120	1.65E-07	0.905	1.14E-04	0.823
15mM	7.55E-08	40.79	2146	3.96E-07	0.838	1.13E-04	0.818
20mM	2.02E-07	40.24	2025	2.03E-07	0.888	1.14E-04	0.814

Upon closer inspection of both the light and dark conditions in a 1 mM glucose testing solution, a smaller depressed semicircle is observed as a tail in the high frequency region as per Figure 4.30. This high frequency region semi-circle is attributed to the resistance of the surface passivating layer (Xiang *et al.*, 2011). The Bode-modulus plot reveals constant phase behavior in the middle and high frequency region in the dark. Conversely, in the light, this constant phase behavior is only very slightly noticed in the lower end of the high frequency range. According to the Bode-phase plot, one-time constant is observed in the high frequency region and another in the mid frequency region. The latter corresponds to the charge transfer reaction whereas the former represents the properties of the passive film form on the surface during testing (Yang *et al.*, 2018). In both dark and light, the solution resistance (R_s) is seen to fluctuate. These deviations can be attributed to inhomogeneous mixing following the addition of glucose to the testing solution. It was expected the solution resistance would increases with increased glucose concentration as glucose does not dissociate into its ions making it a poor conductor in solution. This however is not the case as the concentrations used are so limited it has little effect on the solution resistance. Finally, the relationship between glucose concentration and charge transfer resistance was found to not be strong enough to accurately detect glucose concentrations.

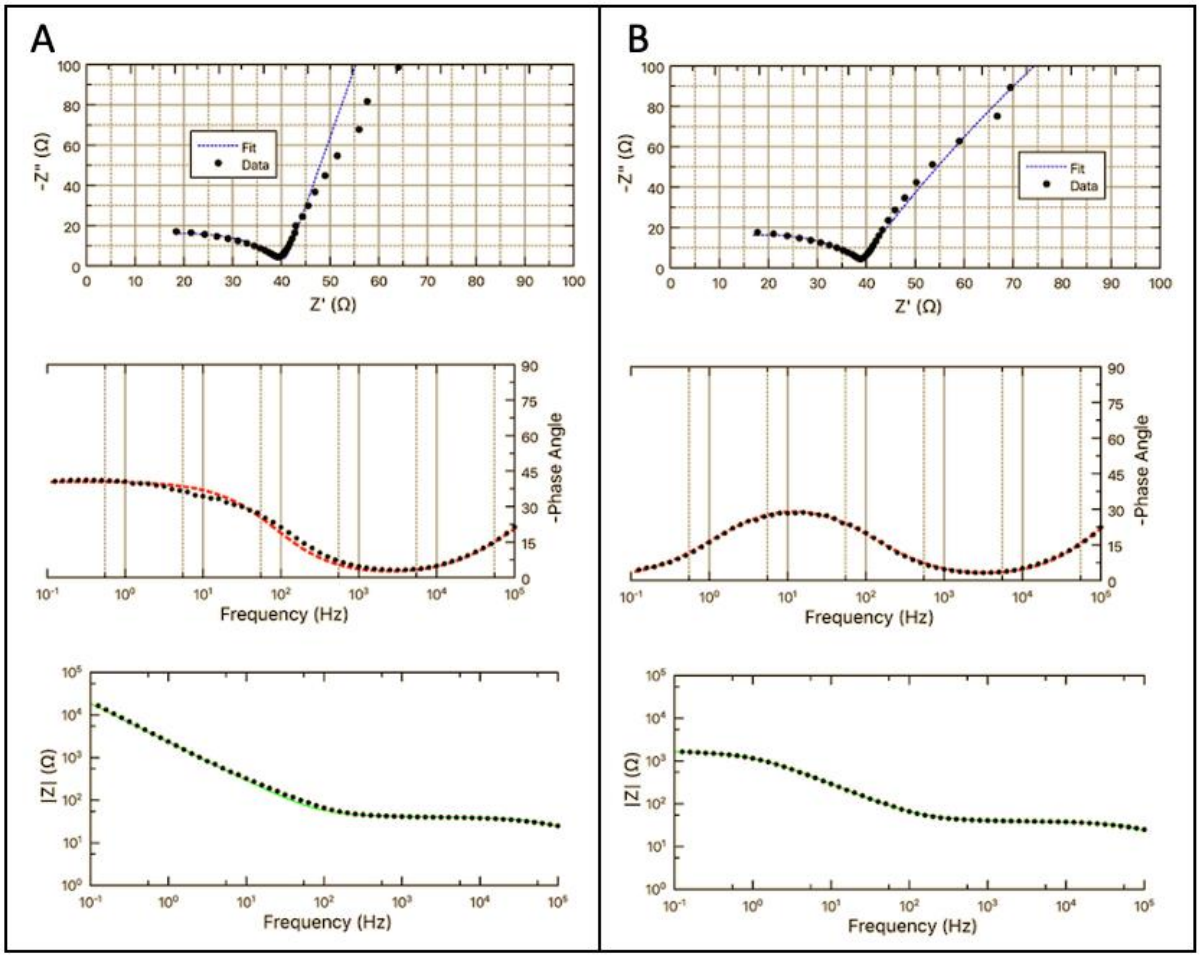

Figure 4.30: Zoomed in view of fitted high frequency Nyquist and Bode plots using the modified Randel's circuit in A) Dark and B) Light for 1 mM glucose

An investigation into the determination of k^o via EIS as oppose to CV was conducted by Edward P. Randviir who found that both approaches are comparable (Randviir, 2018). Due to the irreversible nature of the reaction between glucose and CuO, an accurate determination of the standard reduction potential is not possible and hence should rather be examined via EIS. As such, the R_{CT} is related to the exchange current (i_o) and subsequently the heterogeneous electron transfer rate (k^o) by the expressions:

$$R_{CT} = \frac{RT}{nFi_o} \qquad \text{and} \qquad i_o = nFAC_o k^o$$

Where R is the universal gas constant, T is the temperature, n is the number of electrons (can be considered as = 1) and F which is faradays number. By applying these equations, the mean electron kinetic transfer rate over a glucose concentration range of 0.1 mM to 20 mM, was found to be 9.7E-08 cm/s and 3.46E-04 cm/s in the dark and light respectively. These k^o values align well with other reports using CV measurements as oppose to EIS thus further confirming the findings by Randviir (Torto, Ruzgas and Gorton, 1999; Sattarahmady and Heli, 2012; Randviir, 2018).

4.5. Chronoamperometric Measurements

The chronoamperometric detection of glucose was carried out to determine the current response of the CuO photoelectrode samples to successive glucose injections. From the CV's, the E_p occurred between 0.55 V and 0.60 V which were subsequently used as the applied potentials for the analysis in the dark and light. An interval time of 50 s between each successive glucose addition was used under constant stirring in 0.1 M NaOH solution. Though this interval time is long, the time taken to reach a steady state current was rapid. Table 4.7 shows the injection time and total glucose concentration present within the system.

Table 4.7: Successive glucose injections with respect to time and the decrease in NaOH concentration as a result of glucose additions

Injection Time (s)	Glucose Concentration (mM)	NaOH Concentration (mM)
0	0.00	100.00
50	0.02	99.99
100	0.06	99.98
150	0.17	99.93
200	0.41	99.84
250	0.89	99.65
300	1.68	99.33
350	2.77	98.89
400	4.15	98.34
450	5.81	97.67
500	7.75	96.90
550	9.95	96.02
600	12.39	95.05
650	15.05	93.98
700	17.93	92.83
750	21.26	91.50
800	25.00	90.00
850	29.12	88.35

The chronoamperometric data presented in Figure 4.31 for the "As-Deposited" sample shows a very inconsistent staircase type structure in both the light and dark. This can be attributed to the lack of crystallinity in the as deposited sample. At low concentrations this classical step increase is very pronounced though upon increasing the glucose concentration, the readings become less stable. Both the calcined and etched samples however retain this staircase structure throughout testing and steady state is reached rapidly upon glucose injection. Following calcination, the CuO layer is much more crystalline than its as-deposited counterpart. The large decrease in current density at higher glucose concentrations could be as a result of the decrease in porosity of the CuO layer. This is confirmed as post etching; the porosity is greatly increased and yields a higher current density in both light and dark conditions. Also, in each case, the dark current density is lower than that in the light further showcasing the benefits of making use of the built-in semiconductive properties of CuO.

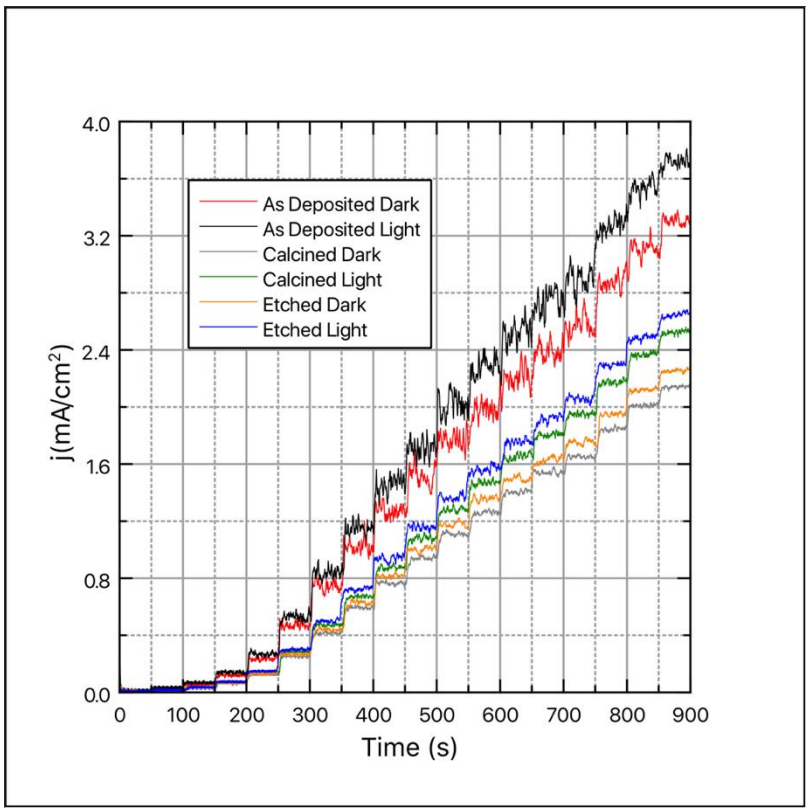

Figure 4.31: Current response of selected samples during each stage of synthesis (As-deposited, Post Calcination and Post Etching)

4.5.1. Different voltages etched

With the CV measurements having been conducted in 1mM glucose, the associated peak potential is mostly constant. Upon altering the glucose concentration, the peak potential as well as peak current would shift slightly. As a result, independent chronoamperometric studies were conducted under 0.55 V, 0.57 V and 0.6 V bias to obtain a clearer view of the impact the applied potential has over a range of concentrations. Upon finetuning the applied voltage, the largest difference between light and dark current density is achieved at 0.55 V as presented in Figure 4.32. Over the range of applied potentials, the iconic staircase rise in current is evident in the dark and light. It is evident that as the applied voltage is increased, the difference between light and dark current decreases. This suggests the possibility of a maximum current difference between the dark and light scenario as seen in the CV measurements. The chronoamperometric data in Figure 4.32 shows that glucose detection in concentration levels below 0.41 mM show no significant difference between the dark and illuminated samples. Above this concentration, the semiconductive behavior of the CuO photoelectrode becomes apparent with higher current responses to the same glucose concentration. The divergence between the recorded current and the glucose concentration measured in the dark and light continues to grow even after an addition of 20 mM glucose.

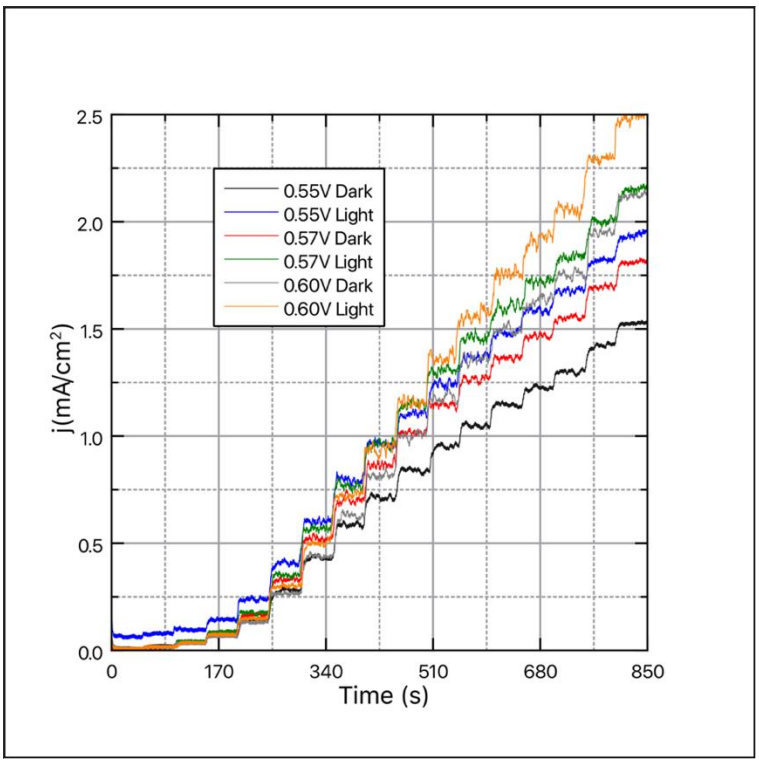

Figure 4.32: Chronoamperometric measurements completed under dark and light conditions with 0.55V, 0.57V and 0.60V bias

A closer inspection of the 0.60 V “etched” sample’s chronoamperometric response (Figure 4.33) confirms that the difference between light and dark only becomes apparent following the addition of 0.41 mM of glucose. After this critical point, the difference continues to grow even after the highest glucose concentration injection. Impressively fast response times of 4 s were recorded for both the dark and light tests indicating that light had no influence on the time taken to respond to glucose additions.

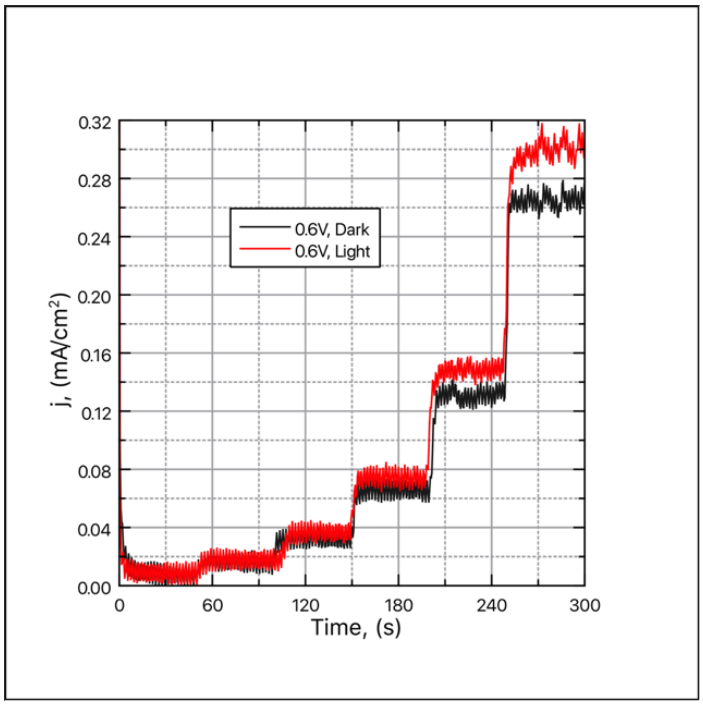

Figure 4.33: Zoomed view of chronoamperometric detection data at 0.6 V vs Ag/AgCl showing the first 300 seconds in the light and dark

The peak currents following each successive glucose injection were determined and plotted against the respective glucose concentrations to develop a calibration curve. Figure 4.34 shows this calibration curve for the “etched” CuO sensor in the light and dark. A total of 3 linear ranges (LR-1, LR-2 and LR-3) are clearly identified under both scenarios with strong correlation coefficients. LR-1 covers a 0-2.77mM glucose range, LR-2 spans across 2.77-9.95 mM and LR-3 covers the largest range between 9.95 mM to 29.12 mM glucose. Interestingly, these linear ranges were not altered by the inclusion of light in the system however the correlation coefficients of LR-1 are seen to increase from dark to light and decrease for the LR-2 range. The increased oxidation current of the optimized CuO thin film also had no effect on the linear ranges. With smaller formations on the surface of the etched electrode, the surface area is increased. This increase in surface area has been reported to cause small increases in linear range though coupled with good adhesion to the FTO substrate, the linear range is further enhanced. The major contribution to the increased linear range is believed to be as a result of the enhanced electronic properties and more specifically charge carrier mobility and conductivity. With such high conductivities, charge carrier separation is easily attainable. Studies by other authors show that an increased LR results in a lower sensitivity. The sensitivity and limit of detection however were greatly influenced by illumination. The sensitivity in the dark was found to be $197\ \mu A/mMcm^2$ whereas in the light it increased to $263\ \mu A/mMcm^2$. The low sensitivity could be attributed to the aforementioned high charge carrier concentration. This is supported by numerous reports concerning semiconductors having decreased sensitivity as a result of increased charge carrier density (Torto, Ruzgas and Gorton, 1999; van den Heever and Perold, 2013; Chen *et al.*, 2018). Additionally, the LOD at (S/N) of 3 decreased from 0.079 to 0.059 mM showing enhanced lower detection limits under illumination.

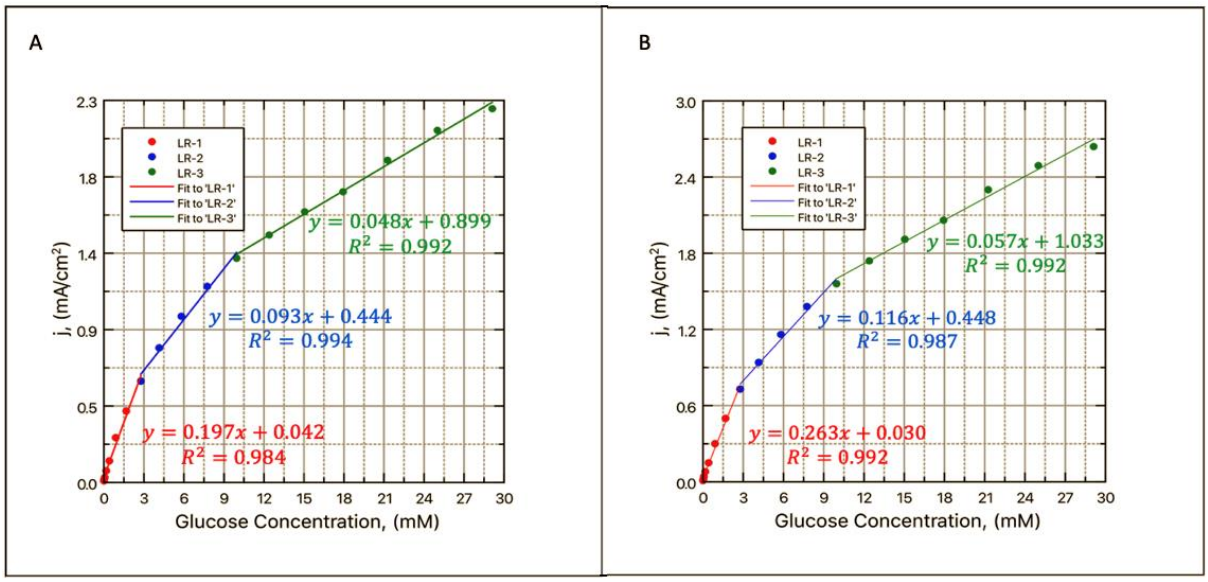

Figure 4.34: Calibration curve for the “Etched” CuO thin film depicting 3 linear ranges in the A) Dark and B) light

The detection properties for this sensor are highly comparable with many works as presented in Table 4.8. From this, it can be seen that the sensor developed in this work displays wide linear ranges as well as enhanced sensitivities as compared to other works with far less power output.

Table 4.8: Comparison drawn between this work and other similar CuO glucose sensors

Material	Light Source & Power, (W)	Synthesis Method	Linear Range, (mM)	Potential, (V)	LOD (S/N)=3, (μM)	Sensitivity, ($\mu A/mMcm^2$)	Response Time, (s)	References
Pt/TiO2/NTA	Mercury Lamp, NR	Anodization & Ion Exchange	0.50-4.50	0.4	0.2	10	NR, Not Reported	(Chen *et al.*, 2017)
PANI-TiO2	Mercury Lamp, 125.0	Vapor Phase Polymer-ization	0.02-0.140	0.5	5.33	163	NR, Not Reported	(Majumdar and Mahanta, 2020)
Anodic TiO2	Xenon, 150.0	Anodization	LR-1: 0-0.12 LR-2: 0.38-0.67	0.5	7.3	136	3.0	(Syrek *et al.*, 2019)
GCE/rGO/CdS/CoOx	Dark	Solvothermal & electro-deposition	0.001-0.6	0.40	0.87	120	3.0	(Ashrafi, Salimi and Arabzadeh, 2016)
GCE/rGO/CdS/CoOx	Blue LED, 1.0	Solvothermal & electro-deposition	0.001-0.6	0.40	0.40	224	3.0	
ZnS/CdS/PGE	Halogen Bulb, 250.0	Electro-deposition	0.2-8.0	0.80	90.0	39	NR, Not Reported	(Ertek, Akgül and Dilgin, 2016)
PBS/SiO2/AuNPs	Blue LED, NR	Dip-Coating	0.001-1	0.20	0.46	NR, Not Reported	NR, Not Reported	(Cao *et al.*, 2019)
CuO/FTO	Dark	Electro-deposited thin film and NH_3 Etched	LR-1: 0-2.77 LR-2: 2.77-9.95 LR-3: 9.95-29.12	0.60	79.9	197	4.0	This Work
CuO/FTO	Cool White LED, 6.0	Electro-deposited thin film and NH_3 Etched	LR-1: 0-2.77 LR-2: 2.77-9.95 LR-3: 9.95-29.12	0.60	59.5	263	4.0	This Work

4.5.2. Interference Study

An interference study was conducted to verify this sensors performance in terms of selectivity toward glucose in the presence of other interfering constituents present in human blood. At normal levels, these species include fructose (0.1 mM), sucrose (0.1 mM), NaCl (145 mM), uric acid (0.1 mM), citric acid (0.1 mM), ascorbic acid (0.1 mM) and acetaminophen (0.1 mM). As such, to mimic the constituents found in human blood the aforementioned interfering species were added to a testing solution containing 0.1 M NaOH. Figure 4.35 shows the current/time characteristics associated with the addition of these interfering species.

Table 4.9: Indication time and concentration of the species injected into the testing chamber

Injected Species	Concentration in mM	Injection Time
NaOH	0.1	0
D-Glucose	1.0	100
D-Fructose	0.1	200
D-Sucrose	0.1	300
NaCl	145	400
Uric Acid	0.1	500
Citric Acid	0.1	600
Ascorbic Acid	0.1	700
Acetaminophen	0.1	800
D-Glucose	1.0	900

The results from the interference study showed that even closely related monosaccharides such as fructose (isomeric to glucose) and sucrose did not result in any significant response at levels similar to those present in human blood. An addition of 0.1 mM uric acid produced the greatest interference with the CuO thin film with a decrease of almost 0.1 mA/cm2. This interference is ascribed to the anionic nature of the UA which causes a decrease in current density. The addition of light caused no changes in the sensor's response toward interfering species. A common cause for interference and catalyst poisoning comes in the form of Cl, however, in this work it can be seen that no poisoning occurred even at very high NaCl levels. Overall the response to glucose was significant before and after the introduction of interfering species which makes this "etched" CuO thing film a promising non-enzymatic biosensor.

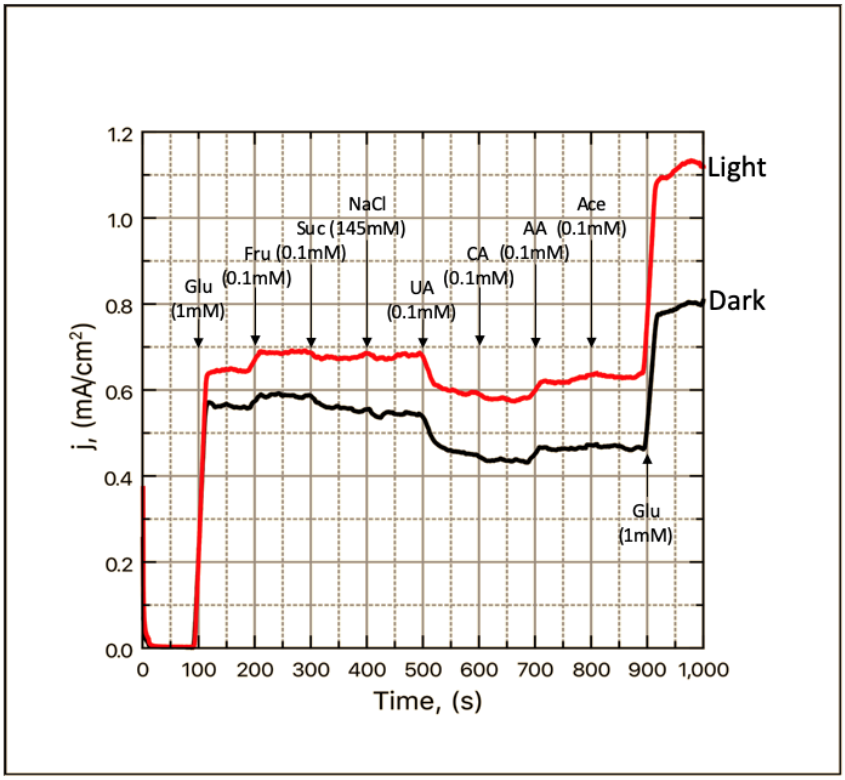

Figure 4.35: Chronoamperometric response to common interfering species on the “etched” CuO electrode in the dark and light

4.6. Persistent Photoconductivity

The recombination characteristics of charge carriers for the glucose sensor were evaluated under chopped light conditions. A three-electrode system was used in an optical glass box containing a range of glucose concentrations and 0.1 M NaOH. The Nova-2 software was set to turn the LED on and off at regular intervals during the testing phase at an applied voltage of 0.54 V vs Ag/AgCl. A depiction of the experimental setup is presented in Figure 4.36.

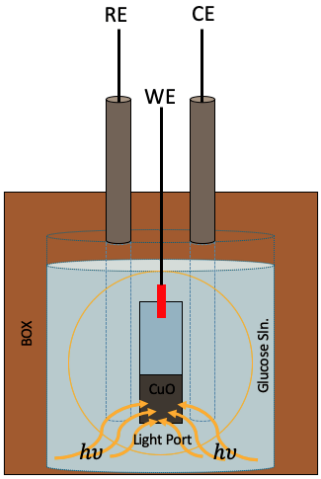

Figure 4.36: Light chopping experimental set-up

Figure 4.37 shows the intermittent illumination of the “etched” CuO photoelectrode which revealed a sharp increase in current the moment the semiconductor was exposed to light. At low glucose concentrations, a characteristic hump was formed during the first 5 seconds of illumination followed by a much slower current increase to its respective steady state. This initial spike can be attributed to the generation of electrons and holes which act in tandem with the Cu(III) species to rapidly oxidize glucose. Transients arise from the perturbations imposed on the system and the photo-generated charge results in a current which is measured against time. As previously described, the time difference between the old and new system equilibrium states can be used to define the transport parameters. The photo-generated transients were modeled using the triphasic stretched exponential function as follows.

$$I = i_o + A_1\left(e^{\frac{-t}{\tau_1}}\right) + A_2\left(e^{\frac{-t}{\tau_2}}\right) + A_3\left(e^{\frac{-t}{\tau_3}}\right)$$

Here, A represents a dimensionless weighting parameter associated with the amplitude of the photoinduced response, t denotes the time, i_o represents the dark current and τ is the RC time constants for each exponential term in agreeance with previous works (Li *et al.*, 2011, 2014; Bhatt *et al.*, 2019). The triphasic nature of the chopped light response indicates the presence of non-interacting charge carriers which act to shift the fermi energy level via their unique decay pathway. Furthermore, the rise and decay profiles reveal that the CuO photoelectrode is controlled via multiple processes which together result in its overall PPC behavior.

Figure 4.37 shows the tri-exponentially fitted rise and decay in photocurrent for this glucose sensor. A fast response in either the rise or decay when the light is on or turned off is indicative of a process which undergoes speedy charge carrier transfer. A fast response time is associated with band bending while a slow response is ascribed to charge carrier trapping in the presence of deep level traps that results in PPC behavior (Bhatt *et al.*, 2019). The concentration of glucose altered both the shape and intensity of the current rise and decay curves. At low concentrations up to 1 mM, the electron-hole recombination appeared prevalent though upon increasing the amount of glucose in the system, the charge carrier elimination effects became less obvious. The parameters during the rise A_1 and τ_{1R} in the above equation arise as a result of this initial spike which is attributed to the electron-hole pair recombination. A slower increase in photocurrent following this spike is as a result of the adsorption of OH^- to the surface active CuO sites. This gradual rise follows PPC behavior that lasts much longer than the initial spike. The diminishing rise of current until the light cut-off point confirms that A_{2R}/A_{3R} and τ_{2R}/τ_{3R} are associated with the adsorption processes. Following the termination of the light source the current slowly dissipates though never attains its starting current even after 130s post illumination. This decay is attributed to a combination of desorbing species as

well as oxidation products leaving the surface vicinity. This slow dissipation after illumination is highly characteristic for systems which experience persistent photocurrent as a result of limited interaction at deep trap states with re-adsorbed species (Park, Lee and Chang, 2016). The previously excited electrons energy is decreased to levels before illumination causing them to rejoin the VB and fulfilling Shockley-Read-Hall recombination. Interestingly, it can be noted that the rising time constant τ_{2R} with glucose concentration is much faster than for the decay time constant. Conversely, the decay time constants τ_{1D} and τ_{3D} are faster for the decay region than in the rise for increasing concentrations. It is this comparably fast adsorption process which results in the drastic increase in glucose oxidation when light is incident on the CuO photoelectrode.

Table 4.10: Fitting parameters for light chopping rise region

[Glucose], mM	A_1	τ_{1R}	A_2	τ_{2R}	A_3	τ_{3R}
0.0	1.50E-03	7.93E-02	1.30E-06	3.97E-01	-1.50E-03	7.93E-02
0.1	1.54E-03	9.55E-02	1.84E-05	4.02E-01	-1.54E-03	9.84E-02
0.3	1.56E-03	1.03E-01	5.48E-05	4.65E-01	-1.55E-03	1.13E-01
0.5	1.61E-03	1.12E-01	1.06E-04	4.73E-01	-1.59E-03	1.34E-01
1.0	1.78E-03	8.23E-02	1.91E-04	2.92E-01	-1.75E-03	1.07E-01
2.5	5.07E-03	1.10E-01	4.54E-04	4.25E-01	-4.96E-03	1.39E-01
5.0	5.21E-03	1.28E-01	8.38E-04	5.05E-01	-5.05E-03	1.88E-01
10.0	6.36E-03	1.30E-01	1.30E-03	2.96E-01	-6.83E-03	1.63E-01
15.0	1.11E-02	7.18E-02	2.72E-04	2.14E-01	-1.08E-02	7.25E-02
20.0	9.85E-03	7.18E-02	2.12E-04	2.69E-01	-9.62E-03	7.22E-02

Table 4.11: Fitting parameters for light chopping decay region

[Glucose], mM	A_1	τ_{1D}	A_2	τ_{2D}	A_3	τ_{3D}
0.0	-1.50E-03	5.84E-01	-1.30E-06	1.37E-02	1.50E-03	5.84E-01
0.1	-1.54E-03	6.14E-01	-1.84E-05	1.27E-02	1.54E-03	6.14E-01
0.3	-1.56E-03	6.34E-01	-5.48E-05	1.52E-02	1.55E-03	6.34E-01
0.5	-1.61E-03	6.29E-01	-1.06E-04	1.69E-02	1.59E-03	6.27E-01
1.0	-1.78E-03	5.43E-01	-1.91E-04	1.86E-02	1.75E-03	5.36E-01
2.5	-5.07E-03	9.43E-01	-4.54E-04	2.11E-02	4.96E-03	9.42E-01
5.0	-5.21E-03	9.59E-01	-8.38E-04	2.03E-02	5.05E-03	9.61E-01
10.0	-6.36E-03	1.25E-01	-1.30E-03	3.77E-02	6.83E-03	1.13E-01
15.0	-1.11E-02	2.47E-01	-2.72E-04	1.21E-02	1.08E-02	2.47E-01
20.0	-9.85E-03	2.61E-01	-2.12E-04	1.66E-02	9.62E-03	2.61E-01

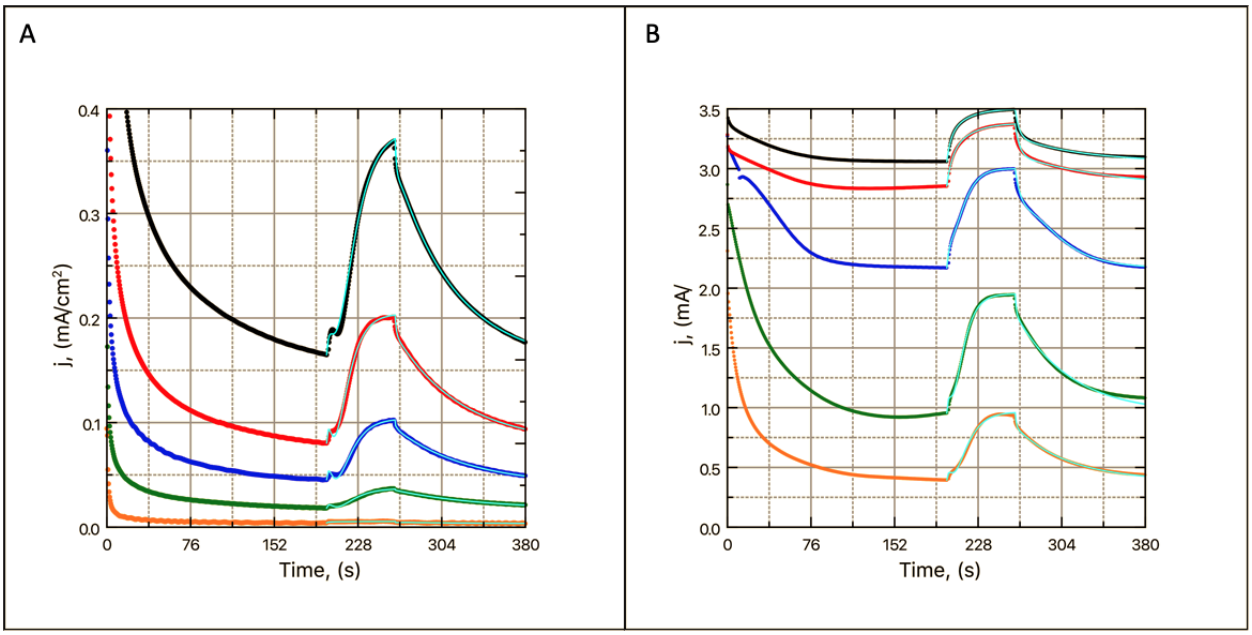

Figure 4.37: Light chopping at a 0.54V bias for A) Low concentrations (NaOH, 0.1, 0.25, 0.5, 1.0 mM Glucose) and B) High Concentrations (2.5, 5.0, 10.0, 15.0, 20.0 mM Glucose)

CHAPTER 5

CONCLUSIONS & RECOMMENDATIONS

5. Conclusion

A non-enzymatic CuO glucose sensor was successfully electrodeposited onto FTO. Film synthesis optimization included the identification of the optimal electrodeposition voltage and respective time. It was found that low voltages resulted in poor photocatalytic abilities whereas high voltage cause peeling between the CuO layer and FTO. The thin film was then subject to thermal oxidation for which the temperature and time effects were studied. At low temperatures, the films changed color from greyish-brown to yellow during testing which is an indication that the surface has irreversibly been changed. At high temperatures the photocatalytic current was found to be less than in the mid-temperature annealing. Finally, wet-chemical etching with NH_3 resulted in miniscule enhancements to the photocatalytic ability; however it was found that the band gap decreased significantly. Enhanced detection properties were exhibited at the optimized synthesis conditions for the CuO photocatalyst (4 V and 2 min electrodeposition, calcination at 450 ℃ for 1 hour and NH_3 etched for 2 min).

At the optimal synthesis conditions, it was determined that the CuO film had a monoclinic structure. During glucose oxidation, the shape of the CV curves in the dark and light remained unchanged. Under illumination, the oxidation peak current was greatly enhanced as compared to in dark. Both systems were determined to follow irreversible electron transfer kinetics and that the oxidation of glucose at the electrodes surface is diffusion controlled. The enhanced photo-electrochemical response under illumination required an investigation into reaction mechanisms. The mechanism identified to occur in the light followed similar oxidation pathways as in the dark however, it was a combination of Cu(II)/Cu(III) and hydroxyl radicals produced following charge separation that is believed to be responsible for the increase current density. A higher kinetic rate constant and diffusion coefficient were obtained for the illuminated samples. In addition, lower charge transfer resistances were found in the light than in the dark. Also, under transient illumination, it was determined that deep trap states resulted in the formation of persistent photoconductivity. Chronoamperometric measurements revealed that the linear range of detection was unaffected by the increased current density in the light though the sensitivity and LOD were enhanced. In both light and dark, the selectivity toward glucose was acceptable with minimal interference from a wide range of interfering substances.

Recommendations:

Cyanide leaching is a well-known and industrially accepted process used in the recovery of gold. When gold ores that contain copper oxide or sulfides (Cu_2O, Cu_5FeS_4, $Cu(OH)_2$, CuS and Cu_2S) undergo cyanidation, the cyanide degrades which allows copper to become soluble in the form of cuprous cyanide complexes. In typical operations, these copper cyanide complexes are not recovered which not only increases the economic penalties against the operation but also the loss of valuable copper during effluent treatment. Though a number of pre and post cyanidation processes have been developed to address these complications, further research could expand to investigate the possibility of recovering copper from leach solutions to synthesize non-enzymatic sensors such as those present in this work.

Alternatively, the persistent photoconductivity (PPC) seen to occur over large time frames could be further investigated as a self-cleaning mechanism for glucose sensors. After removing the light source, the oxidation current slowly decreases over time. By pre-treating photocatalysts with light knowing that they retain PPC behavior, it is logical to think that the degradation of an electrode over time will be diminished and prolong the suitable use period of a given electrode.

References

Ahn, H. S. and Bard, A. J. (2016) 'Surface Interrogation Scanning Electrochemical Microscopy of $Ni_{1-x}Fe_xOOH$ (0', *Journal of the American Chemical Society*, 138, pp. 313–318.

Annalakshmi, M. *et al.* (2019) 'Enzyme-free electrocatalytic sensing of hydrogen peroxide using a glassy carbon electrode modified with cobalt nanoparticle-decorated tungsten carbide', *Microchimica Acta*, 186(4), pp. 1–9. doi: 10.1007/s00604-019-3377-x.

Ansari, S. A. *et al.* (2013) 'Biogenic synthesis, photocatalytic, and photoelectrochemical performance of Ag-ZnO nanocomposite', *Journal of Physical Chemistry C*, 117(51), pp. 27023–27030. doi: 10.1021/jp410063p.

Aristov, N. and Habekost, A. (2015) 'Cyclic Voltammetry - A Versatile Electrochemical Method Investigating Electron Transfer Processes', *World Journal of Chemical Education, Vol. 3, 2015, Pages 115-119*, 3(5), pp. 115–119. doi: 10.12691/wjce-3-5-2.

Ashrafi, M., Salimi, A. and Arabzadeh, A. (2016) 'Photoelectrocatalytic enzymeless detection of glucose at reduced graphene oxide/CdS nanocomposite decorated with finny ball CoOx nanostructures', *Journal of Electroanalytical Chemistry*, 783, pp. 233–241. doi: 10.1016/j.jelechem.2016.11.015.

Association, A. D. (2019) '4. Comprehensive medical evaluation and assessment of comorbidities: Standards of medical care in diabetesd2019', *Diabetes Care*, 42(January), pp. S34–S45. doi: 10.2337/dc19-S004.

Bard, A. J. and Faulkner, L. R. (2000) *Electrochemical methods and applications*. 2nd Editio. Wiley-Interscience.

Barragan, J. T. C. *et al.* (2018) 'Insight into the Electro-Oxidation Mechanism of Glucose and Other Carbohydrates by CuO-Based Electrodes', *Analytical Chemistry*, 90(5), pp. 3357–3365. doi: 10.1021/acs.analchem.7b04963.

Barrett (2016) *Public Health Ethics: Cases Spanning the Globe*. Edited by G. Ortmann, L.H., Dawson, A., Saenz, C., Reis, A., Bolan. Springer International Publishing.

Barsan, N. *et al.* (2010) 'Modeling of sensing and transduction for p-type semiconducting metal oxide based gas sensors', *Journal of Electroceramics*, 25(1), pp. 11–19. doi: 10.1007/s10832-009-9583-x.

Bhatt, V. *et al.* (2019) 'Persistent photoconductivity in Al-doped ZnO photoconductors under air, nitrogen and oxygen ambiance: Role of oxygen vacancies induced DX centers', *Ceramics International*, 45(7), pp. 8561–8570. doi: 10.1016/j.ceramint.2019.01.174.

Bijoor, S. (2006) *Scanning Electron Microscopy*. Available at: http://large.stanford.edu/courses/2007/ap273/bijoor1/.

Billy, J. T. and Co, A. C. (2018) 'Reducing the onset potential of CO2 electroreduction on CuRu bimetallic particles', *Applied Catalysis B: Environmental*, 237, pp. 911–918. doi:

10.1016/j.apcatb.2018.06.072.

Cambiaso, A. *et al.* (1995) 'Modelling and simulation of a diffusion limited glucose sensor', *International Conference on Solid-State Sensors and Actuators, and Eurosensors IX, Proceedings*, 2, pp. 40–43. doi: 10.1109/sensor.1995.721739.

Cao, L. *et al.* (2019) 'A photoelectrochemical glucose sensor based on gold nanoparticles as a mimic enzyme of glucose oxidase', *RSC Advances*, 9(27), pp. 15307–15313. doi: 10.1039/c9ra02088h.

Chandrappa, K. G. and Venkatesha, T. V. (2013) 'Electrochemical bulk synthesis and characterisation of hexagonal-shaped CuO nanoparticles', *Journal of Experimental Nanoscience*, 8(4), pp. 516–532. doi: 10.1080/17458080.2011.597440.

Chem LibreTexts (2020) *Reversibility – Chemical vs. Electrochemical*. Available at: https://chem.libretexts.org/Bookshelves/Analytical_Chemistry/Supplemental_Modules_(Analytical_Chemistry)/Analytical_Sciences_Digital_Library/JASDL/Courseware/Analytical_Electrochemistry%3A_The_Basic_Concepts/03_Fundamentals_of_Electrochemistry/B%3A_The_El.

Chen, J. *et al.* (2017) ' A Pt/TiO 2 Nanotube Array Electrode for Glucose Detection and Its Photoelectrocatalysis Self-Cleaning Ability ', *Journal of The Electrochemical Society*, 164(2), pp. B66–B73. doi: 10.1149/2.0921702jes.

Chen, Y. *et al.* (2018) 'The lower rather than higher density charge carrier determines the NH 3 -sensing nature and sensitivity of ambipolar organic semiconductors', *Materials Chemistry Frontiers*, 2(5), pp. 1009–1016. doi: 10.1039/c7qm00607a.

Cho, S. K. *et al.* (2007) 'Acceleration effect of CuCN in Ag electroplating for ultralarge-scale interconnects', *Electrochemical and Solid-State Letters*, 10(10), pp. 116–119. doi: 10.1149/1.2769103.

Chu, D. and Fedkiw, P. S. (1993) 'The electrochemistry of a cuprous cyanide strike-plating bath', *Journal of Electroanalytical Chemistry*, 345(1–2), pp. 107–120. doi: 10.1016/0022-0728(93)80472-T.

Costa, D. *et al.* (2020) *Nanoparticles for New Pharmaceuticals: Metabolites from Actinobacteria*. doi: 10.1007/978-3-030-26668-4_6.

Debbichi, L. *et al.* (2012) 'Vibrational properties of CuO and Cu 4O 3 from first-principles calculations, and raman and infrared spectroscopy', *Journal of Physical Chemistry C*, 116(18), pp. 10232–10237. doi: 10.1021/jp303096m.

Depauw (2020) *Introduction to Voltammetry*. Available at: http://dpuadweb.depauw.edu/harvey_web/eTextProject/_site/threeImportantConcepts.html.

Dhand, C. *et al.* (2015) 'Methods and strategies for the synthesis of diverse nanoparticles and their applications: A comprehensive overview', *RSC Advances*, 5(127), pp. 105003–105037. doi: 10.1039/c5ra19388e.

Double, E. *et al.* (1990) '<Electrical Double Layer -- Recent Experimental and Theoretical.pdf>', pp. 813–826.

Dunwell, M., Yan, Y. and Xu, B. (2018) 'Understanding the influence of the electrochemical double-layer on heterogeneous electrochemical reactions', *Current Opinion in Chemical Engineering*, 20, pp. 151–158. doi: 10.1016/j.coche.2018.05.003.

Ebnesajjad, S. (2014) *Surface and Material Characterization Techniques*, *Surface Treatment of Materials for Adhesive Bonding*. doi: 10.1016/b978-0-323-26435-8.00004-6.

Elgrishi, N. *et al.* (2018) 'A Practical Beginner's Guide to Cyclic Voltammetry', *Journal of Chemical Education*, 95(2), pp. 197–206. doi: 10.1021/acs.jchemed.7b00361. en-academic (2021) *Copper*. Available at: https://en-academic.com/dic.nsf/enwiki/82997 (Accessed: 15 June 2020).

Ertek, B., Akgül, C. and Dilgin, Y. (2016) 'Photoelectrochemical glucose biosensor based on a dehydrogenase enzyme and NAD+/NADH redox couple using a quantum dot modified pencil graphite electrode', *RSC Advances*, 6(24), pp. 20058–20066. doi: 10.1039/c5ra25673a.

Felix, S. *et al.* (2017) 'A novel CuO–N-doped graphene nanocomposite-based hybrid electrode for the electrochemical detection of glucose', *Applied Physics A: Materials Science and Processing*, 123(10), pp. 1–9. doi: 10.1007/s00339-017-1217-6.

Feng, C. *et al.* (2014) 'Glucose biosensors based on Ag nanoparticles modified TiO2 nanotube arrays', *Journal of Solid State Electrochemistry*, 18(1), pp. 163–171. doi: 10.1007/s10008-013-2257-2.

Fujishima and Honda (1972) 'Electrochemical Photolysis of Water at a Semiconductor Electrode', *Nature*, 238(5358), pp. 38–40. doi: 10.1038/238037a0.

Fujiwara, Y. and Enomoto, H. (2000) 'Electrodeposition of β'-Brass from Cyanide Baths with Accumulative Underpotential Deposition of Zn', *Journal of The Electrochemical Society*, 147(5), p. 1840. doi: 10.1149/1.1393444.

Gamry (2021a) *Chronoamperometry Purpose*. Available at: Chronoamperometry Purpose.

Gamry (2021b) *Two, Three and Four Electrode Experiments*. Available at: https://www.gamry.com/application-notes/instrumentation/two-three-four-electrode-experiments/.

Giziński, D. *et al.* (2020) 'Nanostructured anodic copper oxides as catalysts in electrochemical and photoelectrochemical reactions', *Catalysts*, 10(11), pp. 1–38. doi: 10.3390/catal10111338.

Graham, D. J. (2018) *Standard Operating Procedures for Cyclic Voltammetry*. 1st Editio. Available at: https://sop4cv.com/chapters/ChangingScanRates.html.

Grigore, M. E. *et al.* (2016) 'Methods of synthesis, properties and biomedical applications of CuO nanoparticles', *Pharmaceuticals*, 9(4), pp. 1–14. doi: 10.3390/ph9040075.

Guillén, C. and Herrero, J. (2018) 'Single-phase Cu2O and CuO thin films obtained by low-

temperature oxidation processes', *Journal of Alloys and Compounds*, 737, pp. 718–724. doi: 10.1016/j.jallcom.2017.12.174.

Han, C. *et al.* (2014) 'Improving the photocatalytic activity and anti-photocorrosion of semiconductor ZnO by coupling with versatile carbon', *Physical Chemistry Chemical Physics*, 16(32), pp. 16891–16903. doi: 10.1039/c4cp02189d.

Harris, A. R. *et al.* (2019) 'Using chronopotentiometry to better characterize the charge injection mechanisms of platinum electrodes used in bionic devices', *Frontiers in Neuroscience*, 13(APR), pp. 1–13. doi: 10.3389/fnins.2019.00380.

Haynes, W. M. (2016) *CRC Handbook of Chemistry and Physics, 97th Edition*. 97th Editi. CRC Press.

van den Heever, T. S. and Perold, W. J. (2013) 'The influence of resistance and carrier concentration on the output voltage of a ZnO nanogenerator', *Micro and Nano Systems Letters*, 1(1), pp. 2–7. doi: 10.1186/2213-9621-1-4.

Hirst, J. *et al.* (2019) 'Comparative Study of Photocarrier Dynamics in CVD-deposited CuWO4, CuO, and WO3 Thin Films for Photoelectrocatalysis', *Zeitschrift fur Physikalische Chemie*, 234(4), pp. 699–717. doi: 10.1515/zpch-2019-1485.

Hong, I. K., Park, J. W. and Lee, S. B. (2014) 'Balancing of plating solution in CuCN electroplating process', *Journal of Industrial and Engineering Chemistry*, 20(5), pp. 3068–3074. doi: 10.1016/j.jiec.2013.11.045.

Hwang, D. W. *et al.* (2018) 'Recent advances in electrochemical non-enzymatic glucose sensors – A review', *Analytica Chimica Acta*, 1033, pp. 1–34. doi: 10.1016/j.aca.2018.05.051.

Hwang, J. Y., Wang, Y. Y. and Wan, C. C. (1987) 'Electrolytic oxidation of cuprocyanide electroplating waste waters under different pH conditions', *Journal of Applied Electrochemistry*, 17(4), pp. 684–694. doi: 10.1007/BF01007802.

Institute, E. C. (2018) *How much copper is there and where does it come from*. Available at: https://copperalliance.eu/about-copper/copper-and-its-alloys/resources/.

Inyang, A. *et al.* (2020) 'One step copper oxide (CuO) thin film deposition for non-enzymatic electrochemical glucose detection', *Thin Solid Films*, 709(July), p. 138244. doi: 10.1016/j.tsf.2020.138244.

Jafari, F., Salimi, A. and Navaee, A. (2014) 'Electrochemical and photoelectrochemical sensing of dihydronicotinamide adenine dinucleotide and glucose based on noncovalently functionalized reduced graphene oxide-cadmium sulfide quantum dots/poly-nile blue nanocomposite', *Electroanalysis*, 26(8), pp. 1782–1793. doi: 10.1002/elan.201400164.

Joya, M. R., Barba-Ortega, J. and Raba, A. M. (2019) 'Vibrational Raman modes and particle size analysis of cupric oxide with calcination temperature', *Indian Journal of Pure and Applied Physics*, 57(4), pp. 268–271.

Juska, V. B. and Pemble, M. E. (2020) 'A critical review of electrochemical glucose sensing: Evolution of biosensor platforms based on advanced nanosystems', *Sensors (Switzerland)*, 20(21), pp. 1–28. doi: 10.3390/s20216013.

Karamanou, M. (2016) 'Milestones in the history of diabetes mellitus: The main contributors', *World Journal of Diabetes*, 7(1), p. 1. doi: 10.4239/wjd.v7.i1.1.

Khan, Ibrahim, Saeed, K. and Khan, Idrees (2019) 'Nanoparticles: Properties, applications and toxicities', *Arabian Journal of Chemistry*, 12(7), pp. 908–931. doi: 10.1016/j.arabjc.2017.05.011.

Kim, M. J. *et al.* (2012) 'Facile Formation of Cu-Ag Film by Electrodeposition for the Oxidation-Resistive Metal Interconnect', *Journal of The Electrochemical Society*, 159(4), pp. D253–D259. doi: 10.1149/2.104204jes.

Kim, M. J. *et al.* (2013) 'Fabrication of Cu-Ag Interconnection Using Electrodeposition: The Mechanism of Superfilling and the Properties of Cu-Ag Film', *Journal of The Electrochemical Society*, 160(12), pp. D3126–D3133. doi: 10.1149/2.020312jes.

Kubelka, P. (1954) 'New Contributions to the Optics of Intensely Light-Scattering Materials Part II: Nonhomogeneous Layers*', *Journal of the Optical Society of America*, 44(4), p. 330. doi: 10.1364/josa.44.000330.

Kyle, J. H. and Hefter, G. (2015) 'A critical review of the thermodynamics of hydrogen cyanide and copper(I)-cyanide complexes in aqueous solution', *Hydrometallurgy*, 154, pp. 78–87. doi: 10.1016/j.hydromet.2015.03.012.

Lee, S. Y. *et al.* (2016) 'Charting the Outer Helmholtz Plane and the Role of Nitrogen Doping in the Oxygen Reduction Reaction Conducted in Alkaline Media Using Nonprecious Metal Catalysts', *Journal of Physical Chemistry C*, 120(43), pp. 24511–24520. doi: 10.1021/acs.jpcc.6b04771.

Li, D. *et al.* (2010) 'Conductometric chemical sensor based on individual CuO nanowires', *Nanotechnology*, 21(48). doi: 10.1088/0957-4484/21/48/485502.

Li, R. *et al.* (2019) 'Influence of Charge Carriers Concentration and Mobility on the Gas Sensing Behavior of Tin Dioxide Thin Films', *Coatings*, 9(9), p. 591. doi: 10.3390/coatings9090591.

Li, Z. *et al.* (2011) 'Comparison of the operation of polymer/fullerene, polymer/polymer, and polymer/nanocrystal solar cells: A transient photocurrent and photovoltage study', *Advanced Functional Materials*, 21(8), pp. 1419–1431. doi: 10.1002/adfm.201002154.

Li, Z. *et al.* (2014) 'Influence of nanoparticle shape on charge transport and recombination in polymer/nanocrystal solar cells', *Physical Chemistry Chemical Physics*, 16(47), pp. 25684–25693. doi: 10.1039/c4cp01111b.

Li, Z. *et al.* (2015) 'Rational design of binder-free noble metal/metal oxide arrays with nanocauliflower structure for wide linear range nonenzymatic glucose detection', *Scientific Reports*, 5(April), pp. 1–10. doi: 10.1038/srep10617.

Liao, H. and Reitberger, T. (2013) 'Generation of free OHaq radicals by black light illumination of degussa (Evonik) P25 TiO2 aqueous suspensions', *Catalysts*, 3(2), pp. 418–443. doi: 10.3390/catal3020418.

Lide, D. R. (2005) *CRC Handbook of Chemistry and Physics*. 74th Editi. CRC Press. Available at: http://webdelprofesor.ula.ve/ciencias/isolda/libros/handbook.pdf.

Liu, M., Yu, Y. X. and Zhang, W. De (2017) 'A Non-enzymatic Hydrogen Peroxide Photoelectrochemical Sensor Based on a BiVO4 Electrode', *Electroanalysis*, 29(1), pp. 305–311. doi: 10.1002/elan.201600366.

De Los Santos Valladares, L. *et al.* (2012) 'Crystallization and electrical resistivity of Cu 2O and CuO obtained by thermal oxidation of Cu thin films on SiO 2/Si substrates', *Thin Solid Films*, 520(20), pp. 6368–6374. doi: 10.1016/j.tsf.2012.06.043.

Lowenheim, F. A. (1974) *Modern Electroplating*. 3rd Editio. Wiley-Interscience.

Lowenheim, F. A. (1977) *Electroplating: Fundamentals of Surface Finishing*. 1st Editio. McGraw Hill.

Lu, J., Dreisinger, D. and Cooper, W. (2002) 'Thermodynamics of the aqueous copper-cyanide system', *Hydrometallurgy*, 66, pp. 23–36.

Luo, J. *et al.* (2012) 'A novel non-enzymatic glucose sensor based on Cu nanoparticle modified graphene sheets electrode', *Analytica Chimica Acta*, 709, pp. 47–53. doi: 10.1016/j.aca.2011.10.025.

Majumdar, S. and Mahanta, D. (2020) 'Deposition of an ultra-thin polyaniline coating on a TiO2surface by vapor phase polymerization for electrochemical glucose sensing and photocatalytic degradation', *RSC Advances*, 10(30), pp. 17387–17395. doi: 10.1039/d0ra01571g.

Makuła, P., Pacia, M. and Macyk, W. (2018) 'How To Correctly Determine the Band Gap Energy of Modified Semiconductor Photocatalysts Based on UV-Vis Spectra', *Journal of Physical Chemistry Letters*, 9(23), pp. 6814–6817. doi: 10.1021/acs.jpclett.8b02892.

Masudy-Panah, S. *et al.* (2016) 'Rapid thermal annealing assisted stability and efficiency enhancement in a sputter deposited CuO photocathode†', *RSC Advances*, 6(35), pp. 29383–29390. doi: 10.1039/c6ra03383k.

Materials Project (2021) *pourbaixdiagram*. Available at: https://materialsproject.org/#apps/pourbaixdiagram/%7B%22chemsys%22%3A[%22Cu%22]%7D (Accessed: 23 November 2020).

Mcauley, C. and Compton, R. G. (2012) 'Voltammetry of multi-electron electrode processes of organic species', *Journal of Electroanalytical Chemistry*, 669, pp. 73–81. doi: 10.1016/j.jelechem.2012.01.016.

Meng, F. and Liu, L. (2019) 'Electrochemical Evaluation Technologies of Organic Coatings', *Coatings and Thin-Film Technologies*. doi: 10.5772/intechopen.79736.

Mensah, J. B. *et al.* (2018) 'Mechanistic Studies of the Cu(OH)+-Catalyzed Isomerization of

Glucose into Fructose in Water', *ChemSusChem*, 11(15), pp. 2579–2586. doi: 10.1002/cssc.201800483.

Morasch, J. *et al.* (2016) 'Influence of grain boundaries and interfaces on the electronic structure of polycrystalline CuO thin films', *Physica Status Solidi (A) Applications and Materials Science*, 213(6), pp. 1615–1624. doi: 10.1002/pssa.201533018.

Myland, J. C. and Oldham, K. B. (2004) 'Cottrell's equation revisited: An intuitive, but unreliable, novel approach to the tracking of electrochemical diffusion', *Electrochemistry Communications*, 6(4), pp. 344–350. doi: 10.1016/j.elecom.2004.01.013.

Nagajyothi (2015) 'Co 3 O 4 nanoparticles as a high-performance', *Physical Chemistry Chemical Physics*, 18, pp. 926–931. Available at: http://dx.doi.org/10.1039/C5CP06815K.

National Institute of Standards and Technology (2019) *The Hall Effect*. Available at: https://www.nist.gov/pml/nanoscale-device-characterization-division/popular-links/hall-effect/hall-effect.

Nicholson, R. S. and Shain, I. (1964) 'Single Scan and Cyclic Methods Applied to Reversible, Irreversible, and Kinetic Systems', *Analytical Chemistry*, 36(4), pp. 706–723.

Nosaka, Y. and Nosaka, A. (2016) 'Understanding Hydroxyl Radical (•OH) Generation Processes in Photocatalysis', *ACS Energy Letters*, 1(2), pp. 356–359. doi: 10.1021/acsenergylett.6b00174.

Oliver, N. S. *et al.* (2009) 'Glucose sensors: A review of current and emerging technology', *Diabetic Medicine*, 26(3), pp. 197–210. doi: 10.1111/j.1464-5491.2008.02642.x.

Opoku, F. *et al.* (2017) 'Understanding the mechanism of enhanced charge separation and visible light photocatalytic activity of modified wurtzite ZnO with nanoclusters of ZnS and graphene oxide: From a hybrid density functional study', *New Journal of Chemistry*, 41(16), pp. 8140–8155. doi: 10.1039/c7nj01942d.

van Oversteeg, C. H. M. *et al.* (2020) 'Copper sulfide derived nanoparticles supported on carbon for the electrochemical reduction of carbon dioxide', *Catalysis Today*, (August). doi: 10.1016/j.cattod.2020.09.020.

Pap, J. S. and Szyrwiel, Ł. (2017) 'On the Cu(III)/Cu(II) Redox Chemistry of Cu-Peptide Complexes to Assist Catalyst Design', *Comments on Inorganic Chemistry*, 37(2), pp. 59–77. doi: 10.1080/02603594.2016.1192541.

Parenr, L. S. *et al.* (1980) 'O f t h e american chemical society', 102.

Park, C., Lee, S. M. and Chang, W. S. (2016) 'Carrier transport behaviors depending on the two orthogonally directional energy bands in the ZnO nanofilm affected by oxygen plasma', *Physical Chemistry Chemical Physics*, 18(37), pp. 26184–26191. doi: 10.1039/c6cp04391g.

Park, S., Boo, H. and Chung, T. D. (2006) 'Electrochemical non-enzymatic glucose sensors',

Analytica Chimica Acta, 556(1), pp. 46–57. doi: 10.1016/j.aca.2005.05.080.

Parmigiani, F. *et al.* (1992) 'The fine structure of the Cu2p3 2 X-ray photoelectron spectra of copper oxide based compounds', *Journal of Electron Spectroscopy and Related Phenomena*, 58(4), pp. 315–323. doi: 10.1016/0368-2048(92)85017-2.

Paršin, A. N. (1976) 'On the arithmetic of two-dimensional schemes. I. distributions and residues', *Mathematics of the USSR - Izvestija*, 10(4), pp. 695–729. doi: 10.1070/IM1976v010n04ABEH001810.

Passal, F. (2006) 'Copper Plating during the Last 50 Years', 46. Available at: https://www.nmfrc.org/pdf/psf2006/100638.pdf.

Pirsaheb, M. *et al.* (2020) 'Optimization of photocatalytic degradation of methyl orange using immobilized scoria-Ni/TiO2 nanoparticles', *Journal of Nanostructure in Chemistry*, 10(2), pp. 143–159. doi: 10.1007/s40097-020-00337-x.

Rajeshwar, K. *et al.* (2008) 'Heterogeneous photocatalytic treatment of organic dyes in air and aqueous media', *Journal of Photochemistry and Photobiology C: Photochemistry Reviews*, 9(4), pp. 171–192. doi: 10.1016/j.jphotochemrev.2008.09.001.

Randviir, E. P. (2018) *A cross examination of electron transfer rate constants for carbon screen-printed electrodes using Electrochemical Impedance Spectroscopy and cyclic voltammetry*, *Electrochimica Acta*. Elsevier Ltd. doi: 10.1016/j.electacta.2018.08.021.

Raziq, A. *et al.* (2017) 'Electrochemical Investigation of Glucose Oxidation on a Glassy Carbon Electrode Using Voltammetric, Amperometric, and Digital Simulation Methods', *ChemistrySelect*, 2(30), pp. 9711–9717. doi: 10.1002/slct.201701193.

Rios, J. F., Calderón, J. A. and Nogueira, R. P. (2011) 'Electrochemical behavior of copper in drinking water: Evaluation of dissolution process at low anodic overpotential', *Journal of the Brazilian Chemical Society*, 22(7), pp. 1362–1370. doi: 10.1590/S0103-50532011000700023.

Robson, H., Reinhardt, M. and Bracher, C. (2021) *Cyclic Voltammetry: Basic Principles & Set Up*. Available at: https://www.ossila.com/pages/cyclic-voltammetry (Accessed: 5 June 2020).

Ruffino, F. and Grimaldi, M. G. (2019) 'Nanostructuration of thin metal films by pulsed laser irradiations: A review', *Nanomaterials*, 9(8). doi: 10.3390/nano9081133.

Sandford, C. *et al.* (2019) 'A synthetic chemist's guide to electroanalytical tools for studying reaction mechanisms', *Chemical Science*, 10(26), pp. 6404–6422. doi: 10.1039/c9sc01545k.

Sattarahmady, N. and Heli, H. (2012) 'A non-enzymatic amperometric sensor for glucose based on cobalt oxide nanoparticles', *Journal of Experimental Nanoscience*, 7(5), pp. 529–546. doi: 10.1080/17458080.2010.539275.

Sehit, E. and Altintas, Z. (2020) 'Significance of nanomaterials in electrochemical glucose sensors: An updated review (2016-2020)', *Biosensors and Bioelectronics*,

159(January), p. 112165. doi: 10.1016/j.bios.2020.112165.

Settle, F. A. (1997) *Handbook of Instrumental Techniques for Analytical*. Prentice Hall.

Shibata, H. *et al.* (1998) 'Hydroxyl radical generation depending on O2 or H2O by a photocatalyzed reaction in an aqueous suspension of titanium dioxide', *Bioscience, Biotechnology and Biochemistry*, pp. 2306–2311. doi: 10.1271/bbb.62.2306.

Su, Y. (2018) *Copper Oxide Nano Photocatalyst for Wastewater Purification using Visible Light*. University of Cambridge. doi: 10.17863/CAM.25069.

Syrek, K. *et al.* (2019) 'A photoelectrochemical sensor based on anodic tio2 for glucose determination', *Sensors (Switzerland)*, 19(22). doi: 10.3390/s19224981.

Szpyrkowicz, L. *et al.* (1998) 'Electrochemical treatment of copper cyanide wastewaters using stainless steel electrodes', *Water Science and Technology*, 38(6), pp. 261–268. doi: 10.1016/S0273-1223(98)00598-8.

Thenmozhi, S. *et al.* (2017) 'Electrospun nanofibers: New generation materials for advanced applications', *Materials Science and Engineering B: Solid-State Materials for Advanced Technology*, 217, pp. 36–48. doi: 10.1016/j.mseb.2017.01.001.

Tian, K., Prestgard, M. and Tiwari, A. (2014) 'A review of recent advances in nonenzymatic glucose sensors', *Materials Science & Engineering C*, 41, pp. 100–118. doi: 10.1016/j.msec.2014.04.013.

Tian, L. *et al.* (2018) 'Co3O4 Based Non-Enzymatic Glucose Sensor', *Journal of Nanotechnology*, pp. 0–15.

Toghill, K. E. and Compton, R. G. (2010) 'Electrochemical non-enzymatic glucose sensors: A perspective and an evaluation', *International Journal of Electrochemical Science*, 5(9), pp. 1246–1301.

Torto, N., Ruzgas, T. and Gorton, L. (1999) 'Electrochemical oxidation of mono- and disaccharides at fresh as well as oxidized copper electrodes in alkaline media', *Journal of Electroanalytical Chemistry*, 464(2), pp. 252–258. doi: 10.1016/S0022-0728(99)00041-8.

Tran, T. H. and Nguyen, V. T. (2014) 'Copper Oxide Nanomaterials Prepared by Solution Methods, Some Properties, and Potential Applications: A Brief Review', *International Scholarly Research Notices*, 2014, pp. 1–14. doi: 10.1155/2014/856592.

Travaini, R. *et al.* (2015) *Ozonolysis*, *Pretreatment of Biomass: Processes and Technologies*. doi: 10.1016/B978-0-12-800080-9.00007-4.

University of Cambridge (2020) *Direct and Indirect Band Gap Semiconductors*. Available at: https://www.doitpoms.ac.uk/tlplib/semiconductors/direct.php.

Wang, L., Han, K. and Tao, M. (2007) 'Effect of Substrate Etching on Electrical Properties of Electrochemically Deposited CuO', *Journal of The Electrochemical Society*, 154(2), p. D91. doi: 10.1149/1.2404913.

Wang, S. *et al.* (2019) 'A non-enzymatic photoelectrochemical glucose sensor based on BiVO4

electrode under visible light', *Sensors and Actuators, B: Chemical*, 291(April), pp. 34–41. doi: 10.1016/j.snb.2019.04.057.

Wang, X. *et al.* (2010) 'Synthesis of CuO nanostructures and their application for nonenzymatic glucose sensing', *Sensors and Actuators, B: Chemical*, 144(1), pp. 220–225. doi: 10.1016/j.snb.2009.09.067.

Weatherspoon, D. (2019) *What's a Normal Blood pH and What Makes It Change?* Available at: https://www.healthline.com/health/ph-of-blood.

Wen, L. *et al.* (2012) 'Synthesis, characterization, and photocatalysis of Fe-doped TiO 2: A combined experimental and theoretical study', *International Journal of Photoenergy*, 2012. doi: 10.1155/2012/368750.

Wu, J. *et al.* (2014) 'Charge transport in single CuO nanowires', *Applied Physics Letters*, 105(18). doi: 10.1063/1.4900966.

Xia, L. P. *et al.* (2015) 'Cu(III)-independent oxidation and sensing of glucose on multi-layer stacked copper nanoparticles', *Microchimica Acta*, 182(7–8), pp. 1289–1295. doi: 10.1007/s00604-015-1447-2.

Xiang, J. Y. *et al.* (2011) 'Electrochemical impedance analysis of a hierarchical cuo electrode composed of self-assembled nanoplates', *Journal of Physical Chemistry C*, 115(5), pp. 2505–2513. doi: 10.1021/jp108261t.

Xie, Y. and Huber, C. 0. (2001) 'M o m o Librodot', (164), pp. 5–10. doi: 10.1021/ac00017a012.

Yabuki, A. and Arriffin, N. (2010) 'Electrical conductivity AR of copper nanoparticle thin films annealed at low temperature', *Thin Solid Films*, 518(23), pp. 7033–7037. doi: 10.1016/j.tsf.2010.07.023.

Yang, L. W. *et al.* (2020) 'Improving linear range limitation of non-enzymatic glucose sensor by OH− concentration', *Crystals*, 10(3). doi: 10.3390/cryst10030186.

Yang, X. *et al.* (2018) 'Influence of sulfides on the passivation behavior of titanium alloy TA2 in simulated seawater environments', *Applied Surface Science*, 458(July), pp. 198–209. doi: 10.1016/j.apsusc.2018.07.068.

Zeghbroeck, B. Van (2011a) *Chapter 2: Semiconductor Fundamentals*. Available at: https://ecee.colorado.edu/~bart/book/book/chapter2/ch2_7.htm#fig2_7_1.

Zeghbroeck, B. Van (2011b) 'Principles of Semiconductor Devices'.

Zeghbroeck, B. Van (2011c) 'Principles of Semiconductor Devices'. Available at: https://ecee.colorado.edu/~bart/book/book/chapter2/ch2_8.htm.

Zhang, J. T. *et al.* (2004) 'Studies of impedance models and water transport behaviors of polypropylene coated metals in NaCl solution', *Progress in Organic Coatings*, 49(4), pp. 293–301. doi: 10.1016/S0300-9440(03)00115-2.

Zhu, C. and Panzer, M. J. (2016) 'Etching of electrodeposited Cu2O films using ammonia solution for photovoltaic applications', *Physical Chemistry Chemical Physics*, 18(9), pp. 6722–6728. doi: 10.1039/c5cp06385j.

Zhu, H. *et al.* (2016) 'Advances in non-enzymatic glucose sensors based on metal oxides', *Journal of Materials Chemistry B*, 4(46), pp. 7333–7349. doi: 10.1039/C6TB02037B.

Appendix

S-1.1 Physical Characterization:

X-ray photoelectron spectroscopy experiments were conducted by bombarding selected samples with X-rays of known energy while recording the kinetic energy of the released photoelectrons. From this the binding energy is calculated and used to identify the elements from which the electrons were extracted. Figure S1 presents the core Cu 2p, O 1s, C 1s and Na peaks. The Cu 2p core level's XPS spectra for the "calcined" sample featured two peaks corresponding to Cu $2p_{3/2}$ and Cu $2p_{1/2}$ which occurred at 933.2 eV and 953.4 eV respectively. The former binding energy is assigned to Cu^{2+} ions which is characteristic of the CuO phase while the latter further confirms the presence of CuO by matching with the standard XPS spectra for CuO (Li *et al.*, 2015). At least three satellite peaks are recorded at higher binding energy relative to their main peaks at 935.0 eV, 943.4 eV and 953.4 eV which are assigned to the Cu $3d^9$ configuration. The position of the Cu $2p_{3/2}$ peak with respect to its satellite indicates the existence of two CuO configurations which are the Cu $3d^{10}$ and the Cu $3d^9$ (ground state) (Parmigiani *et al.*, 1992). This further confirms the existence of CuO. The binding energies associated with the O 1s XPS spectra revealed a strong peak at 529.3 eV which is associated with a metal-oxygen bond in the lattice. A peak at 529.2 eV confirms the M-O bond is in fact a (Cu-O) bond however some impurities were detected in the form of (C-O) bond at 531.1 eV and a (C=O) bond at 532.7 eV. The detection of these impurities is common in samples which have been stored in air as opposed to an evacuated vial. XPS did not detect any form of (-OH) species on the samples surface though the carbon-based impurities were further investigated in the C 1s core level scan. A strong sp^2 (C-C) peak was detected at 284.2 eV along with a secondary confirmation of the contaminant (C-O) and (C=O) species at 285.8 eV and 287.6 eV respectively. Interestingly, residual Na was detected even post calcination with a peak 1071.7 eV. The spectrograph spanning over the entire testing range is seen in Figure S2.

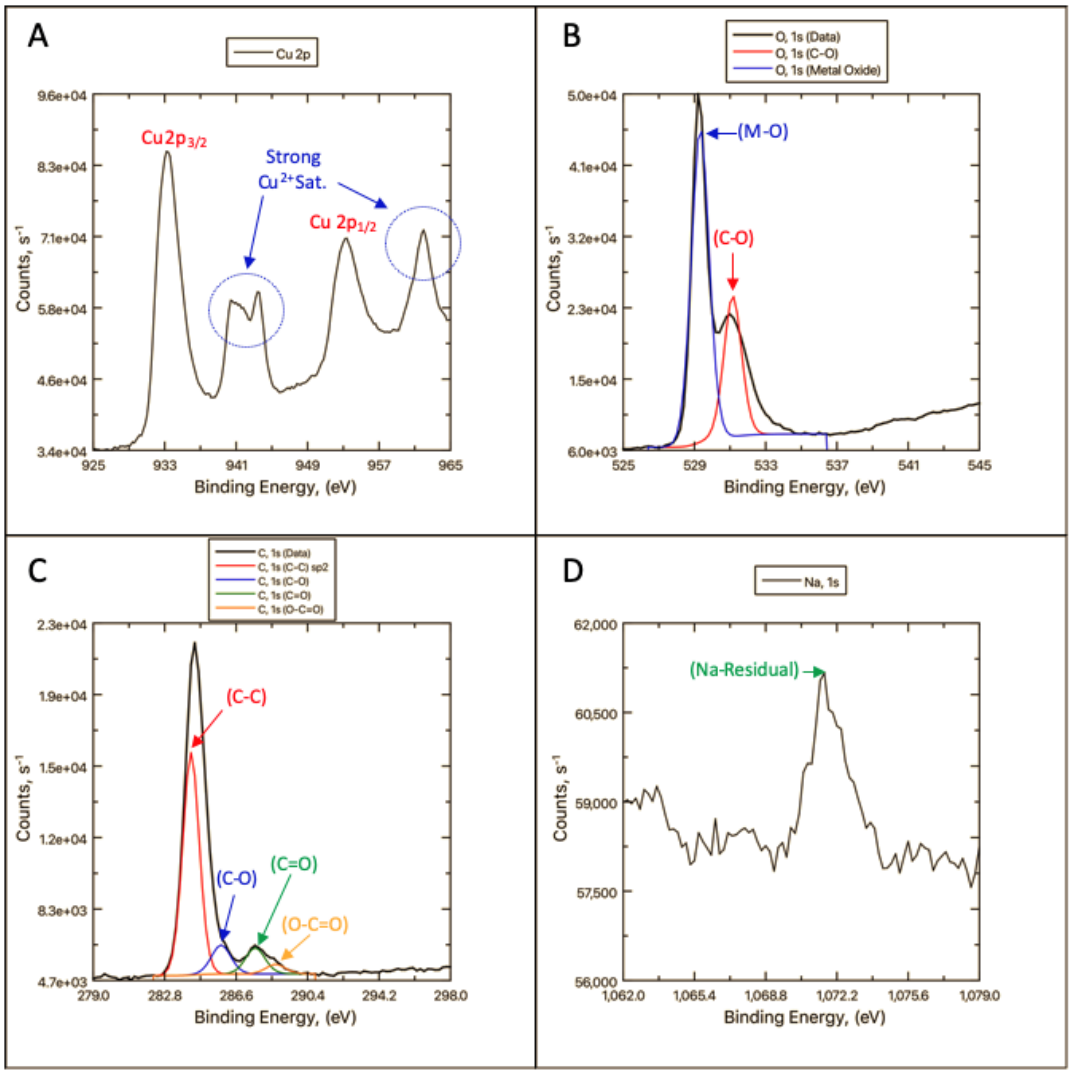

Figure S1: XPS spectrographs for the “calcined” sample focused on A) Cu 2p-peaks, B)O 1s-peaks, C)C 1s-peaks and D)Na residuals.

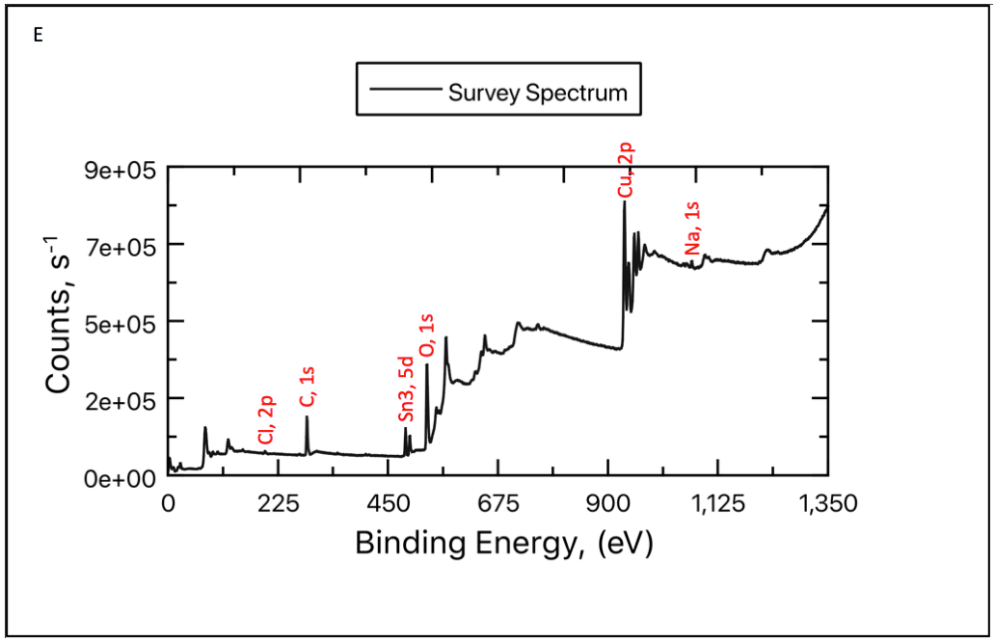

Figure S2: Spectrograph showing the full XPS range for the “calcined” sample.

S-1.2 Electrochemical characterization of “As Deposited” and “Calcined” samples:

The electrochemical characterization of the “As Deposited and Calcined” films were evaluated using cyclic voltammetry (CV) in an alkaline medium both in the presence and absence of glucose with and without light. A total of 10 stabilization cycles were performed before the data was recorded to ensure stability. The CV’s conducted in the dark were performed in an optical glass box housed in cardboard to block illumination of the sample from ambient light. The same cardboard housing was used for samples undergoing illumination via and LED (6W, 540lumen) though a cut out in the box. The kinetic interactions occurring at the electrode’s interface offer a clearer view to draw meaningful conclusions regarding the glucose oxidation process. The kinetic interactions were investigated using CV measurements over a range of scan rates (25, 30, 40, 50, 70, 100, 150, 175, 200 and 300mV/s) in a solution containing 1mM glucose and 0.1 M NaOH. Figures S3 and S4 reveals how the oxidation potential and ultimately peak current varies with scan rate for the “As Deposited” samples. Figures S5 and S6 show the same though for the “Calcined” samples.

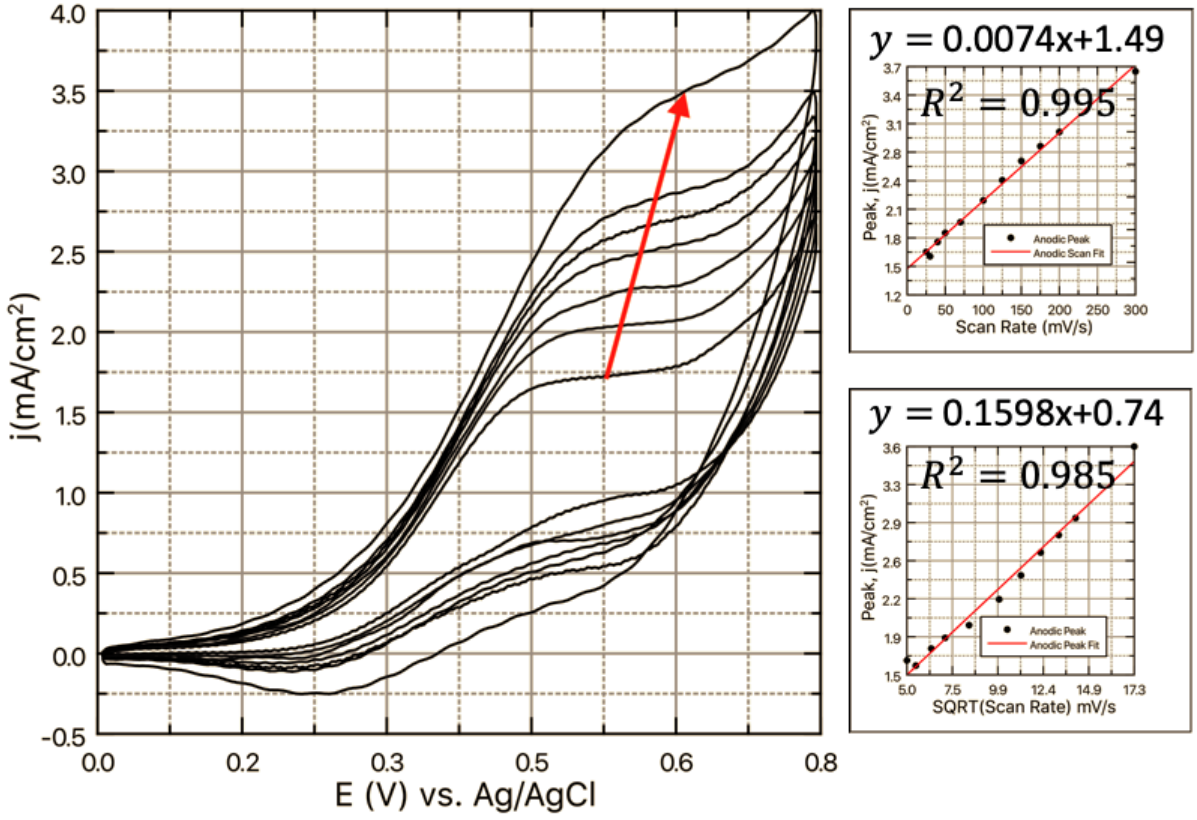

Figure S3: CV cycles in 1mM Glucose in the dark over a range of scan rates with peak anodic currents against scan rate and square root of scan rate and their linearities for the “As Deposited” sample.

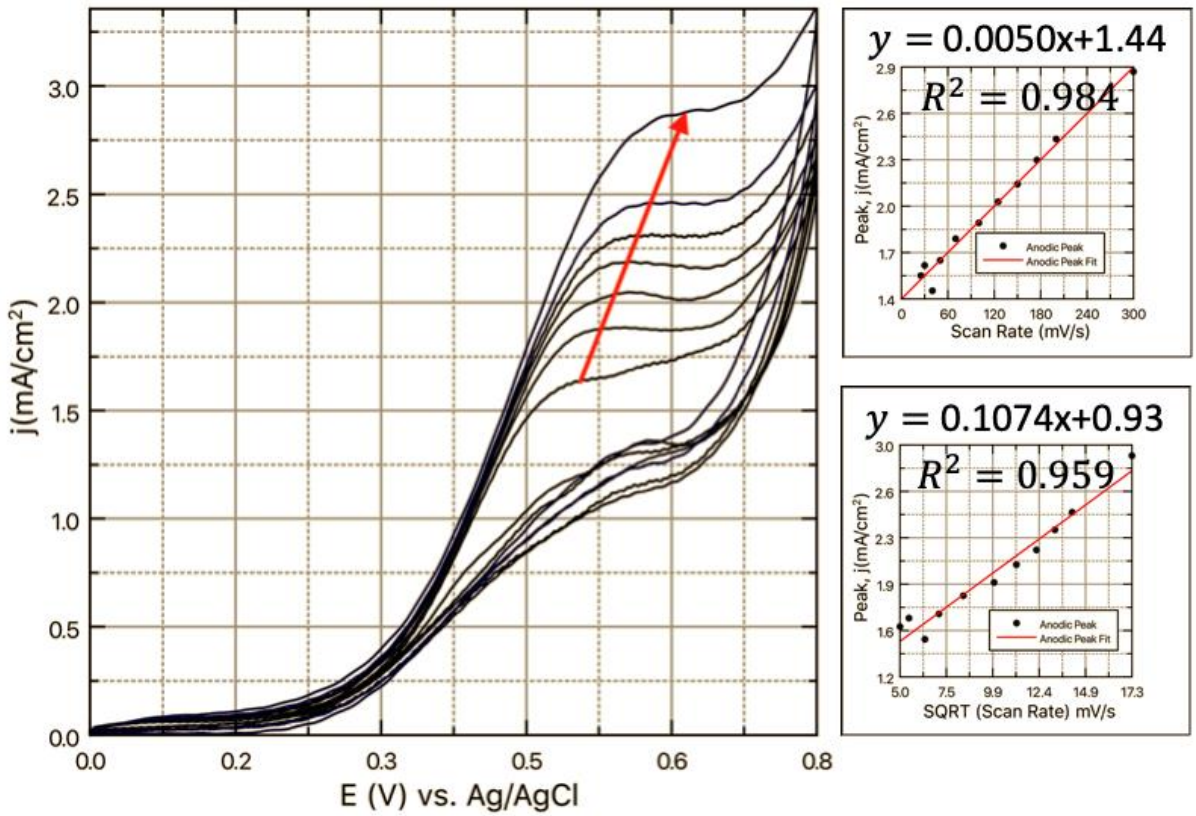

Figure S4: CV cycles in 1mM Glucose in the light over a range of scan rates with peak anodic currents against scan rate and square root of scan rate and their linearities for the “As Deposited” sample.

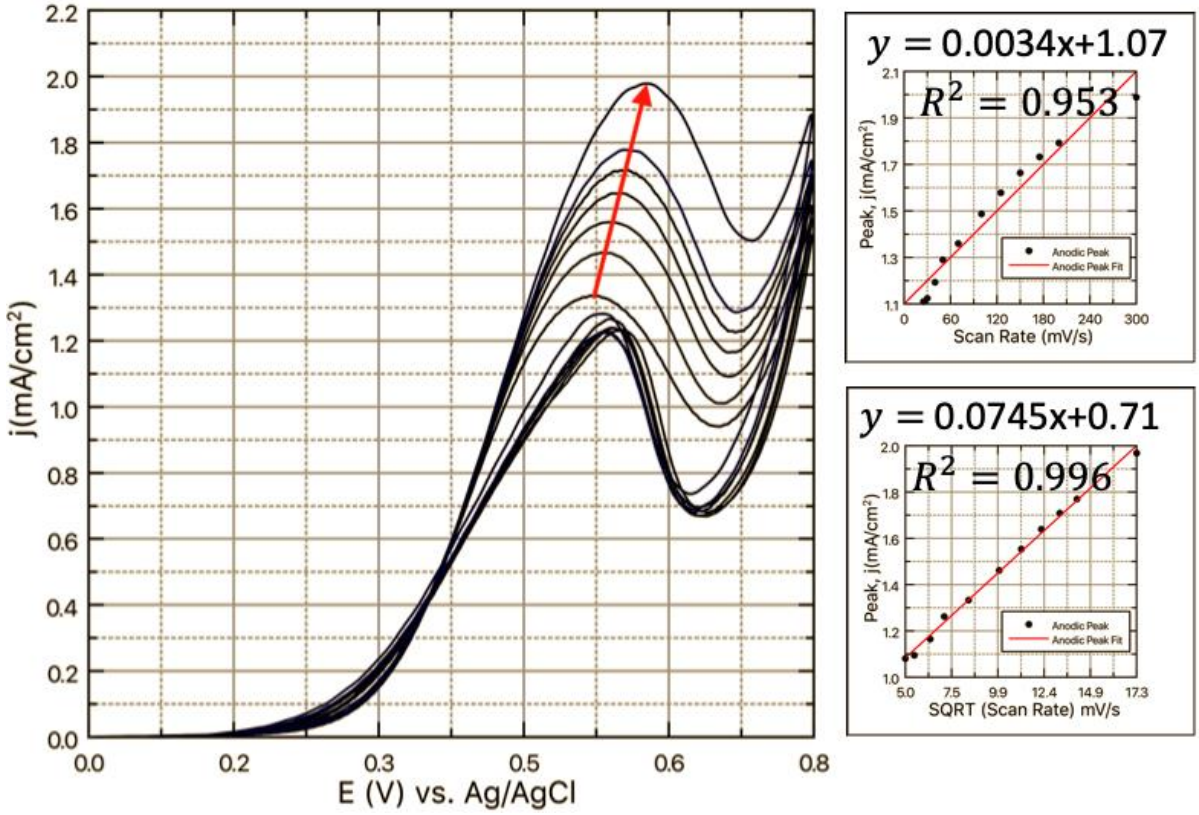

Figure S5: CV cycles in 1mM Glucose in the dark over a range of scan rates with peak anodic currents against scan rate and square root of scan rate and their linearities for the “Calcined” sample.

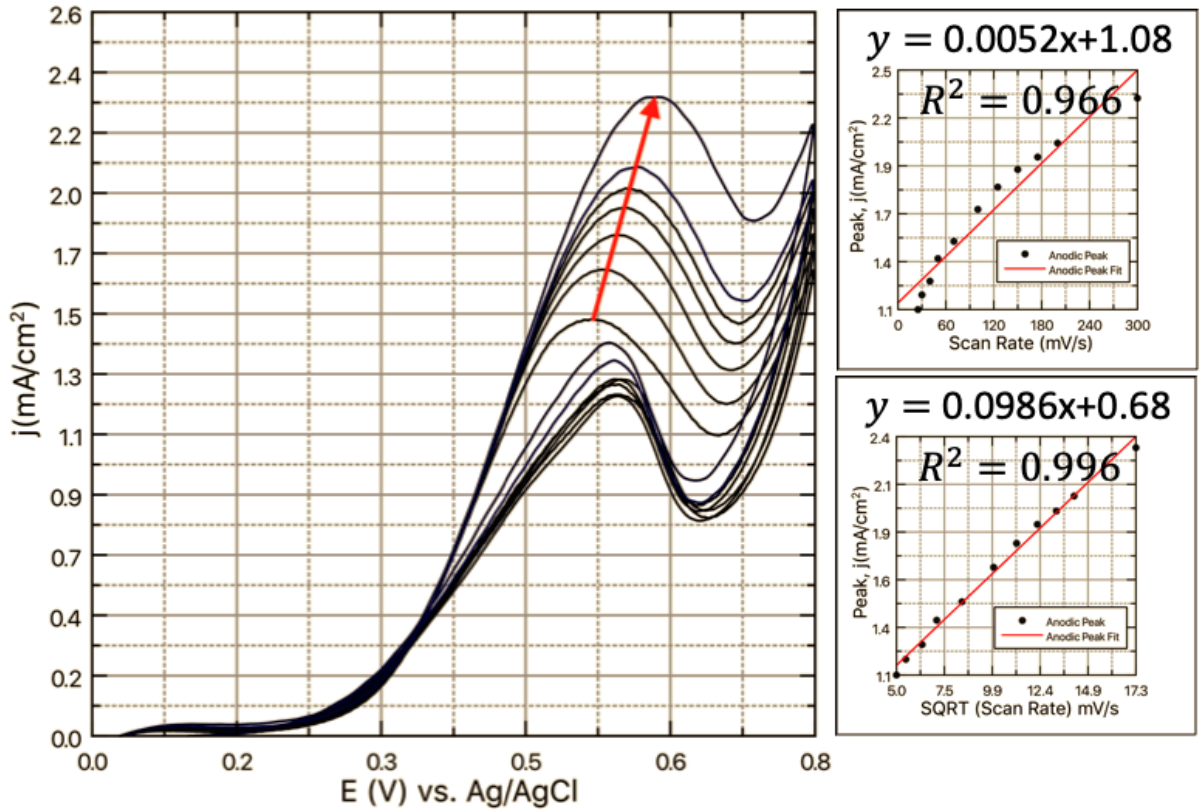

Figure S6: CV cycles in 1mM Glucose in the light over a range of scan rates with peak anodic currents against scan rate and square root of scan rate and their linearities for the “Calcined” sample.

A shift in potential to more positive oxidative levels is observed in both “As Deposited” and “Calcined” samples with increasing scan rate suggesting that the glucose oxidation process is irreversible. Again, no reduction peaks are formed at potentials lower than the oxidation potential (0.6V vs. Ag/AgCl) solidifying the irreversible nature. A strong linear dependence exists between $i_p \; and \; v$ with a regression coefficient of R^2 = 0.995 in the dark for the “As Deposited” sample. In the light, the regression coefficient decreases slightly to R^2 = 0.984 with respect to $i_p \; and \; v$ suggesting that the glucose oxidation mechanism for this sample is in fact kinetically controlled. Post calcination however, the dependencies in both the light and dark indicate that the oxidation of glucose at this CuO electrode is a mass transfer process within the double layer controlled by diffusion of glucose to the active redox sites as was the case with the “Etched” samples. The linearity of the regression lines were found to be R^2 = 0.996 in both the dark and light scenarios for the “Calcined” samples with respect to $i_p \; and \; \sqrt{v}$. Anodic shifts were also noted to increased potentials with increasing scan rate in the light.

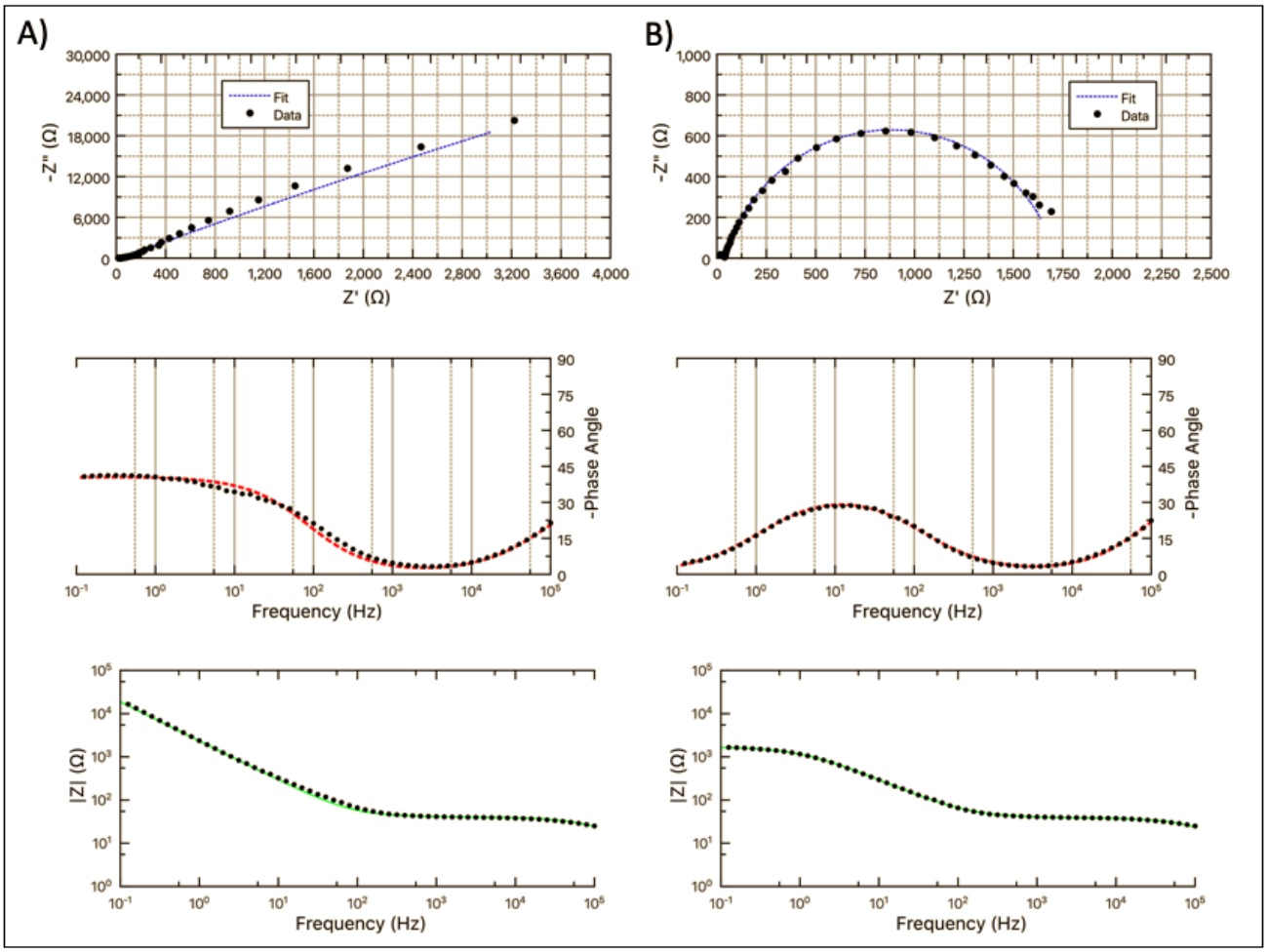

Figure S7: Nyquist and Bode plots using the modified Randel's circuit in A) Dark and B) Light for 1mM glucose